

Development of paper-based hygro-mechanical  
systems for liquid characterization

A Thesis

In the Department  
of  
Mechanical and Industrial Engineering

Presented in Partial Fulfillment of the Requirements  
For the Degree of Doctor of Philosophy at  
Concordia University  
Montreal, Quebec, Canada

March 2017

© Angel Perez-Cruz, 2017



# Abstract

Development of paper-based hygro-mechanical systems for liquid characterization

Angel Perez-Cruz, Ph.D.

Concordia University, 2017

Over the past few years, paper-based microfluidics systems have been extensively applied to perform different analytical tasks including detection and quantification of the specific analyte. Few works have reported the use of paper as a structural element to develop both sensors and actuators. These devices are extremely useful as they are inexpensive, easy to fabricate, disposable and portable. However, other features of paper that can be applied to develop new sensing principles have not been explored. Paper is a hygroscopic material that enables the generation of motion by hygromorphism.

In this work, paper-based hygro-mechanical systems (PB-HMS) for liquid characterization are developed. The configuration of the developed PB-HMS is formed by the interaction of a paper-based cantilever beam and a liquid droplet. The paper-based cantilever beam acts as a hygroscopic sensitive element, while the liquid droplet triggers the bending response of the PB-HMS. These systems do not require any external source of energy to stimulate the sensing element (i.e. electric or magnetic field) as their interaction with the liquid droplet activates the motion.

In addition, different gaps in the knowledge found in the literature were addressed to develop the PB-HMS. They are described as follows. First, an imbibition model based on Richards' equation is developed in this thesis to predict liquid imbibition in complex paper-based networks. Second, a dimensionless stress-imbibition model including three main nonlinearities (imbibition, swelling and softening) is developed in this work. Third, the influences of such nonlinearities on the characteristic hygro-mechanical bending response of paper-based beams are studied. Fourth, the design of the PB-HMS is performed in order to extract information from the systems using their dynamic response. Finally, a method to quantify the dynamic performance of the PB-HMS in order to characterize liquid is developed.

# Acknowledgment

I'm indebted to my co-supervisors Dr. Stiharu and Dr. Dominguez-Gonzalez for providing the opportunity to work under their supervision. All of their encouragement, support, suggestions, and comments have helped me to conduct this research. I would like to express my sincere gratitude to Dr. Stiharu from whom I always found an open door to discuss this research. I also would like to acknowledge Dr. Dominguez-Gonzalez for showing me the path to Concordia. Thank you Dr. Stiharu and Dr. Dominguez-Gonzalez for your extremely valuable suggestions in pursuing this research!

I would like to thank my family; I wouldn't have completed this research without them. My special thanks to my lovely wife, Monica, for all her love and support. She is the strength that helps me to make my dreams come true. Thanks to my mother for all her prayers and moral support, she has always been an inspiration to me. I also would like to acknowledge my siblings, Rosalia, Martin, and Rodrigo, for all their endless support.

*In memory of my father,*

*J. C. Mariano Perez-Rodriguez*

*Your soul will always be with us,  
and your love will always light our way.*

# Table of Contents

List of abbreviations .....	x
List of Symbols .....	xi
List of Figures.....	xv
List of Tables .....	xxiii
Chapter 1 Introduction .....	1
1.1 From Microsystems to paper-based systems .....	2
1.2 Rationale.....	6
1.3 Literature review.....	14
1.4 Objectives and thesis outline.....	27
Chapter 2 Two-dimensional imbibition into paper-based networks .....	34
2.1 Imbibition .....	35
2.2 Capillary Model .....	38
2.3 Richards' based model .....	42
2.4 Methods and materials.....	44
2.5 Imbibition into two dimensional geometries.....	46
2.6 Summary .....	57
Chapter 3 Hygro-mechanical bending response of paper....	59
3.1 Hygro-mechanical response of paper-based beams .....	60

3.2	Constitutive equations .....	64
3.3	Reduced model .....	74
3.4	Summary .....	85
Chapter 4 Nonlinear influences on the hygro-mechanical		
	bending response of paper .....	87
4.1	Nonlinearity sources .....	88
4.2	Nonlinear geometry .....	93
4.3	Material nonlinearities .....	96
4.4	Characterization of the bending response .....	109
4.5	Summary .....	113
Chapter 5 Paper-based hygro-mechanical systems as		
	sensing elements .....	114
5.1	PB-HMS design .....	115
5.2	Experimental section .....	119
5.3	Dynamic performance of the PB-HMS .....	125
5.4	Portrait signature of PB-HMS .....	133
5.5	Summary .....	139
Chapter 6 Characterization of liquids by means of PB-		
	HMS .....	141
6.1	Analogy to high order linear systems .....	142
6.2	Frequency analysis .....	146

6.3	Characterization of binary aqueous solutions .....	151
6.4	Liquid identification.....	157
6.5	Hygro-mechanical sensing capabilities .....	162
6.6	Summary .....	165
Chapter 7	Conclusions and future work .....	168
7.1	Conclusions .....	169
7.2	Particular contributions and future work .....	170
References	.....	178
Appendix A	Richard's equation .....	193
Appendix B	Large deflection solution using COMSOL .....	197

## List of abbreviations

PB-HMS	Paper-based hygro-mechanical system
MEMS	Micro-electromechanical systems
PDMS	Polydimethylsiloxane
SU8	Negative, epoxy-type, photoresist
CD	Cross direction of paper
MD	Machine direction of paper
DNA	Deoxyribonucleic acid
LW	Lucas-Washburn theory
PDE	Partial differential equation
CTC	Compressive-tensile-compressive bending state of paper along the thickness of paper from bottom to top.
TCTC	Tensile-compressive-tensile-compressive bending state of paper along the thickness of paper from bottom to top.
IR	Infrared
NIF	Near infrared
UV	Ultraviolet
C1	Paper-based cantilever beam made of tracing paper.
C2	Paper-based cantilever beam made of pad paper and filled with acrylic resin.
Fps	Frame per second

## List of Symbols

$P_{nw}$	Non-wetting pressure
$P_w$	Wetting pressure
$P_c$	Capillary pressure
$r$	Radius of a capillary tube
$\theta$	Contact angle
$\rho$	Density
$\gamma$	Viscosity
$\gamma$	Surface tension
$h_c$	Capillary rise
$x$	Cartesian coordinate
$y$	Cartesian coordinate
$z$	Cartesian coordinate
$\varphi$	Volumetric liquid content
$\varphi_s$	Saturated volumetric liquid content
$D(\varphi)$	Equivalent diffusivity of the porous media
$K(\varphi)$	Equivalent conductivity of the porous media
$D_0$	Constant of the Brooks-Corey diffusivity
$K_0$	Constant of the Brooks-Corey conductivity
$n$	Exponent of the Brooks-Corey diffusivity
$n_k$	Exponent of the Brooks-Corey conductivity
$h$	Thickness of paper
$h_{dry}$	Thickness of dry paper

$h_{wet}$	Thickness of wet paper
$l$	Length of paper-based beam
$\Delta l_h(z)$	Length extension due to hygroscopic swelling
$\Delta l_b(z)$	Apparent length extension due to bending
$\varepsilon_h(z)$	Hygroexpansive strain
$\varepsilon_b(z)$	Bending strain
$\varepsilon(z)$	Total strain
$R$	Radius of curvature
$z_n$	Neutral axis
$E$	Young modulus of elasticity
$f_1(\varphi)$	Characteristic function of the moisture diffusivity
$f_2(\varphi)$	Characteristic function of the hygroexpansive strain
$f_3(\varphi)$	Characteristic function of relaxation
$p$	Exponent of nonlinear hygroexpansive strain
$\beta$	Relaxation constant
$E_{dry}$	Young modulus of elasticity of dry paper
$m$	Ratio between wet and dry Young modulus of elasticity
$\sigma_{ij}$	Stress in the direction $ij$
$\varepsilon_{ij}$	Strain in the direction $ij$
$\nu$	Poisson's ratio
$G$	Shear modulus of elasticity
$\vartheta$	Bending angle
$\kappa_n$	Curvature at the neutral axis

$\kappa_0$	Curvature at the reference level $z=0$
$\varepsilon_0$	Strain at the reference level $z=0$
$\bar{z}$	Dimensionless coordinate
$\phi$	Dimensionless volumetric content
$\bar{t}$	Dimensionless time
$\tau$	Time constant of the bending response
$\bar{\kappa}$	Dimensionless curvature
$\eta$	Gain of the curvature
$\varepsilon_{max}$	Maximum hygroexpansive strain
$a_{ij}$	Elements $ij$ of the matrix in Eq. (3.29)
$b_i$	Elements $i$ of the vector in Eq. (3.29)
$\bar{z}_w$	Dimensionless wetting front
$p_i$	Points in the bending curvature response
$\lambda_i$	Eigenvalue $i$ of the bending response using linear solution
$\bar{a}_i, \bar{b}_i$	Coefficients $i$ of the linear bending response
$b_{wet}$	Wet portion of the cantilever beam along its length
$\Omega$	Bending angle of the PB-HMS
$\Omega'$	Bending velocity of the PB-HMS
$\Omega''$	Bending acceleration of the PB-HMS
$\xi$	Output of the equivalent high order linear system
$u_0$	Step input
$A_i, B_i$	Coefficients $i$ of the equivalent high order linear system
$H_i(s)$	Equivalent transfer function in Laplace domain “s”
$Y$	Experimental amplitude of the bending acceleration

$Y_p$	Output of the transfer function
$\bar{Y}$	Mean value of the measured signal
$U(s)$	Input signal
$Y(s)$	Output signal
$f_r$	Resonance frequency
$G_p$	Gain peak
$K$	Proportional gain
$G_m$	Gain margin
$f_c$	Crossover frequency
$d$	Distance of a given PB-HMS with respect to the reference line in the identification plot

# List of Figures

Figure 1.1	Number of publications per year of paper-based microsystems. Source: citation reports Thompson Reuters. ....	7
Figure 1.2	Hygro-bending response of a paper strip a) along the cross direction CD b) parallel to the MD c) longer dimension is oblique to the MD. Reproduced from Ref. [58] with permission from The Royal Society of Chemistry. ....	12
Figure 1.3	Areas of knowledge involved in the proposed paper-based hygro-mechanical sensor. ....	15
Figure 1.4	Paper-based microfluidics systems patterned with photoresist. Reproduced from Ref. [35] with permission from John Wiley and Sons. ....	22
Figure 1.5	Mixing using filter paper. Reproduced from Ref. [98] with permission from Elsevier. ....	24
Figure 1.6	Imbibition in a rectangular porous material using a) Lucas-Washburn and b) Richards' models. ....	26
Figure 2.1	Schematic representation of capillary imbibition into a cylindrical pore. ....	35
Figure 2.2	Representation of macro-models for imbibition into porous media: capillary based and Richard's models. ....	37
Figure 2.3	Imbibition into 2D porous networks. Different geometries analyzed in the literature. The liquid penetration into the network is represented in blue. ....	41
Figure 2.4	Schematic representation of conventional two-dimensional paper-based networks a) case I, b) case II, c) case III, and d) case IV. ....	46
Figure 2.5	Numerical results of the volumetric water content distribution for different values of n of the case I a) along AA' and b) two-dimensional domain. ....	48

Figure 2.6	Advancing wetting front due to imbibition of a) case I, b) case II, c) case III, and d) case IV. Comparison between numerical solution (using $n=6$ ) and experimental measurements. Dotted lines in b), c) and d) are the solution to the case I.....	50
Figure 2.7	Time lapse of the capillary imbibition of the case II. Gray scale images are pictures of the experimental results, and blue images represent numerical solutions.....	52
Figure 2.8	Time lapse of the capillary imbibition of case IV. Grayscale images are pictures of the experimental results, and blue images represent numerical solutions.....	54
Figure 2.9	Time lapse of the capillary imbibition of the case II. Gray scale images are experimental results, and blue images represent numerical solutions. ....	55
Figure 2.10	Advancing wet area due to imbibition of a) case I, b) case II, c) case III, and d) case IV. Comparison between numerical solution (using $n=6$ ) and experimental measurements. Dotted lines in b), c) and d) are the solution to the case I. ....	56
Figure 3.1	Microscope cross section image of a piece of chromatography paper experiencing hygroexpansive strain along its thickness. Comparison of a) dry paper and b) wet paper.....	61
Figure 3.2	Softening effect on a) dry and b) wet pieces of tracing paper.....	62
Figure 3.3	Schematic representation of the hygro-mechanical bending state. ....	64
Figure 3.4	Block diagram of the imbibition-bending coupled problem. ....	65
Figure 3.5	Comparison of 500X SEM images of a) tracing paper and b) filter paper. Bars scale represents $100 \mu\text{m}$ .....	67
Figure 3.6	$f_1(\varphi)$ as a function of the normalized volumetric water content for various values of the exponent $n$ .....	69

Figure 3.7	$f_2(\varphi)$ as a function of the normalized volumetric water content for different values of the exponent $p$ . .....	71
Figure 3.8	$f_3(\varphi)$ as a function of the normalized volumetric water content for various values of $m$ and $\beta=2$ . .....	72
Figure 3.9	Schematic representation of stresses acting on an infinitesimal element of a piece of paper. ....	73
Figure 3.10	Schematic representation of plane stresses. ....	73
Figure 3.11	Schematic representation of pure bending state of a paper beam experiencing hygroexpansive strain actuation. ....	75
Figure 3.12	Pure bending response of a paper beam undergoing hygroexpansive strain actuation a) curvature b) bending strain at $z=0$ . ....	81
Figure 3.13	Hygro-mechanical bending state cycle of a paper beam due to hygroexpansive strain actuation. ....	82
Figure 3.14	Strain state distribution at $p_2$ a) total strain, b) bending strain, and c) hygroexpansive strain. ....	83
Figure 3.15	Total strain state distribution of a) $p_1$ , b) $p_2$ , c) $p_3$ , d) $p_4$ , and e) $p_5$ from bending state plot presented in Fig. 3.13. ....	84
Figure 4.1	Hygro-mechanical bending response of a paper beam considering linear imbibition a) bending curvature and b) bending strain at reference level. Comparison among analytical, numerical and large deformation solutions. ....	91
Figure 4.2	Hygro-mechanical bending state cycle using linear imbibition theory. Comparison among analytical, numerical and large deformation solutions. ....	92
Figure 4.3	Error of the proposed model assuming linear imbibition theory due to geometrical nonlinearities. Absolute errors of both a) curvature and b) bending strain at reference level are presented. The hygroexpansive strain actuations applied are 0.05, 0.1, 1.15 and 0.2. ....	93

Figure 4.4	Illustration of the maximum bending curvature of a slender beam experiencing hygroexpansive strain actuation of a) 0.05, b) 0.10, c) 0.15 and d) 0.20. ....	95
Figure 4.5	Water content distribution along $z$ assuming nonlinear imbibition using a) $n = 0$ , b) $n = 1/4$ , c) $n = 1/2$ , d) $n = 1$ , e) $n = 2$ and f) $n = 4$ for different values of $t$ .....	96
Figure 4.6	Influence of the nonlinear imbibition on the hygro-mechanical bending strain state cycle.....	98
Figure 4.7	Total strain distribution along $z$ as a function of $t$ for the case of nonlinear imbibition. The nonlinear effect is studied by means of the exponent a) $n=0$ , b) $n=0.25$ , c) $n=0.5$ , d) $n=1$ , e) $n=2$ , and f) $n=4$ . Black lines represent contours at $\varepsilon = 0$ . Zones T and C stand for regions experiencing tension and compression, respectively. ....	101
Figure 4.8	Influence of the nonlinear softening effect on the hygro-mechanical bending state cycle. Right-hand side image represents the magnification of the insert <i>i-iv</i> . ....	103
Figure 4.9	Total strain distribution along $z$ as a function of $t$ under the influence of nonlinear softening. The nonlinear effect is studied by means of a) $m=0$ , b) $m=0.5$ , c) $m=0.1$ , d) $m=0.05$ , e) $m=0.001$ , and f) $m=0.005$ . The contours at $\varepsilon = 0$ are represented as black lines. Zones T and C stand for regions experiencing tension and compression, respectively. ....	105
Figure 4.10	Influence of the nonlinear swelling on the hygro-mechanical bending state cycle. ....	106
Figure 4.11	Total strain distribution along $z$ as a function of $t$ under the influence of nonlinear swelling. The nonlinear effect is studied by means of the exponent a) $p=0.25$ , b) $p=0.5$ , c) $p=1$ , d) $p=2$ , and e) $p=4$ . The contours at $\varepsilon = 0$ are represented as black lines. Zones T and C stand for regions experiencing tension and compression, respectively. ....	108

Figure 4.12	Comparison of the curvature response using the proposed model including nonlinear imbibition with experimental results presented in [59]. The RMSE for the proposed model is $0.009 \text{ mm}^{-1}$ . In addition, the attempt to match the experimental result with the model developed in [59]. The RMSE for this attempt is $0.120 \text{ mm}^{-1}$ . .....	112
Figure 5.1	Proposed configuration of the PB-HMS. The sensing element is a paper-based cantilever beam of length $l$ and thickness $h$ . The bending response is triggered by a small droplet that wets a portion $b_{wet}$ of the cantilever length.....	118
Figure 5.2	Time lapse side view of paper-based microcantilever beam experiencing hygro-expansion along both cross (CD) and machine (MD) direction.....	119
Figure 5.3	Fabrication process of the paper-based cantilever beams. a) A rectangular area is added to the cantilever beam for holding purposes. b) The design is implemented using CAD. c) The paper is placed on an electronic cutter. d) The paper-based elements are cut. f) A fabricated paper-based cantilever beam is compared to the size of a one Canadian dollar coin. ....	121
Figure 5.4	Measurements of the hygro-mechanical bending response. a) Experimental setup and b) a detail of the cantilever holder. c) The portable microscope and d) the mechanical pipette used to deposit the fluid droplet on the surface of the cantilever beam. ....	122
Figure 5.5	Image processing method to evaluate the bending angle of the paper-based cantilever beam using ImageJ.....	124
Figure 5.6	Dynamic response of paper-based cantilever beams C1 and C2. Bending angle response of a) C1 and b) C2. c) and d) represent their first derivative with respect to time. Time sample recording is 2s and 1s for C1 and	

	C2, respectively. In each case the number of experiments carried out was N=7.....	126
Figure 5.7	Dynamic response of paper-based cantilever beam C1 under the influence of a-b) water, c-d) water-methanol and e-f) water-hydrogen peroxide. The bending velocity ( $\Omega'$ ) is presented in the left column, while the bending acceleration ( $\Omega''$ ) on the right column. Time sample recording is 2s, and bars represent the standard deviation for N=7. ....	130
Figure 5.8	Dynamic response of paper-based cantilever beam C2 under the influence of a-b) water, c-d) water-methanol and e-f) water-hydrogen peroxide. The bending velocity ( $\Omega'$ ) is presented in the left column, while the bending acceleration ( $\Omega''$ ) on the right column. Time sample recording is 1s, and bars represent the standard deviation for N=7. ....	132
Figure 5.9	Phase portrait of the dynamic response of the cantilever beams a) C1 and b) C2 under the influence of water. The black line represents the phase portrait of the average response. Color points represent experimental measurements using N=7. Sample recording is 2s and 1s for C1 and C2, respectively.....	133
Figure 5.10	Phase portrait of the dynamic response of the cantilever beams a) C1 and b) C2 under the influence of water-methanol solution. The black line represents the phase portrait of the average response of water. Color points represent experimental measurements using N=7. Sample recording is 2s and 1s for C1 and C2, respectively.....	135
Figure 5.11	Phase portrait of the dynamic response of the cantilever beams a) C1 and b) C2 under the influence of water. The black line represents the phase portrait of water. Color points represent experimental measurements	

	using $N=7$ . Sample recording is 2s and 1s for C1 and C2, respectively. ....	136
Figure 5.12	Phase portrait of the dynamic response of the cantilever beams a) C1 and b) C2 under the influence of glycerol. The black line represents the phase portrait of water. Color points represent experimental measurements using $N=7$ . Sample recording is 2s and 1s for C1 and C2, respectively. ....	137
Figure 5.13	Phase portrait of the dynamic response of the cantilever beams a) C1 and b) C2 under the influence of sucrose. The black line represents the phase portrait of water. Color points represent experimental measurements using $N=7$ . Sample recording is 2s and 1s for C1 and C2, respectively. ....	138
Figure 6.1	Comparison of the estimated transfer function $H_5(s)$ and $H_9(s)$ with the experimental acceleration of cantilever C2 under the influence of distilled water. a) Time response signals and b) absolute errors. ....	145
Figure 6.2	Bode plot of the identified hygro-mechanical system corresponding to Fig. 6.1 a) magnitude and b) phase. Both resonance and crossover frequencies are illustrated along with their respective gains peak and margin. ....	147
Figure 6.3	Close loop configuration of the hygro-mechanical system under a proportional gain $K$ . $U(s)$ and $Y(s)$ stand for the step input and the virtual bending acceleration, respectively. ....	148
Figure 6.4	Root locus plot of the hygro-mechanical system presented in Fig. 6.1. ....	149
Figure 6.5	Virtual bending acceleration due to a step input of the close loop system exhibiting stable and instable behavior for $K=6$ and $K=7$ , respectively. ....	150

Figure 6.6	Characterization of water-methanol solutions by means of the resonance frequency a) methanol, and b) sucrose solutions (N=7). .....	152
Figure 6.7	Characterization of water-methanol solutions by means of a) hygro-mechanical system using its gain margin (N=7) and b) refraction index via a digital refractometer (N=7). .....	154
Figure 6.8	Characterization of water-sucrose solutions by means of a) hygro-mechanical system using its gain margin (N=7) and b) refraction index via a conventional refractometer (N=7). .....	155
Figure 6.9	Identification chart (crossover frequency against gain margin) of hydrogen peroxide aqueous solutions. Hydrogen peroxide (N=21) exhibit a different trend compared to the methanol, sucrose and glycerol solutions (N=70). .....	158
Figure 6.10	Sematic representation of the distance from the reference line to a characteristic point A ( $fc_A$ , $Gm_A$ ) of a given hygro-mechanical system. ....	160
Figure 6.11	Evaluation of the distance $d$ using Eq. (5.4) to determine a threshold between typical and abnormal hygro-mechanical systems. Typical hygro-mechanical systems $d < 2.8$ , and abnormal hygro-mechanical systems $d > 2.8$ . .....	161

## List of Tables

Table 1.1	Summary of the paper-based mechanical devices reported in the open literature. ....	10
Table 2.1	Physical properties of water [137].....	45
Table 2.2	RMSE and maximum relative errors of imbibition along the center line for various values of $n$ . ....	47
Table 3.1	Equivalent functions $f_i$ for LW case.....	80
Table 4.1	Equivalent functions $f_i$ for accounting for nonlinear influences.....	89
Table 4.2	First five values of $\lambda_{iz}, a_i$ and $b_i$ of Eqs. 4.2, 4.5 and 4.7.....	90
Table 4.3	Relative error on curvature and bending strain reference due to nonlinear geometry. ....	94
Table 4.4	Dependence of the five necessary parameters to describe the hygro-mechanical response of paper-based beams. ....	110
Table 4.5	Parameters used in the proposed model to describe the experimental results presented in [59]. ....	112
Table 5.1	Properties of cantilever beams C1 and C2.....	120
Table 6.1	Parameter setting applied on the hygro-mechanical system identification.....	143
Table 6.2	Fits values of the different identified hygro-mechanical systems. ....	144
Table 6.3	Sensitivity of tested binary aqueous solutions using both gain margin and index refraction by means of PB-HMS and refractometer, respectively.....	156
Table 6.4	Comparison of the features of the proposed hygro-mechanical detection with other commercially available techniques. ....	163

# Chapter 1 Introduction

*This chapter provides an introductory overview of the evolution of paper-based devices from silicon-based microsystems to the current state of paper-based systems. Then, the rationale of this research is described based on the current state-of-art related to paper-based systems. The main contribution of this research is to develop a paper-based sensor based on hygro-mechanical detection for characterization of bio-fluids. Four main areas of knowledge involve in this research are identified: cantilever biosensors, hygro-mechanical systems, paper-based microfluidic and imbibition of porous media. A literature review regarding these areas is presented in order to define the particular objectives of the research. Finally, this thesis is divided into six chapters, which content is outlined in the last section of this chapter.*

## 1.1 From Microsystems to paper-based systems

Microsystems have revolutionized several markets developing miniature devices for several applications. Among the subcategories of microsystems are MEMS (Micro-electromechanical systems), bio-MEMS, microfluidics, and microelectronics. Several studies have been conducted to develop microdevices such as micro-actuators, lab-on-a-chip, micro-antennas, and micro-sensors. Perhaps the most common examples of the impact of microsystems are the mobile communication and the automotive markets. Microsystem technologies have been consolidated in these markets over the past few years [1]. The development of smart devices in both areas has been possible due to the availability of small and robust sensors and actuators. Smart devices are also found in other areas of development such as radio frequency [2-5], energy harvesting [6-10] and health care [11-13] applications. According to a recent market research report by Technavio, the compound annual growth rate will be 25% for microsystem market in healthcare[14].

Nowadays, health care market demands reliable and low cost devices, which must perform quick and accurate analysis. In this regard, the huge challenge for scientists is to improve or to develop new devices for real-time biomedical assays. These devices must be suitable for large-scale production. Finding the appropriate designs, which allow easy fabrication of microsystems without compromising their performance, is still a challenge in the research community. Recently, micro- and nano-

mechanical biosensors have become powerful tools in different areas such as biological studies, health science research, drug discovery and clinical diagnosis [15].

In particular, microcantilever sensors, as the one developed for atomic force microscopy (AMF) [16], have become one of the most important types of mechanical biosensors, since they exhibit remarkable features such as high sensitivity, low cost as well as multiple and free-label detection [17, 18]. Microcantilever biosensors can be operated under static or dynamic mode. In static mode, the microcantilever bends due to change in the surface stress, while in the dynamic mode these microstructures oscillate at resonance to detect frequency shifts due to the added mass of specific targets.

According to Calleja et al. [18] these types of biosensors can be classified according to their functionality as (i) detection or concentration measurement of a particular analyte in solution; (ii) measurement of a specific property of the analyte for either classification or identification; or (iii) observation, characterization or analysis of a specific biological process. Microcantilever biosensors have partially solved issues regarding the study of diverse types of bioanalytes. However, there are still some drawbacks to overcome in order to significantly potentiate their capabilities. There are issues regarding their sensitivity as well as detection limit in natural environments, usually liquids (i.e. buffers and serums). In this kind of media, the performance of the microcantilever

biosensors is extremely limited due to the strong effect of the hydrodynamic forces in the surrounding media.

In addition, many applications as in the biological field required disposal sensors to avoid cross contamination. Therefore, the need of devices that can be both affordable and disposable has also been another concern in the design of microsystems. In the last decade, MEMS have evolved from silicon-based devices (Silicon, Silicon Nitride, and Silicon Dioxide) to a diversity of alternative materials. The most common examples of these materials are polymers such as polydimethylsiloxane (PDMS), which has been extensively used to develop microsensors [19-22], microactuators [23-25] and microfluidic devices (Lab-on-a-chip) [26, 27]. Other polymer-based microsystems have been reported using SU8 [28], polyimide [29], parylene C [30] and polyvinyl chloride [31]. These materials have simplified the fabrication process of microsystems; however, one the main drawbacks of these polymers is that they are not biodegradable.

As paper is made of cellulose that is a biopolymer, it has acquired special attention for many research groups in the microsystems community. In the past decade, several paper-based sensors and actuators have emerged as an alternative to performing same tasks as microsystems. Kim et al. [32, 33] introduced the concept of electro-active paper actuators (EAPad) at the beginning of the 2000s. This system consists of a piece of paper sandwiched between two compliant electrodes. The bending response of this paper-based structures depends on the characteristics of the electric potential applied to the electrodes, magnitude, and frequency.

Later, Lee [34] presented the first urine-activated paper-based battery in 2005. In his work, Lee focused on the need to develop simple devices that may produce energy without complex processes of fabrication as those found in microsystems. This device was capable of generating electrical energy based on chemical reactions induced by the bio-fluid. Two years later, Whitesides and co-workers from Harvard University introduced the concept of paper-based microfluidic systems [35]. They presented a device to perform multiple analytical assays in a single piece of paper by selectively patterning channels.

Thus, from a general point of view all of these devices can be considered as paper-based systems. These paper-based devices exhibit several advantages with respect to their counterparts microsystems made of silicon and/or polymer. Their principal advantages are:

- i. Paper is inexpensive, and the most important, it is readily available in several types.
- ii. The fabrication methods of these devices are simple. In fact, they involve conventional technologies that have been already applied to paper products (i.e. screen, inkjet and laser printing).
- iii. They are extremely portable since their size is small, usually in the range of millimeters.
- iv. The volume of the sample and the analyte that are required to perform an analytical assay is small, usually in the microliter range.

- v. The flow in these devices is self-driven by capillary action, and no external hardware is needed.
- vi. They are highly disposable; therefore, any biological waste can be simply disposed by incineration of the device.

## 1.2 Rationale

Nowadays, almost one decade after the first work related to electroactive paper actuators was published, the knowledge regarding paper-based systems is still in infancy. Figure 1.1 shows the number of papers published per year regarding paper-based systems. In past years paper-based microfluidic devices have been extensively studied. In the past four years more than 400 publications have been published in the open literature. There is a clear tendency to maintain its growth in the upcoming years. The first patent on paper-based microfluidic systems has been granted to Whitesides' research group in 2014. In contrast, electroactive paper actuators and paper-based batteries have not received the same attention in past years. Only 172 and 125 research papers have been published since 2011 on electroactive papers and paper-based batteries, respectively. Moreover, it can be seen that the number of publications per year regarding the paper-based microfluidics devices is still increasing compared to the other two areas.

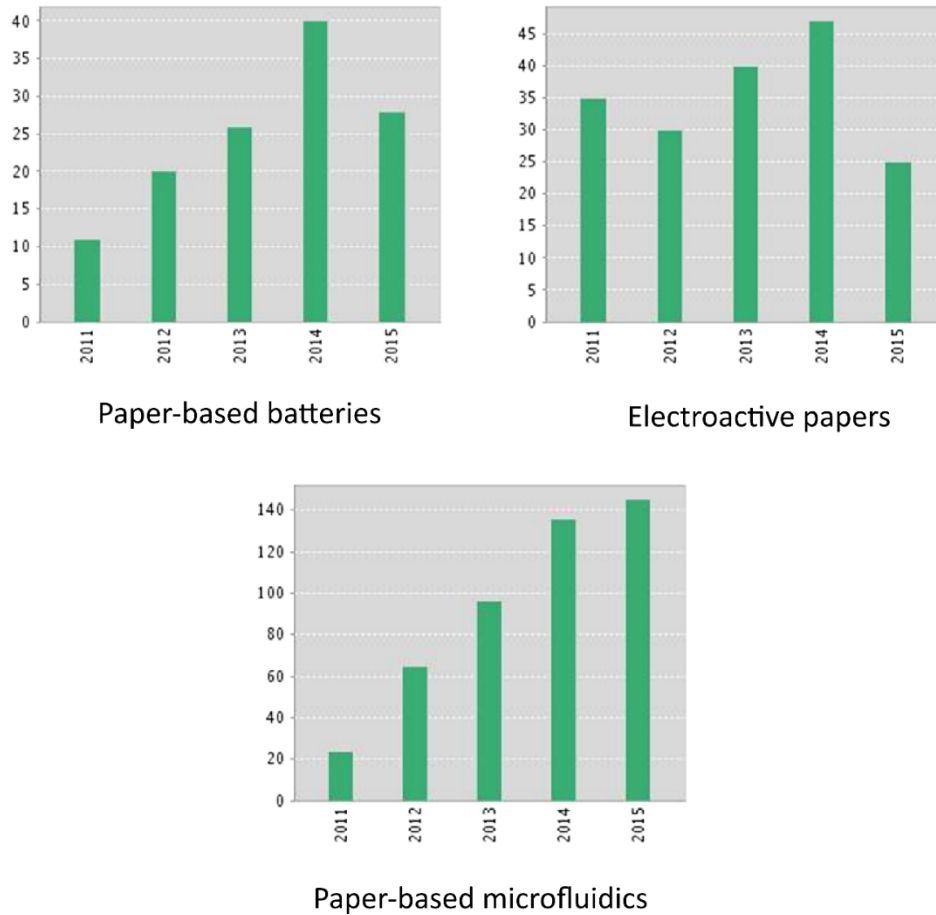


Figure 1.1 Number of publications per year of paper-based microsystems. Source: citation reports Thompson Reuters<sup>1</sup>.

Up to date, only few works have been published in the literature regarding paper-based mechanical devices. Liu et al. [36] presented a force sensor fabricated using paper as a substrate. They fabricated carbon resistors on a cantilever beam by screen printing method [37]. They named their device as a MEMS sensor due to the similarities with those

<sup>1</sup> <http://apps.webofknowledge.com/>

microcantilever sensors made of silicon. Nevertheless, the cantilever size (~cm) is quite large compared to those at the micro-scale. An extension of this work was presented by Ren et al. [38]. They simplified the fabrication process by directly writing graphite resistors using a pencil. In addition, paper-based magnetic actuators have been presented by Liu et al. [39] and Ding et al. [40]. These actuators were magnetized by impregnating the paper substrate with a ferrofluid. Cheng et al. [41] developed an electrostatic paper-based actuator using inject printing technology. Finally, Fraiwan et al. [42] developed a paper-based cantilever sensor. The cantilever beam was fabricated by spin coating a strain sensitive polymer on paper.

The main characteristics of these devices are summarized in Table 1.1. It can be seen that both paper-based sensors and actuators promise an excellent alternative for several applications such as mechanical characterization of soft materials [36], microfluidics valves [39], volatile compounds detection [42] and robotics [41]. All of these works used a cantilever beam structure as either sensing or actuation element. All these devices work in the static domain, except for the electrostatic actuator in [41] that was tested in both static and dynamic mode. According to Liu et al. [36] this type of devices are restricted to work in the quasistatic mode due to the softness of paper. However, this softness feature of paper also brings certain advantages such as large deflection responses that can be easily detected and/or measured even with a bare eye [42].

Most of these works have used either chromatography or printer paper to develop their devices. The first is a standard laboratory degree paper that provides a high degree of consistency in mechanical properties. On the other hand, printer paper is highly available at a very low price (approximately 100 letter-sized sheets per Canadian dollar). A discussion of the influence of types of paper have been presented in [40] for the development of magnetic actuators. The authors concluded that papers with more ferrofluid retention capacity, such as tissue and wipe papers, are more suitable to develop this type of paper-based actuators.

The detection or actuation principle applied in research works presented in Table 1.1 represent well known techniques such as magnetic and electrostatic principles. For sensing purposes, both piezoresistive and polymer swelling methods have been applied. It is interesting to note that in all of these devices paper plays only a structural role. A sensing/actuation element has to be included in the paper structure in order to achieve the specific task. In this regard, piezoresistors, electrodes or active layers have to be deposited on paper. Another type of paper-based devices may be developed by combining paper features with alternative

Table 1.1 Summary of the paper-based mechanical devices reported in the open literature.

References	Application	Substrate	Principle	Sensing/actuation element
Liu et al. [36]	Sensor	Chromatography paper	Piezoelectric detection	Carbon resistors
Ren et al. [38]	Sensor	Printer paper	Piezoelectric detection	Carbon resistors
Fraiwan et al. [42]	Sensor	Chromatography paper	Polymer swelling	Polymer active layer
Liu et al. [39]	Actuator	Chromatography paper	Magnetic	Ferrofluid
Ding et al. [40]	Actuator	Tissue paper, cleanroom wiper, filter paper, printer paper newspaper	Magnetic	Ferrofluid
Cheng et al. [41]	Actuator	Printer paper	Electrostatic	Electrodes made of carbon nanotube ink

sensing/actuation principles. Paper-based mechanical devices represent a niche of opportunity to fulfil the needs of specific sensing and actuation applications.

From a physical point of view, paper offers unique features that facilitate the development of paper-based systems. Paper-based microfluidic devices have taken advantage of the ability of paper to transport liquids and the chemical compatibility to launch several microfluidic applications [43, 44]. However, paper has other properties that can also be exploited to extend the functionality of paper-based systems. One of the characteristic of paper that has not been fully explored is the hygro-mechanical actuation. In nature, several actuation systems found in plants are based on the differential swelling on their walls due to the daily change of humidity in the surrounding environment, known as hygroscopic motion [45-47]. These movements include bending, twisting and coiling [45]. Some studies have been carried out to study hygroscopic motion in pine cones [48], geraniaceae plants [49], and *salaginella lepidophylla* [50]. Since paper is made of natural highly hygroscopic fibers (i.e. cellulose), it is an excellent option for developing paper-based hygro-mechanical devices for either actuation or sensing purposes.

The hygro-mechanical motion of paper has been studied as a physical phenomenon. Several investigations have been conducted to study the bending response of hygroscopic sheets due to changes of relative humidity [51-55]. The moisture transport in this type of environment has

been modeled as molecular diffusion [56, 57]. The motion of this type of structures has to be controlled by modifying the relative humidity of the environment. Such a task requires an external hardware to produce moisture gradients that allow the motion of the paper-based structures. This need of external driving elements represents a limitation to develop portable sensing and/or actuation devices.

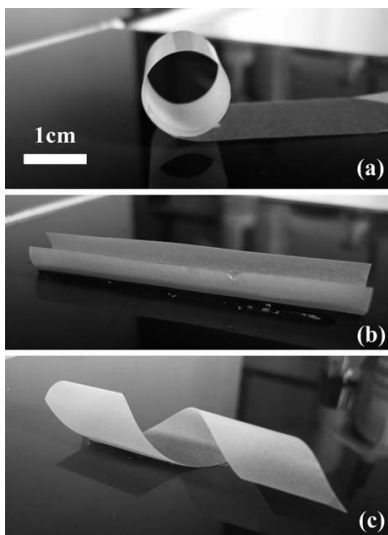


Figure 1.2 Hygro-bending response of a paper strip a) along the cross direction CD b) parallel to the MD c) longer dimension is oblique to the MD. Reproduced from Ref. [58] with permission from The Royal Society of Chemistry.

Recently, the curling response of surface treated paper due to its interaction with water has been reported [58, 59]. The main difference of these works is the moisture source. Here, the motion is produced by the imbibition of water into the paper rather than the relative humidity change in the environment. In these two works a piece of tracing paper was laid on

a water bath; then, a transient bending response is generated as the water penetrates the paper along its thickness. Imbibition into paper dominates the hygro-mechanical response of the paper-based structure. However, two inherent phenomena related to the water imbibition into the structure have a fundamental role in the bending response [60]. First, the fibers of paper swell as their moisture content increases, namely hygroexpansive strain. Second, an apparent relaxation of the bending stiffness occurs as the moisture content in the fibers increases.

When placing a paper beam on a water surface, its initial moisture content is modified. Thus, a gradient of moisture is formed from high content at the contact of the paper beam with water to low content at the opposite surface. This gradient of moisture induces a differential of hygroexpansive strain that yields to a transient bending state (see Figure 2). The final bending state is achieved when the moisture transport reaches its steady state equilibrium. These investigations have shown the feasibility to produce a motion of paper using water, namely hygro-motion. Reyssat et al. [59] and Douezan et al. [58] present a comprehensive explanation of this phenomenon by introducing physical models. They showed that the curling response is dominant along the cross direction as depicted in Figure 1.2a-c. Nevertheless, their models are not capable of predicting the bending response of the paper-based structures due to the lack of deep understanding of the phenomena involved in this problem. In order to develop paper-based hygro-mechanical systems a deeper understanding of such phenomena is needed.

The main purpose of this research is to extend the current knowledge of paper-based systems. Particularly, the main contribution of this research is to develop a paper-based hygro-mechanical sensor for characterization of liquids. Compared to the paper-based mechanical devices summarized in Table 1.1 the proposed sensor has several advantages. In this type of sensor, paper acts not only as a substrate but also as an active element for generation of motion. Thus, no external sensing or actuation element is needed. In addition, the hygro-motion is generated by a small droplet of the fluid to be tested. Then, no external hardware such as electric supplies or magnets is needed. These features in addition to those stated in section 1.1 are extremely important for performing portable liquid characterization tests.

### 1.3 Literature review

The knowledge related to the paper-based hygro-mechanical sensor can be described in the intersection of four areas as illustrated in Fig. 1.3. As this type of sensors has not been reported up to date, the region where these four areas, shown in Fig. 1.3, intersect remains unexplored. Thus, it is important to review the works that have been conducted in these four areas in order to develop such hygro-mechanical sensor.

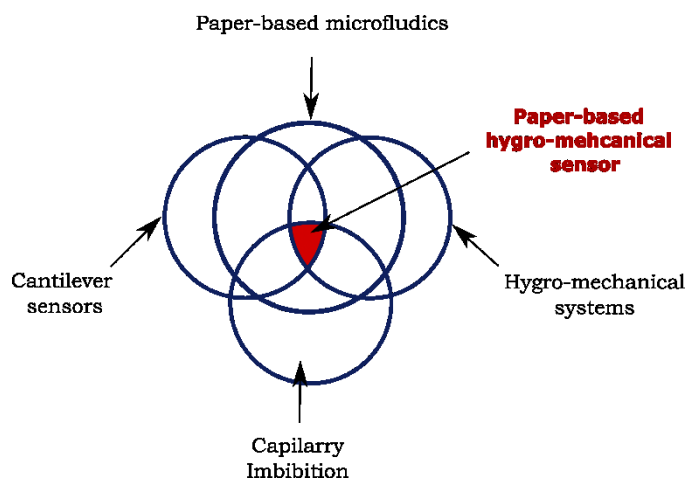


Figure 1.3 Areas of knowledge involved in the proposed paper-based hygro-mechanical sensor.

### 1.3.1 Cantilever sensors

In dynamic mode (resonant-mode), microcantilever sensors oscillate at their resonance frequency and act as microbalances. This mode can provide high sensitivity and less time response compare to the static mode. Here, the cantilever surface is typically functionalized with coatings that can promote adhesion of target molecules [61]. When the analyte is trapped on the selective layer the resonance frequency shifts proportionally to the added mass. Here, measurements of frequency shifts are crucial, since this added mass could change due to different factors (i.e. living matter growing). The dynamic method has been widely applied to biological measurement, where the native environment is liquid media [62]. However, in this environment the mass sensitivity of microcantilever sensors is severely reduced by the inertial and damping effects [63-65].

A good alternative to overcome the hydrodynamic forces when characterizing liquid by means of microcantilever beams is to excite the microcantilever beams at alternative modes of vibration. It has been established in different works that driving microcantilever beams at high out-of-plane [66], lateral [67] and torsional [68] modes can significantly reduce the hydrodynamic force effects. However, driving the microcantilever beams at these alternative modes represents a technical challenge due to the amount of energy required and the spurious vibration induced by the motion of the liquid [69]. In this light, some researches have applied diverse driving methods of excitation such as magnetic [70], thermal [71] and Lorentz force actuation [65] to excite microcantilever beams immersed in liquids. However, most of these techniques require complex hardware that limits the portability of the sensing platform.

Another solution to overcome the hydrodynamic force when sensing bio-fluids was presented by Burg et al. [72] from Massachusetts Institute of Technology. This innovation consists on introducing the liquid sample inside the microcantilever beam instead of immersing the beam in the liquid. This novel design consists of a microcantilever beam with a u-shaped microchannel inside. The resonance frequency is continuously monitored as a sample is passed through this path. Thus, the weight of biomolecules, single cells and single nanoparticles in the fluid can be determined by the shift in the resonance frequency. In another similar example, Wang et al. [73, 74] proposed a design that includes a microcavity with micropillar arrays to increase the sensitivity of the

antigen-antibody reaction. This microcantilever design has been applied for the detection of multiple liver cancer biomarkers. The results reported for the authors represented a considerable improvement of the sensitivity compare to conventional microcantilever designs. Nevertheless, the main limitation of these designs lies in their complex fabrication process.

Other researches have focused on the migration from microcantilever sensors under dynamic mode to cantilever sensors in the millimeter scale, known as milicantilever. Among them, only piezoresistive milicantilever sensors, which were developed by Mutharasan and coworkers at Drexel University, have been successfully applied as biosensors [75]. The research group reported a method to measure DNA hybridization at femtomolar concentrations in human serum using milicantilever beams [76]. This method has been applied by the authors to develop DNA-based milicantilever sensors rather than the conventional antibody-antigen methods. This type of configuration offers several advantages such as clear identification of several pathogens along with a simple readout hardware. For instance, using this platform the authors have been able to detect *E.coli* 0157:H7 in proteins background [77]. In another example, *Listeria monocytogenes* in milk have been detected using the same method [78].

Finally, another interesting alternate use of cantilever beams in static mode for biosensing applications is to favorably use the solid-liquid surface tension produced by molecular interactions, known as capillary force. Among the main advantages is the large deflection response, which can be easily detected by optical read-outs compared to those very small

deflections in the surface stress sensors. For instance, Jeetender et al. [79] achieved the identification of enzymatic reactions by measuring the quasi-static deflection of a microcantilever. In another case, Yin et al. [80] developed a microcantilever based sensor for biodetection using ligand-receptor protein interaction using capillary interactions. However, one major limitation in these works is the limited understanding of the capillary interactions with the cantilever beam. This drawback represents a major limitation to explore the capabilities of these methods.

### 1.3.2 Hygro-mechanical systems

Besides the conventional attractive and repulsive forces (i.e. electrostatic and magnetic fields), the swelling differential has been applied for generating motion in microsystems. The most suitable example of similar behavior is the bilayer thermostat, in which the resultant bending state is due to the difference in the thermal strain due to a temperature variation. Recently, bending response due to swelling of soft materials has been applied not only for actuation [81] but also for detection purposes [82]. The most common examples are hydrogels. The swelling/deswelling of hydrogels can be controlled by changing environmental parameters such as temperature, pH, electrical field, and concentration of specific ions [81, 82]. Another example is the liquid crystals elastomers that swell due to temperature changes and light [83, 84].

In recent years, some devices that transform moisture into motion have been developed, namely bilayer hygro-mechanical devices. These devices

are formed by two layers similar to those formed in plants [45, 48-50]. The one that is sensitive to moisture is known as active, while the other is known as passive. Le Duigou and Castro [55] used unidirectional flax fiber tape embedded in polypropylene film as active layer. Yao et al. [54] developed a graphene oxide/silicon microbridge by spin coating graphene onto the silicon structure. Cheng et al. [85] developed a graphene/graphene oxide bilayer cantilever beam. The bilayer is made by selectively removing graphene oxide on the graphene fiber using a laser beam. Ganser et al. [86] developed a mesoporous silica/silicon microcantilever bilayer actuator activated by moisture source. In all these cases the moisture source is obtained by variations of the relative humidity in the environment. It is interesting to note that up to date these type of hygro-mechanical systems have been only applied to develop humidity sensors [54].

Several studies have been conducted to investigate the bending response of multilayer hygro-mechanical devices. Rafsanjani et al. [50] carried out a study on the curling response of the resurrection plant *Salaginella lepidophylla*. The authors characterized the bending response of a stem as a bilayer beam with constant cross section area. They presented a comparison of the Timoshenko bilayer model and a finite element model that accounts for large deflections. Their results suggested that the Timoshenko theory provides a reasonable approximation of the bending curvature for moderate hygroexpansive strains less than 20%.

In another study, Gendron et al. [57] performed a theoretical study of the hygro-mechanical deformation of a three layered cardboard. The mechanical response was evaluated using von Karman nonlinear strain displacement relationship. They presented the bending response of the cardboard for different moisture changes. Though both studies were focused on the mechanical response, the authors did not discuss the moisture transport in the system. Latter, Dano and Bourque [56] presented a multilayer model for the deformation of paper and card board. The mechanical part is similar to that proposed by Gendron et al. [57]; however, a diffusion moisture transport model was considered in this work. This type of moisture transport has been applied on different researches to model moisture transport under a gradient of relativity humidity.

Recently, hygro-mechanical systems driven by capillary imbibition of bilayer and single structures have gained special attention within the research community. Reyssat et al. [48] studied the bending response of a paper-polymer bilayer cantilever beam due to imbibition of water into the paper. The fixed end was exposed to water; then, the imbibition of water induces the hygroexpansive strain on the active paper layer. The authors applied Timoshenko and Washburn-Lucas [87, 88] theory to model the mechanical and imbibition responses, respectively. In another work, Lee et al. [60] studied the bending and buckling response of wet strips of filter paper. They modeled the out-of-plane deformation assuming one-dimensional infiltration of water along the horizontal direction. However,

as it can be discussed later this type of infiltration models are limited to simple geometries as those rectangular shapes studied by the authors.

In another work, Reyssat et al. [59] and Douezan et al. [58] studied the curling response of a strip of tracing paper in contact with water using a one dimensional approach. Douezan et al. [58] modeled the mechanical response of the problem using Timoshenko bilayer theory. In this work, the water transport into the paper strip started by assuming Lucas-Washburn theory. Then the active layer was considered as wet without taking into account the gradient of water content within its thickness. The model presented by the authors is only valid in the vicinity of the maximum bending curvature. On the other hand, Reyssat et al. [59] presented a discussion of the water transport into the paper strip started by initially assuming Lucas-Washburn theory. Then, they suggested that molecular diffusion drove the water penetration into the paper strip. However, no detail on the theory behind this kind of phenomena was provided by the authors. The model developed in this work presents good agreement for long term curvature response. The omission on the water transport theory in the paper-based network makes it difficult to develop an accurate prediction of the hygro-mechanical response of the paper-based structure.

### 1.3.3 Paper-based microfluidics

In the last decade paper-based microfluidic analytical devices have emerged as attractive options in different areas including medical diagnosis, food safety and environmental monitoring. Here, analytical

assays can be performed without the need for external pumps as the flow is driven by capillary imbibition. Whitesides and co-workers [35] developed a paper-based microfluidic device by patterning channels using a polymer through photolithography. One example of these devices is presented in Fig. 1.4, whose inlet is connected to different test zones. Each detection zone has to be chemically modified to enable a specific reaction with the substance to be detected. The chemical detection can be carried out by different methods such as colorimetry, electrochemical, nanoparticle-based, fluorescence, chemiluminescence and electrochemiluminescence [89].

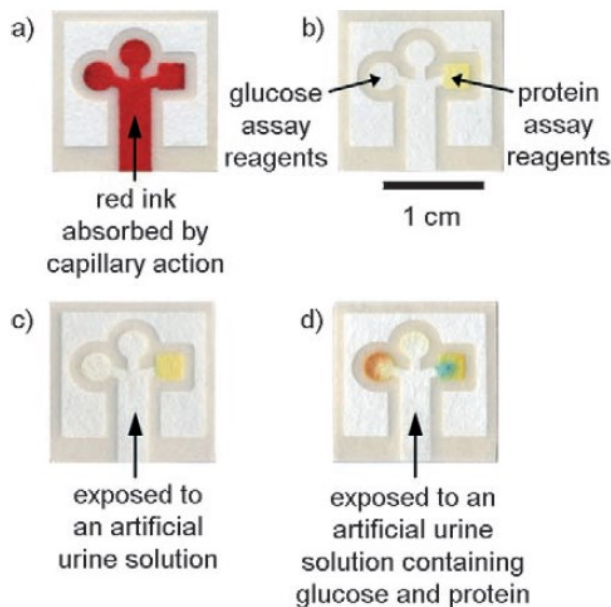


Figure 1.4 Paper-based microfluidics systems patterned with photoresist. Reproduced from Ref. [35] with permission from John Wiley and Sons.

Several reviews have summarized the works done related to these devices [43, 90]. Other reviews have been focused on particular subjects such as diagnostic tests for biosensing [89, 91], and as well as detection [92, 93] and fabrication [94, 95] techniques. In 2012 Li et al. [90] presented a review of the current status and future trends of paper-based microfluidics. The authors conclude that further research related to capillary imbibition into paper samples will be necessary to tune the control of capillary flow.

Up to date only few theoretical works have been conducted to investigate capillary imbibition into paper-based devices. Some authors have proposed the idea of migrating from the conventional rectangular channels to different geometries to control the capillary flow without adding external hardware. Fu et al. [96] provided simple design rules for controlling the delivery time using rectangular channels with a sudden width expansion. Here the reactant delivery can be tuned by positioning the width expansion at a specific location along the length of the channel.

In another work, Elizalde et al. [97] developed a theoretical solution to the inverse imbibition problem on a channel with variable width. This solution to the inverse problem is important as it is possible to determine the cross section needed to achieve either a specific flow velocity or mass transport rate. Nevertheless, both works were performed using equivalent models. Thus, a general frame work that provides a better understanding of the transport in this type of paper-based networks is needed to achieve new design rules.



Figure 1.5 Mixing using filter paper. Reproduced from Ref. [98] with permission from Elsevier.

Moreover, alternative applications of paper-based microfluidics using two-dimensional domains have been presented in the literature such as mixers [98]. In this work, the authors experimentally study the mixing process on filter paper. It can be seen in Fig. 1.5a that it was possible to perform the mixing task using rectangular channels. However, the authors suggested that it was difficult to control the mixing rate and estimate the diffusion area. They proposed a redistribution of the diffusion area by means of circular perforations to tune the mixing rate, Fig. 1.5b. Thus, it suggested that alternative geometries may be important to tune and/or enhance the design of paper-based microfluidic devices. However, one of the main challenges for developing paper-based systems is to understand the liquid transport within the paper sample of both conventional and non-conventional geometries.

### 1.3.4 Imbibition models in porous media

The flow driven by capillary action in porous media is known as imbibition and is the principal mechanism of transport in porous paper-like materials. This type of transport is dominated by both the liquid and the porous media properties. The liquid imbibition in the media can be studied at both micro- and macro-scale. In the micro-scale, also known as pore-level transport [99-102], the connectivity of the pore structure has to be determined in order to solve the problem. This study provides an accurate solution of the problem; however, it represents a challenging task due to the complexity of the porous structure. One of the most recognized techniques to simulate the transport at the micro-scale is the lattice-Boltzmann method [103]. On the other hand, a macroscopic representation of the porous media provides a reduced model to characterize the capillary flow. In this case the properties of the imbibition problem are represented as an average of the one at the microscopic level. Such models enable the development of either numerical or analytical solutions to describe the imbibition dynamics.

The macroscopic models for liquid infiltration in porous materials can be divided into two main categories: capillarity and soil-based models. The first one, which is based on the Washburn-Lucas [87, 88] theory, assess the one dimensional imbibition in porous media. In this kind of models, the imbibition can be represented as a bunch of capillaries tubes of different diameter which can be reduced into a single equivalent tube. In

general, the governing equation of the capillary tube models can be derived by combining the Hagen-Poiseuille and Laplace-Young equations. The second type are the soil-based models, which are obtained by the combination of the governing equations for fluid motion (Navier–Stokes) and mass conservation law. In particular, assuming a laminar flow and neglecting the inertia forces the solution becomes the well-known Richards’ equation [104]. Both models offer different features to model imbibition in porous media.

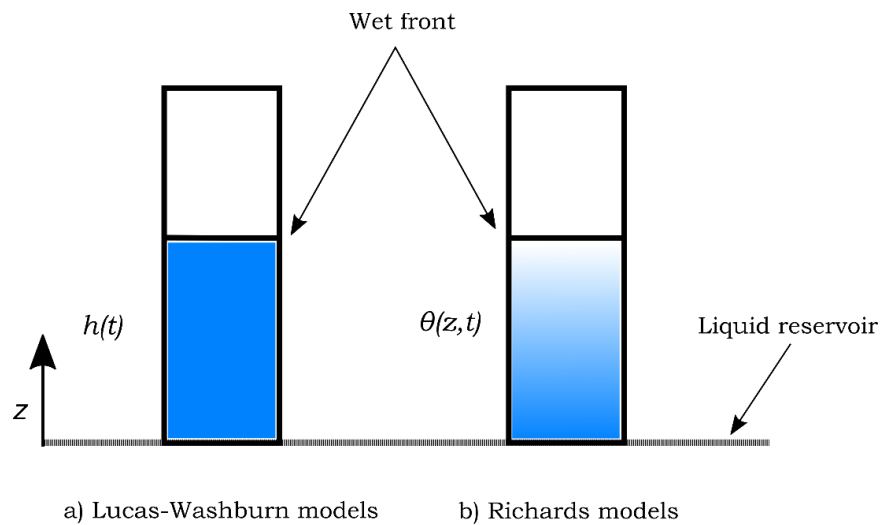


Figure 1.6 Imbibition in a rectangular porous material using a) Lucas-Washburn and b) Richards’ models.

Another important issue regarding paper-based systems is the gradient fluid content distribution during imbibition. This feature plays an important role in the study of the hygro-mechanical bending response where the evaluation of moisture gradients is needed to establish the hygroexpansive strain. Fig. 1.6 depicts this difference between both capillary and Richards’s models to evaluate the imbibition on a rectangular

porous domain. On one side, Richards' models, can predict the content distribution of liquid within the porous media  $\theta(z,t)$  using its volumetric content form. In contrast, capillaries analytical models lead to the solution of the wet front  $h$  as a function of the time. In this particular case a discrete boundary between the saturated and unsaturated zone is considered. In other words, the media is considered as a binary state either wet or non-wet zone.

## 1.4 Objectives and thesis outline

It can be concluded from the literature review that there are few gaps in the knowledge that have to be addressed in order to develop the proposed paper-based hygro-mechanical systems. First, a better understanding of the fluid imbibition into paper-based structures is needed in order to develop future applications. Currently, Lucas-Washburn (LW) theory has been applied to describe the liquid imbibition into paper networks. However, this model is limited to liquid transport in one dimension and constant cross section areas as that in a circular capillary tube. Second, a better understanding of the hygro-mechanical response of paper under the influence of water is needed. Currently models are not accurate when predicting the whole time bending response. Third, a paper-based cantilever beam has to be designed such that will overcome some issues of the current micro- and mili-cantilever sensors for characterization of liquids such as low disposability, complex hardware, and high costs.

Thus the particular objectives of these research are:

- To develop a general model based on Richards' equation to predict liquid imbibition in complex networks.
- To develop a general model the hygro-mechanical bending response of paper-based structures that will overcome the drawbacks of the previous models presented in the open literature.
- To design and fabricate a PB-HMS with an easy activation method and simple hardware.
- To derive a method for characterization of fluids using paper-based cantilever beams.

The accomplishment of these particular objectives as well as the conclusions of the preset research are described in six chapters organized and summarized as follows:

#### 1.4.1 Chapter 1

This chapter provides an introductory overview of the evolution of paper-based devices from silicon-based microsystems to the current state of paper-based systems. Then, the rationale of this research is described based on the current state-of-art related to paper-based systems. The main contribution of this research is to develop a paper-based sensor based on hygro-mechanical detection for characterization of bio-fluids. Four main

areas of knowledge involved in this research are identified: cantilever biosensors, hygro-mechanical systems, paper-based microfluidic and imbibition of porous media. A literature review regarding these areas is presented in order to define the particular objectives of the research. Finally, this thesis is divided into six chapters, whose contents are outlined in the following sections.

#### 1.4.2 Chapter 2

One of the main gaps in the knowledge related to paper-based systems is a lack of understanding in capillary imbibition in two-dimensional domains. This represents a limitation to developing improved design of these devices. In this chapter, the two-dimensional imbibition into paper-based networks using Richards' equation is studied. Evaluation of advancing wetting front of different geometries is investigated using the proposed model. The solution of the derived nonlinear partial differential equation is carried out numerically. The numerical results are experimentally validated using chromatography paper. Measurements of the imbibition were carried out by image processing. The proposed model represents an excellent tool for developing new design rules to control the delivery time of reagents in paper-based microfluidic devices.

### 1.4.3 Chapter 3

In this chapter, a description of the hygro-mechanical motion induced by hygromorphism as well as the phenomena involved in the problem are described. Then, the constitutive equations of the problem are discussed to develop a one-dimensional stress-imbibition model. In such a model three nonlinearity sources are considered. A dimensionless formulation is developed to provide a means to identify the major influences that have a considerable effect on the typical hygro-mechanical bending response of paper-based beams. The analytical solution of the linear problem, which is based on LW theory, is presented with the aim to provide a reference for understanding the hygro-mechanical bending response. It is suggested that the analysis of the bending response not only including the curvature but also the whole bending strain state. The proposed model can be applied to describe the bending strain state of the paper-based beams under different influences.

### 1.4.4 Chapter 4

Previous formulations [58, 59] account only for one nonlinearity source related to the softening effect due to an increment on the moisture content in the paper. In this chapter, the nonlinear influences on the hygro-mechanical bending response of paper-based beams are studied. In order to analyze such influences, the material nonlinearities are described by means of three functions that are dependent on three dimensionless

parameters as described in chapter 3. The influences on both bending state and total strain distribution are studied to provide a better understanding of the phenomenon. The analytical solution of the linear problem is presented with the aim to provide a reference for comparing the aforesaid nonlinear effects. Finally, the proposed formulation is applied to describe the bending response of the experimental results presented in [58].

#### 1.4.5 Chapter 5

The hygro-mechanical response of paper has been studied only as a physical phenomenon. Thus, the main concern in this chapter is to take advantage of the hygro-mechanical response of paper to develop paper-based sensors for physical characterization of aqueous solutions. The feasibility to characterize these solutions by means of the dynamic bending response of paper is studied in this chapter. A new sensing principle using a paper-based cantilever sensors is proposed. It is suggested that the characteristic hygro-mechanical bending response of paper-based beams may provide crucial information about the tested liquid. A cantilever-droplet design is proposed as the sensing element. The hygro-mechanical bending response of different aqueous solutions containing methanol, hydrogen peroxide, glycerol, and sucrose are tested experimentally. The experimental results show the feasibility of the proposed sensing element by comparing their phase portrait (bending velocity against acceleration). It is expected that the final application of these hygro-mechanical sensors

may lead to the characterization of bio-fluids, the identification of hazardous liquids and the estimation of concentrations in aqueous solutions.

#### 1.4.6 Chapter 6

In the previous chapter it was found that certain liquids yield an atypical hygro-mechanical bending response by analyzing their phase portrait. However, such an analysis does not provide a means to quantify the performance of the hygro-mechanical response. In this chapter a method to quantify the performance of the hygro-mechanical response in order to characterize liquid is proposed. The bending response is approximated using a transfer function model that determine an equivalent system. Such an equivalent system is defined as “hygro-mechanical system’, and it can be applied to characterize the tested liquid. The hygro-mechanical system exhibit a similar response to their counterpart micro-electro-mechanical systems: however, they have a very low frequency response. The results show the feasibility to characterize binary aqueous solutions using the proposed method. In addition, the analysis of the hygro-mechanical systems allows the identification of liquids. The proposed method promises a good alternative to performing characterization and/or identification of liquids at a very low cost compared to other commercial equipment such as refractometers and near infrared spectrometers.

#### 1.4.7 Chapter 7

This chapter presents the conclusion of this research as well as the suggested future work. The general conclusions of this thesis are stated in the first section of this chapter. The second section summarized the particular contributions of the conducted research and presented the suggested future work.

## Chapter 2 Two-dimensional imbibition into paper-based networks

*One of the main gaps in the knowledge related to paper-based systems is a lack of understanding in capillary imbibition in two-dimensional domains. This represents a limitation to developing improved design of these devices. In this chapter, the two-dimensional imbibition into paper-based networks using Richards' equation is studied. Evaluation of advancing wetting front of different geometries is investigated using the proposed model. The solution of the derived nonlinear partial differential equation is carried out numerically. The numerical results are experimentally validated using chromatography paper. Measurements of the imbibition were carried out by image processing. The proposed model represents an excellent tool for developing new design rules to control the delivery time of reagents in paper-based microfluidic devices.*

## 2.1 Imbibition

Capillary imbibition is perhaps one of the most interesting physical phenomenon. Several products that use capillary imbibition as a working principle are present in our daily life. Among them are diapers, wipes, coffee filters and inkjet printers. In microfluidics, this phenomenon has been applied to develop self-driving flows on paper-based devices. Here, analytical assays can be performed without the need for external pumps. Only a few designs methodologies have been proposed to potentiate the performance of such devices. One of the reasons for this drawback is the lack of understanding regarding the capillary imbibition into two-dimensional networks. Thus, it expected the providing a model that predicts the capillary imbibition into two-dimensional designs may contribute to the development of new improved designs.

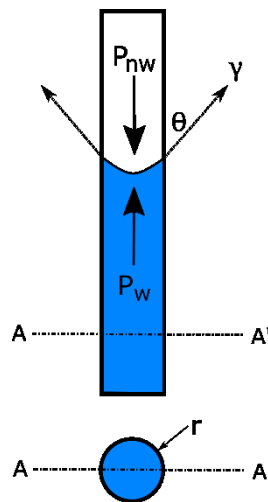


Figure 2.1 Schematic representation of capillary imbibition into a cylindrical pore.

Imbibition, also known as capillary rise or wicking, is defined as the suction of a liquid into a porous media due to the negative capillary pressure generated at the liquid–air interfaces [105]. The wetting of the solid surfaces by the invading liquid produces a gradient in the surface energy of the solid phase generating the so-called capillary pressure. The simplest example of this phenomenon is found in glass capillaries as that depicted in Fig. 2.1. According to [105], the capillary pressure at the interface of both fluids is the difference in the non-wetting pressure ( $P_{nw}$ ) and the wetting pressure ( $P_w$ ), expressed as:

$$P_c = P_{nw} - P_w \quad (2.1)$$

At the molecular level, the attraction of molecules in the liquid medium and the adhesion of such molecules to those in the solid medium generates capillary forces at the solid-liquid interface, also known as surface tension ( $\gamma$ ). Hence, the force balance of this components leads to the well-known Young–Laplace equation for capillary pressure in a capillary.

$$P_c = \frac{2\gamma\cos\theta}{r} \quad (2.2)$$

where  $\theta$  represents the contact angle at the solid-liquid interface known as meniscus.

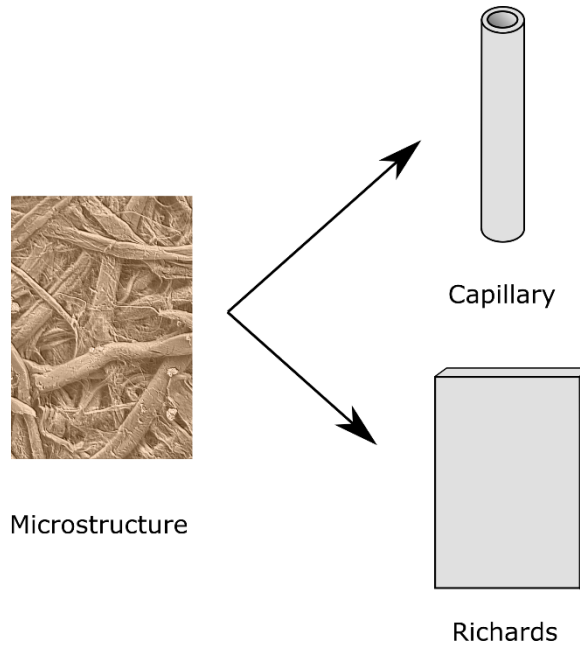


Figure 2.2 Representation of macro-models for imbibition into porous media: capillary based and Richard’s models.

In general, imbibition can be described as a complex phenomenon due to the random distribution of the porous media. The imbibition in hygroscopic materials like paper is a result of the combination of both means of transport, through the voids and within the fibers. Thus, modeling this phenomenon at the microstructure level represents a challenging task. In this regard, macro-models, which transform these porous networks into a simple homogenous media, have been applied in different fields such as textile and paper industry to predict capillary imbibition. Fig. 2.2 presents the schematic representation of two macro-models, capillary based and Richards’. In capillary based models the porous media is represented as a capillary tube with an equivalent radius  $r$ . In contrast, Richards’ models represent the equivalent media as the

same geometry as the problem to be analyzed. Both models will be studied in the following sections.

## 2.2 Capillary Model

Lucas [88] and Washburn [87] presented an analytical solution for the capillary rise in a circular tube neglecting the hydrostatic pressure and the inertia term, known as Lucas-Washburn theory (LW). Almost one hundred years after Lucas and Washburn presented their solution, Zhmud et al. [106] presented a long time asymptotic analytical solution for the problem including hydrostatic pressure but neglecting the inertial term. Hamraoui and Nylander [107] provide an analytical approach that compensates the error on the asymptotic solution in [4] by introducing a retardation coefficient. Fries and Dreyer [108] present an analytical solution based on the Lambert function; however, the inertia term was also neglected in their solution.

In some cases, it has been shown that the inertial term cannot be neglected under specific conditions. Masoodi et al. [109] and Nia and Jessen [110] provided a general formulation for the capillary rise ( $h_c$ ) in a single circular tube. The governing equation is presented in Eq. (2.3). The driving forces, in this case, can be classified as (I) capillary pressure, (II) viscous pressure loss, (III) hydrostatic pressure and (IV) inertia term. Although, the imbibition in a single capillary tube may seem simple, its governing equation involve highly nonlinear terms [109, 110].

$$\underbrace{\frac{2\gamma\cos\theta}{r}}_I = \underbrace{\frac{8\mu}{r^2}h_c\dot{h}_c}_{II} + \underbrace{\frac{\rho gh_c}{III}} + \underbrace{\rho \frac{d}{dt}(h_c\dot{h}_c)}_{IV} \quad (2.3)$$

From this formulation, simple reductions can be made by neglecting driving forces according to the application to be studied. For instance, in paper-based microfluidics devices the hydrostatic pressure and the inertia term in Eq. 2.3 can be neglected; then, LW equation and its solution can be obtained as Eq. 2.4 and Eq. 2.5, respectively. This solution of this equation has been extensively applied to model lateral imbibition in paper-based microfluidic devices [110].

$$\frac{2\gamma\cos\theta}{r} = \frac{8\mu}{r^2}h_c\dot{h}_c \quad (2.4)$$

$$h_c(t) = \sqrt{\frac{\gamma r \cos\theta}{2\mu} t} \quad (2.5)$$

Capillary models provide a simple way to develop analytical expressions for the imbibition into porous media under different scenarios. Several analytical solutions have been presented in the literature considering capillary tubes of same circular cross section area [106-108, 110, 111]. Other variants of these simple models have been proposed. For instance, Reyssat et al. [112] developed an analytical model for imbibition on a bilayer of packed beads with different permeabilities. The authors extended their work to study imbibition into a material with a permeability gradient as a function of the length domain. Cai et al. [113, 114] developed an

analytical model assuming tortuous capillaries with different cross section shapes rather than the conventional circular ones. In another example, Masoodi et al. [115] performed numerical simulations of imbibition in paper-like porous media considering the swelling of the media.

Some authors have studied other effects such as roughness of the capillary wall [116, 117], boundary conditions [118] and contact angle [119, 120]. From a design point of view capillary models represent a simple and accurate tool to model one dimensional problems in paper-based microfluidic systems. In these applications the evaluation of the wet front is the main concern. However, the limitations of this model to predict the capillary imbibition into two-dimensional paper-based networks have not been well established.

In this regard, different attempts to describe the transport on two-dimensional porous media have been conducted in past years using capillary models. The geometries analyzed in the literature are presented in Fig 2.3. Medina et al. [121] develop a model for triangular imbibition into paper. Reyssat et al. [122] studied the imbibition in geometries with axial shapes, namely conical as well as parabolic and power-law-shaped channels. In another work, Mendez et al. [123] developed a frame work to model the imbibition in porous membranes of alternative geometries, see Fig. 2.3c. The authors reduced the problem to analyze a simple geometry form by discretization the geometry into a rectangle and a circular section.

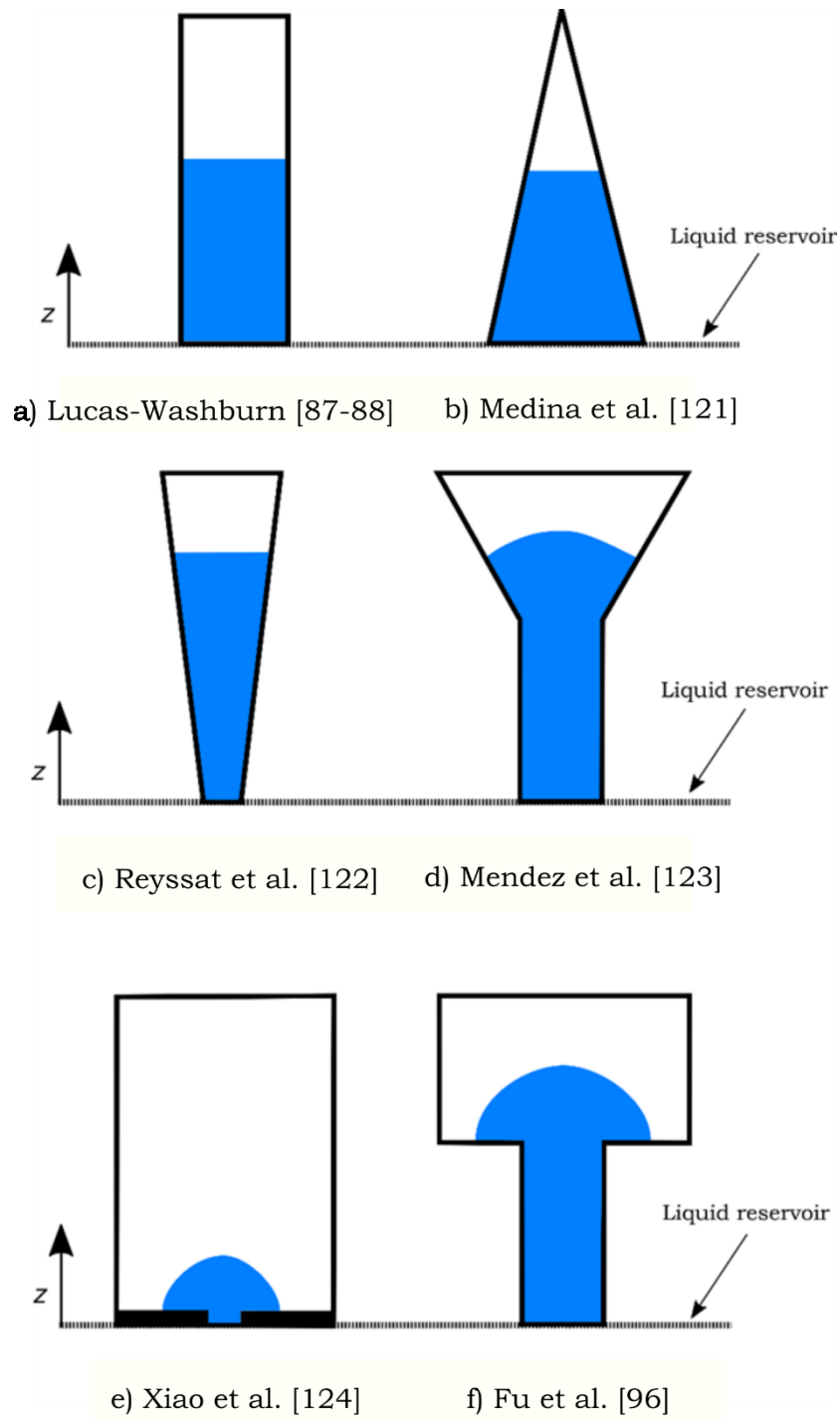


Figure 2.3 Imbibition into 2D porous networks. Different geometries analyzed in the literature. The liquid penetration into the network is represented in blue.

In addition, Xiao et al. [124] analyzed a radial flow of Fig. 2.3d by means of a source like solution. Finally, Fu et al. [96] studied the transport on rectangular channels with a sudden width expansion. The authors calculated the imbibition by discretizing the domain into rectangular subdomains. All of the previous capillary models provide good agreement with the experimental for the geometries summarized in Fig 2.3. However, the limitations of capillary models for the case of complex geometries, i.e. nonsymmetrical design and perforations, were not discussed by the authors. Moreover, the authors limited the analysis to simplified geometries, which can be easily reduced into lateral problems. From a design point of view, this represents a major drawback to developed new designs that may enhance the performance of these devices.

## 2.3 Richards' based model

Soil-based models based on Richards' equation have been extensively studied for unsaturated and saturated flows in both swelling [125, 126] and no-swelling [127, 128] soils. Several analytical solutions have been developed for semi-infinite domains under different boundary conditions in one dimension space [129-131]. However, these models lead to a highly nonlinear partial differential equations which are difficult to solve analytically. In this light, several numerical solutions have been developed to solve this type of equations. Among the most relevant are the finite difference and finite element methods [132-134].

A two-dimension model that can predict the two-dimensional capillary imbibition is needed for the analysis and/or design of paper-based networks. Richard's model [104] for porous media is applied to develop a general framework to describe the flow in two dimension paper-based networks. The capabilities of Richard's equation to model two-dimensional imbibition have not received particular attention as in soil mechanics the media is usually represented as a simplified geometry (i.e. rectangles). Richard's equation for two-dimensional imbibition is represented in Eq. 2.6. For detail on the development of Richard's equation please refer to Appendix B.

$$\frac{\partial \varphi}{\partial t} = \frac{\partial}{\partial x} \left( D(\varphi) \frac{\partial \varphi}{\partial x} \right) + \frac{\partial}{\partial y} \left( D(\varphi) \frac{\partial \varphi}{\partial y} \right) + \frac{\partial K(\varphi)}{\partial y} \quad (2.6)$$

A good approximation of both diffusivity  $D(\varphi)$  and conductivity  $K(\varphi)$  functions can be made by applying the Brooks-Corey model that is well known for modeling water penetration in soils [135]. Under this assumption, the diffusivity and the conductivity functions are defined in this model as

$$D(\varphi) = D_0 \varphi^n \quad (2.7)$$

$$K(\varphi) = K_0 \varphi^{n_k} \quad (2.8)$$

Considering that the hydrostatic pressure dominates the effect of the derivative of the conductivity on the vertical coordinate, its contribution to

Eq. 2.6 is small enough that can be neglected. The similar assumption has been made in capillary models, where the gravitational effects are neglected [2-6]. Thus, Eq. (2.6) can be simplified as:

$$\frac{\partial \varphi}{\partial t} = \frac{\partial}{\partial x} \left( D(\varphi) \frac{\partial \varphi}{\partial x} \right) + \frac{\partial}{\partial y} \left( D(\varphi) \frac{\partial \varphi}{\partial y} \right) \quad (2.9)$$

## 2.4 Methods and materials

The paper-based networks studied in this chapter were fabricated using chromatography paper (Whatman® grade 3MM). The geometries of the analyzed configurations were designed and cut out using a conventional electronic paper cutter (Silhouette Curio®). Observations of the capillary imbibition were performed using distilled water. All the experiments were conducted at a room temperature of 24°C with a relative humidity of 50%. The physical properties of water are summarized in Table 1. Capillary imbibition was recorded using a digital microscope (Celestron®). Then, image processing of the frames was done to enhance the display and to measure the wetting front. Finally, numerical solutions of Eq. (2.15) were carried out using the fine element partial differential equation (PDE) solver of COMSOL Multiphysics®.

The developed Richards' based model requires three parameters to solve any imbibition problem. The volumetric content at saturation ( $\varphi_s$ ) has to be estimated first. Water content at saturation of the paper sample was experimentally determined as 0.84 by estimating the volume of water using

a weight scale and its density. In contrast, the diffusivity and the exponent  $n$  are more complex to assess. According to soils theory, the diffusivity of the porous media depends on the liquid properties and the exponent  $n$  depends on the type of soil. Therefore, it is expected that these parameters can be determined using capillary imbibition measurements.

Table 2.1 Physical properties of water [136]

Property	Value
Density $\rho$	997.0 [Kg/m <sup>3</sup> ]
Viscosity $\mu$	0.890 x 10 <sup>-3</sup> [Kg/m·s]
Surface tension $\gamma$	0.0720 [N/m]

In order to test the developed Richards' based model, a set of networks with different geometries are analyzed. This group is divided into two main groups: conventional and complex geometries. The first group includes simple symmetrical configurations, whereas the second set considers designs whose geometries incorporate asymmetrical shapes and perforations. The study of these configurations is presented in the following sections.

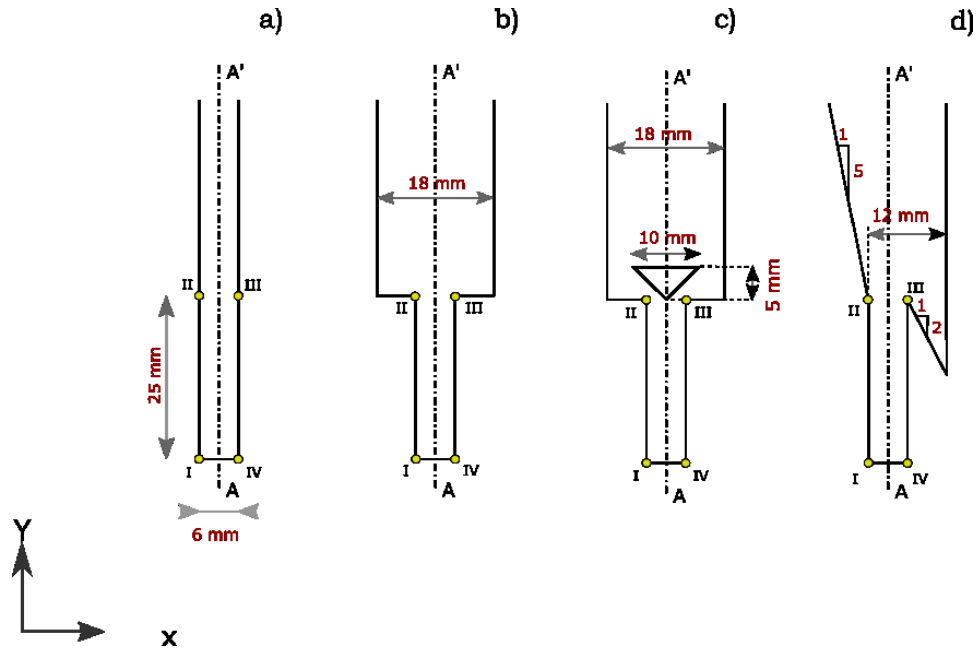


Figure 2.4 Schematic representation of conventional two-dimensional paper-based networks a) case I, b) case II, c) case III, and d) case IV.

## 2.5 Imbibition into two dimensional geometries

The schematic representation of the networks investigated in this section is provided in Fig. 2.4. As previously stated a rectangular configuration, which is defined as case I, is the simplest two-dimensional configuration (Fig. 2.4a). One of the main advantages of these types of geometry is that can be modeled using LW theory with a good accuracy. Here, the edge form by nodes I and IV is exposed to a water reservoir; such a condition is represented as a Dirichlet boundary condition ( $\varphi = \varphi_s$ ). The remaining edges are in contact with air and it can be assumed that there is not flow through them. Thus these edges can be assumed as a non-flux

Neumann boundary condition. Fig. 2.3b shows case II, whose geometry is formed by a sudden expansion of the width at node II and III from 6 mm to 18 mm. This case has been studied in [96]. The boundary conditions of this case are similar to case I

The equivalent diffusivity ( $D_0$ ) and the exponent  $n$  can be determined experimentally using the configurations presented in Fig. 2.3. Different values of  $D_0$  were estimated for a given value of  $n$  using experimental measurements of the imbibition along the center line AA'. These values of  $D_0$  were determined by minimizing the root mean square error (RMSE) of the experimental measurements compared to the numerical solution of Eq. (2.15). Table 2.2 shows the respective RMSE for the capillary imbibition in cases I, II, and III using different values of  $n$ . It can be seen that the capillary imbibition along the line AA' can be modeled using different values of  $n$  with a reasonable RMSE.

Table 2.2 RMSE and maximum relative errors of imbibition along the center line for various values of  $n$ .

n	Case I		Case II	
	RMS	maximum	RMS	maximum
2	4.0%	8.9%	6.7%	14.4%
4	3.7%	9.1%	4.5%	10.4%
6	3.8%	9.0%	3.6%	8.5%
8	3.7%	9.1%	3.5%	7.9%

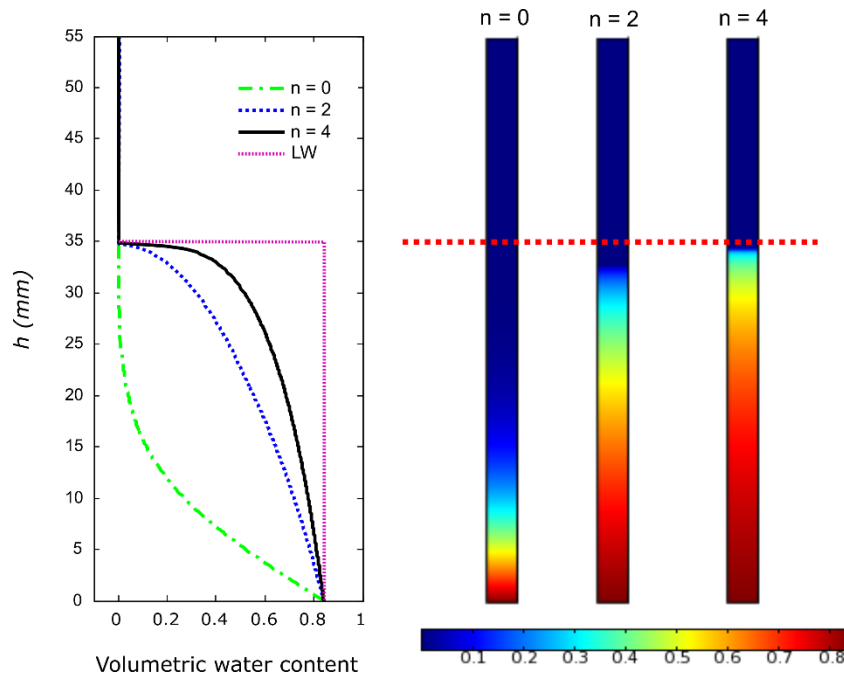


Figure 2.5 Numerical results of the volumetric water content distribution for different values of  $n$  of the case I a) along AA' and b) two-dimensional domain.

Although Table 2.2 suggested that using different values of  $n$  yields to a good agreement with the experimental results, it is interesting to look at the effect of the exponent  $n$ . Fig. 2.5 shows the volumetric water content gradient of the case I, whose advancing wetting front is  $h_c = 34\text{mm}$ , using different values of  $n$ . It can be seen that the water content tends to become homogenous as  $n$  increases. This result suggests that when increasing  $n$ , the liquid content profile will tend to the binary state (wet/dry) assumption of the LW theory. It is also interesting to note that the solution of  $n=0$  yields to the same water content distribution solution using molecular diffusion theory (Fick's law). Thus, Richards' based model allows the estimation of both the liquid volumetric distribution and the advancing

wetting front in the paper sample. In this chapter only the advancing wetting front will be analyzed as the volumetric liquid content is not of interest in paper-based microfluidic devices. However, the volumetric distribution within the paper sample will be studied in the next chapter to describe the hygro-mechanical response of paper.

In contrast, when looking at the two dimensional imbibition of the case II the influence of  $n$  becomes significant. Here, low values of  $n$  yield high errors on the advancing wet front prediction when accounting for the sudden width expansion of this network. The value of  $n$  used in this work was determined as 6 for two reasons. First, similar errors as the case I can be achieved using this value of  $n$ . Second, it was found that the reduction of the RMS is only 0.1% when increasing  $n$  from 6 to 8 is low. Third, the solution of the nonlinear PDE using higher values of requires more computational effort.

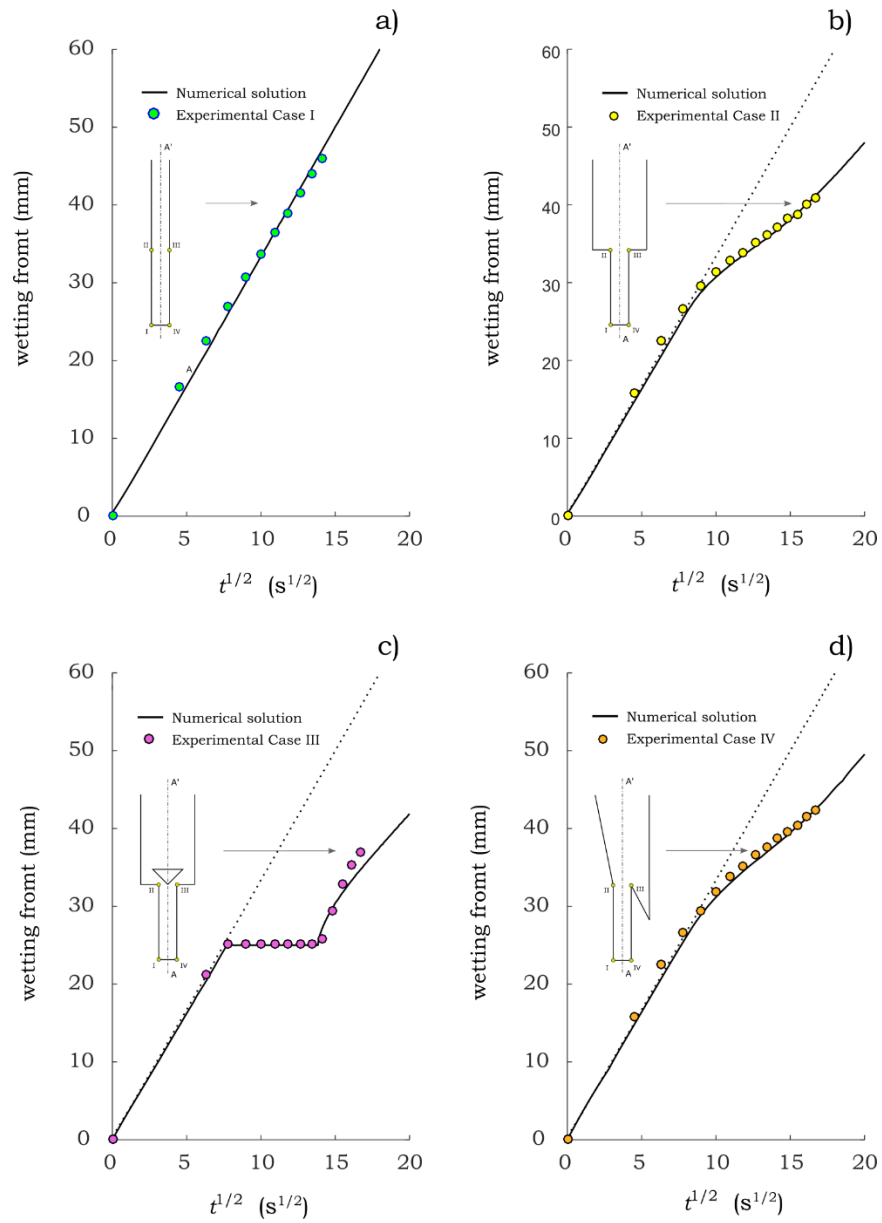


Figure 2.6 Advancing wetting front due to imbibition of a) case I, b) case II, c) case III, and d) case IV. Comparison between numerical solution (using  $n=6$ ) and experimental measurements. Dotted lines in b), c) and d) are the solution to the case I.

It can be seen in Fig. 2.6 that the experimental measurements of the wetting front for case I are in good agreement with the numerical solution of the Richards' model along line AA'. In addition, it should be mentioned that the numerical solution of Eq. 10 yields to the same solution found using the LW theory. These types of similarities between capillaries and soil based models have been reported elsewhere [137-139]. Thus, these results suggest that Richard's equation can be suitable for modeling imbibition into paper-based devices. Furthermore, the results of the Case I presented in Fig. 2.6 verify that the hydrostatic pressure does not play a significant role on the capillary imbibition, and it can be neglected.

As previously found by Fu et al. [96] the geometry of case II exhibit a slower capillary flow compared to Case I. The numerical prediction is in agreement with the experimental results as shown in Fig. 2.6b. The results show that the first rectangular section ( $h_c < 25\text{mm}$ ) obey the LW theory. Hence, a reduction of the capillary imbibition velocity due to the width expansion is presented as illustrated in Fig. 2.6b. In addition, the experimental measurements of the advancing wetting front of the Case II follow the same trend as the numerical predictions, see Fig. 2.6c. However, there is a discrepancy after the wet front passes the cutout. This discrepancy may be due to several influences such as the inner corner effects of the cutouts. Finally, the numerical solution of the case IV also exhibits a good agreement with the experimental measurement of the advancing wet front as can be seen in Figure 3d. In all the cases presented

in Fig. 2.6 the RMS and maximum relative errors do not exceed 4% and 9%, respectively.

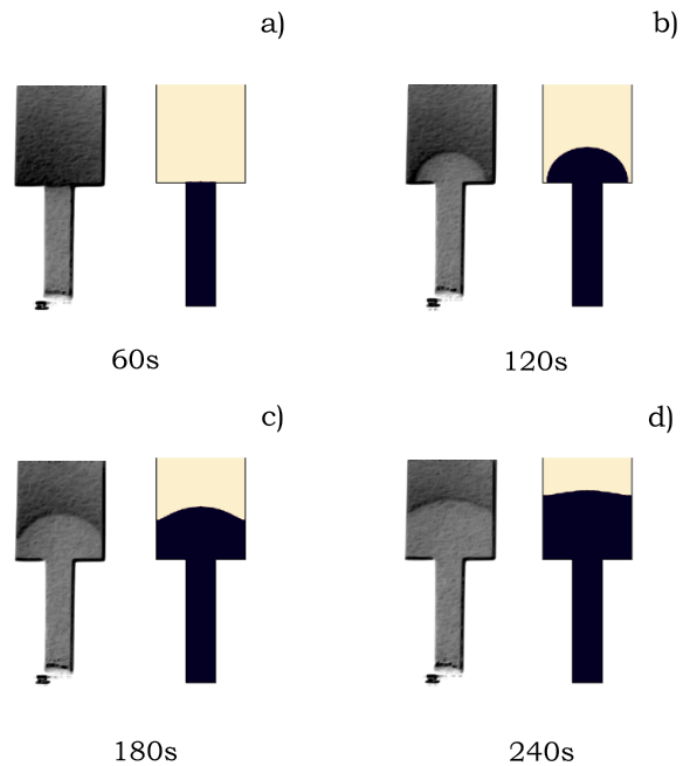


Figure 2.7 Time lapse of the capillary imbibition of the case II. Gray scale images are pictures of the experimental results, and blue images represent numerical solutions.

Let's now look at the imbibition into the whole two-dimensional domain of the cases presented in Fig. 2.3. Figs. 2.7-2.9 present the time lapse comparison between the numerical solution of the two-dimensional imbibition and the experimental results of case II, III and IV. It is interesting to note that the results predicted by the model are very close to the experimental results, which represents one of the main contribution of

the proposed model. As it was expected, the wet front at the macro-level in the rectangular segment ( $h_c < 25\text{mm}$ ) is a straight line as the width of the channel is constant from the wetting edge to the width expansion. It should be emphasized that at the micro-level the advancing wet front is a meniscus rather than a straight line. Here, the flow velocity component along axis  $x$  is constant, while the  $y$  component decreases as the wet front advances along the length of the channel. In order to tune the flow velocity, both components can be modified by adjusting the geometry.

The time lapse of capillary imbibition for case II is presented in Fig. 2.7. The numerical predictions of the capillary imbibition in the two-dimensional domain are in good agreement with the experimental measurements. Numerical results of case II show a different behavior compared to the design I in concordance with the experimental observation by Fu et al. [96]. Here, both  $x$  and  $y$  components of the velocity are modified due to the sudden expansion of the width. The proposed model can be applied to estimate the wetting profile not only along the line A-A' (shown in Fig. 2.4) but also in the whole two-dimensional domain compared to the equivalent resistance model developed by Fu et al. [96]. This capability represents an interesting feature that enables to enhance the design of paper-based microfluidic devices.

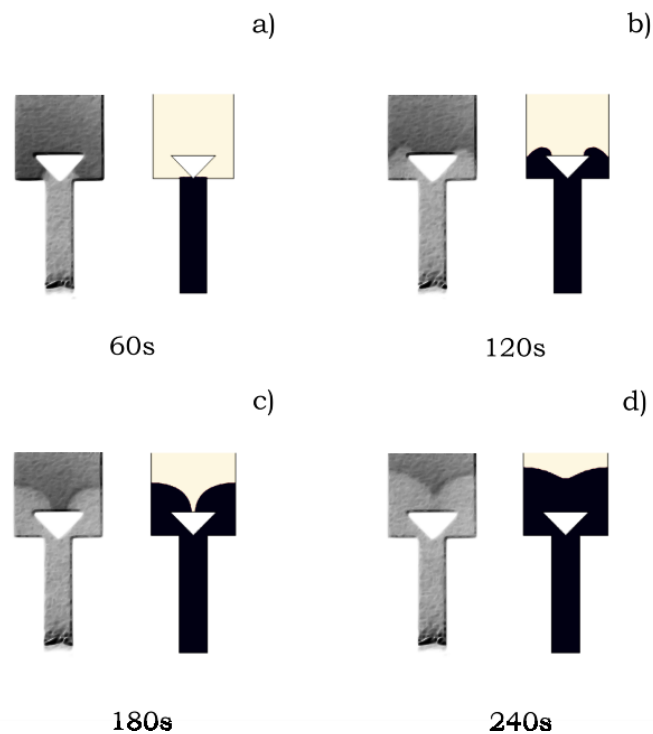


Figure 2.8 Time lapse of the capillary imbibition of case IV. Grayscale images are pictures of the experimental results, and blue images represent numerical solutions.

The numerical and experimental results of the case III are presented in Fig. 2.8. In this case, the triangular perforation induces a particular imbibition profile due to both width expansion and perforation. First, the triangular imbibition induces a radial flow ( $\sim 120s$ ) yielding to an inverted sharp wetting profile ( $\sim 180s$ ). This particular response of the wetting profile is experimentally validated as illustrated in Fig. 2.8. The incorporation of perforations into the paper-based network could be an excellent alternative for developing new designs rules. For instance, rules to control the reagent transport for applications such as mixers or chromatography assays.

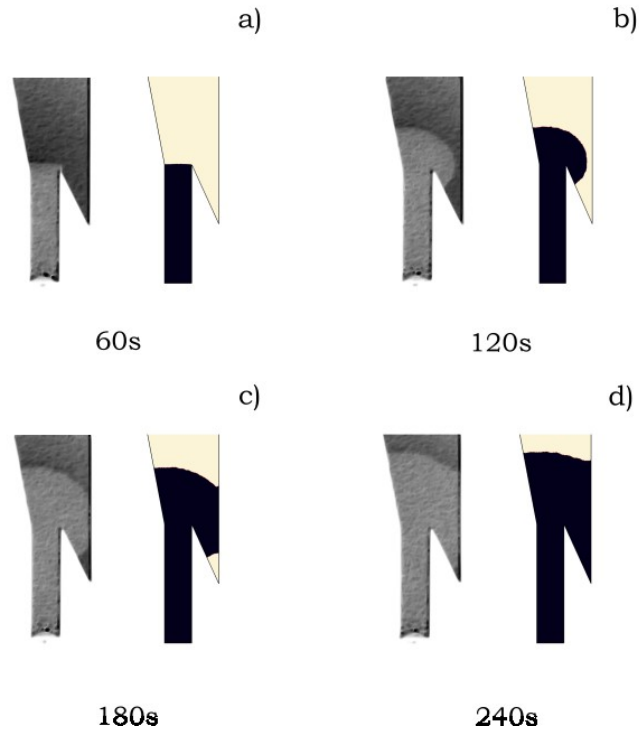


Figure 2.9 Time lapse of the capillary imbibition of the case II. Gray scale images are experimental results, and blue images represent numerical solutions.

Finally, the time lapse imbibition of case IV is presented in Fig. 2.9. Like previous cases, the numerical solution is in good agreement with the experimental measurements. Hence, it is suggested that the proposed model can also be applied to model imbibition in asymmetrical domains. In this case the asymmetrical expansion of the width induces an elliptical wetting front after the width expansion (Figs. 2.9b and 2.9c) compared to the circular wet front in symmetrical shapes in case II. In addition, it can be seen In Fig. 2.9c that the downward imbibition on the right side induces an asymmetrical wet front.

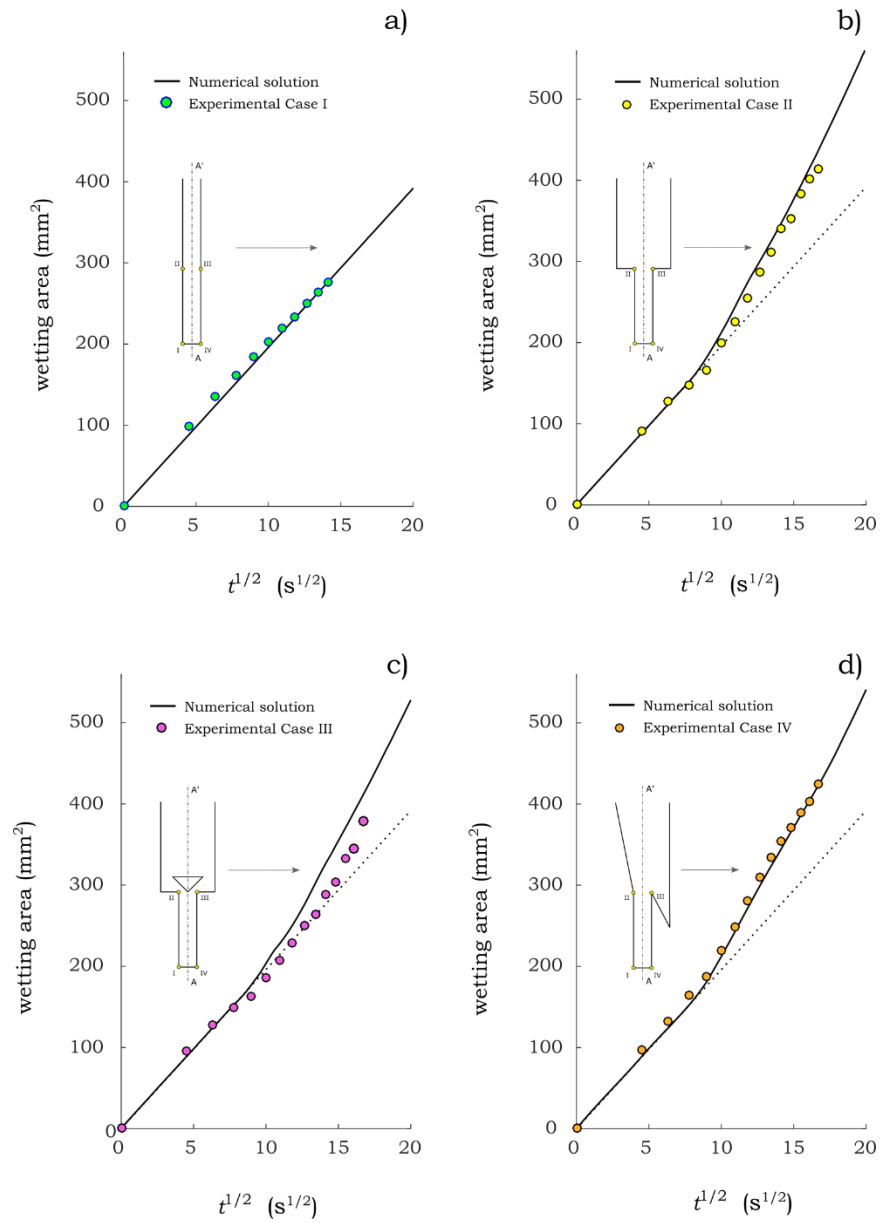


Figure 2.10 Advancing wet area due to imbibition of a) case I, b) case II, c) case III, and d) case IV. Comparison between numerical solution (using  $n=6$ ) and experimental measurements. Dotted lines in b), c) and d) are the solution to the case I.

In order to further evaluate the accuracy of the proposed model the wetting area during imbibition of all the cases is estimated. The wetting area as a function of the root square of time of cases I-IV is presented in Fig. 2.10. The experimental measurements of the wetting area are in good agreement with respect to the numerical predictions for the cases I, II and IV. The RMS and maximum relative errors for these cases do not exceed 5.4% and 8.9%, respectively. However, for the case III these errors are higher as can be seen in Figure 2.10c. The RMS and maximum relative error of this case are 9.3% and 13.5%, respectively.

## 2.6 Summary

Richard's equation can be applied to model the capillary imbibition in two-dimensional paper-based networks. This model requires only three parameters, which can be easily determined experimentally. The characterization of  $Do$  and  $n$  can be conducted by using simple geometries such as rectangular channels. Compared to capillary based models Richard's equation is capable to predict the capillary imbibition in networks that includes complex geometries. It is expected that this approach can be applied to developed new design rules for controlling the flow in paper-based microfluidics devices. Richard's based model represents an excellent alternative tool to model the hygro-mechanical response of paper as its solution enables the estimation of the water content distribution along the thickness of the paper sample.

Although only five configurations were studied in this chapter, Richard's based model can be applied to perform analyses of different geometries that may be of interest in paper-based systems. For instance combination of asymmetrical shapes with perforations. Moreover, topological optimization can be carried out using the proposed model. Perhaps one of the main drawbacks of the proposed model is that it requires numerical solution. However, nowadays computational tools allow the solution of this types of problems within few seconds.

It should be noted that the paper-based designs analyzed in this chapter were cut out. However, two-dimensional paper-based devices fabricated by others methods (i.e. waxing and photolithography) can also be studied using the proposed model. Finally, the errors found in previous cases may be reduced by taking into consideration other effects such as anisotropic imbibition and swelling of fibers.

## Chapter 3    Hygro-mechanical bending response of paper

*In this chapter, a description of the hygro-mechanical motion induced by hygromorphism as well as the phenomena involved in the problem are discussed. Then, the constitutive equations of the problem are introduced to develop a one-dimensional stress-imbibition model. In the model three nonlinearity sources are considered. A dimensionless formulation is developed to provide the means to identify the major influences that have a considerable effect on the typical hygro-mechanical bending response of paper-based beams. The analytical solution of the linear problem, which is based on LW theory, is presented with the scope to providing a reference for understanding the hygro-mechanical bending response. It is suggested that the analysis of the bending response not only requires the curvature but the whole bending strain state. The proposed model can be applied to describe the bending strain state of the paper-based beams under different influences.*

### 3.1 Hygro-mechanical response of paper-based beams

In order to describe the hygro-mechanical bending of paper-based beams it is necessary to provide the following definitions:

- “*Hygroscopy is the ability of a substance to attract and hold water molecules from the surrounding environment [140]*”. Hence, a material manifesting hygroscopy is commonly known as hygroscopic material.
- “*Hygromorphism is the ability of an object to change shape in response to humidity or moisture [141]*”.

Plants are the most common example of natural hygroscopic materials exhibiting hygromorphism. They take advantage of this property to generate motion of their branches, stems or leaves for different purposes such as self-protection and seed spreading. As used from now on, the term “hygro-mechanical response” refers to these motion induced by hygromorphism, which can be classified as bending, twisting and cooling. In this work, only the hygro-mechanical bending response will be studied.

#### 3.1.1 Hygro-mechanical bending response

The hygro-mechanical bending response of paper, a hygroscopic material, has received particular attention over the past years. Several

works have been conducted to describe the position or curvature responses with respect to the time of hygro-mechanical bilayer beams. However, less attention has been pointed out to single layer paper-based beams. Douezan et al. [58] and Reyssat and Mahadevan [59] introduced the study of the hygro-mechanical bending response of a single layer paper beam. They also provided an explanation of the occurring phenomena during the bending response.

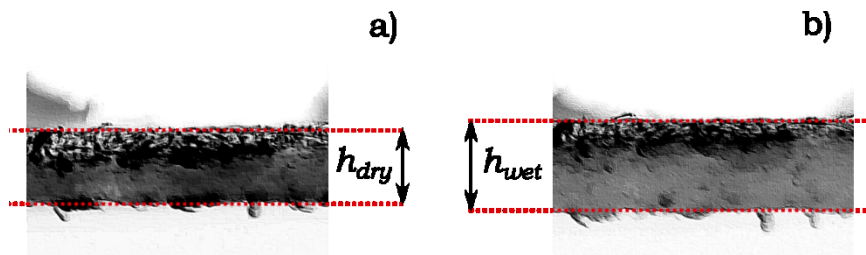


Figure 3.1 Microscope cross section image of a piece of chromatography paper experiencing hygroexpansive strain along its thickness. Comparison of a) dry paper and b) wet paper.

Imbibition into a strip of paper yields to a modification of its initial volumetric moisture content. This transient redistribution of the moisture induces two inherent phenomena, which play fundamental roles in the characteristic bending response. First, the fibers of paper swell as their moisture content increases [142, 143], namely hygroexpansive strain. It has been suggested that swelling takes place as the water molecules break and replace interchain bonds in cellulose [144]. As an example Fig. 3.1 shows the hygroexpansive strain of dry and wet chromatography paper. In this case, the hygroexpansive strain of 0.17 is measured along the

thickness of the paper. Second, an apparent reduction in the Young modulus of paper occurs as the moisture content in the fibers rises [60]. This effect is due to the interaction of cellulose chains and water, which acts as a plasticizer that reduces the Young's modulus [145]. Thus, the bending elasticity of paper decreases as the water content raises along the thickness of the paper. Fig. 3.2 shows the softening effect on a piece of tracing paper, where a piece of wet paper collapse due to its own weight (Fig. 3.2b). In contrast, the dry paper remains unaffected as its weight does not have a huge influence on it (Fig. 3.2a). Therefore, the specific combination of these phenomena determines the characteristic bending response of any hygro-mechanical motion. It is important to remark that both swelling and softening effects are only presented if and only if water penetration into the paper structure occurs.

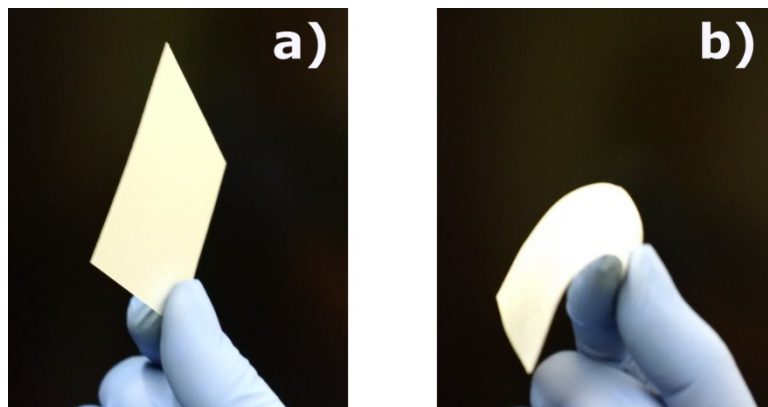


Figure 3.2 Softening effect on a) dry and b) wet pieces of tracing paper

In addition, other phenomena may also influence the hygro-mechanical response of paper elasto-capillary. The elasto-capillary effect is expected to be small as the elasto-capillary length is one order of magnitude higher than the wetting length formed [146]. Moreover, in the hygro-mechanical bending response of paper elasto-capillary acts as a small restoring force rather than a generating force as in the case of other phenomena [146]. Thus, it is suggested that the principal influences on the hygro-mechanical bending response are the swelling of fibers and imbibition. These two phenomena are necessary to trigger the hygro-mechanical bending response. In contrast, other effects such as elasto-capillary and softening effect due to plasticization only have an influence on the apparent elasticity of the problem. According to the scale of the problem, it is suggested that the softening effect would dominate the elasticity of the problem.

### 3.1.2 Hygro-mechanical bending state

The schematic representation of the hygro-mechanical bending state is presented in Fig. 3.3. Let us consider a paper-based beam of initial length  $l$  with an initial homogenous moisture distribution along the thickness (axis  $z$ ), see Fig. 3.3a. When exposing one side of the beam ( $z=0$ ) to water the volumetric moisture content increases uniformly along  $z$ . Thus, a gradient extension of  $l$  like that depicted in Fig. 3.3b is formed from a high expansion at the bottom of the paper beam ( $z=0$ ) to a low swelling at the upper surface ( $z=h$ ). As a consequence, the beam will bend to compensate

the differential of hygroexpansive strain and to minimize the bending strain energy as seen in Fig. 3.3c. The hygroexpansive strain can be defined as the normal strain of  $l$  at a given position along  $z$  as:

$$\varepsilon_h(z) = \frac{\Delta l_h(z)}{l} \quad (3.1)$$

where  $\Delta l_h$  is the extension produced by the hygroscopic swelling of paper. Similarly, the bending strain can be expressed as:

$$\varepsilon_b(z) = \frac{\Delta l_b(z)}{l} \quad (3.2)$$

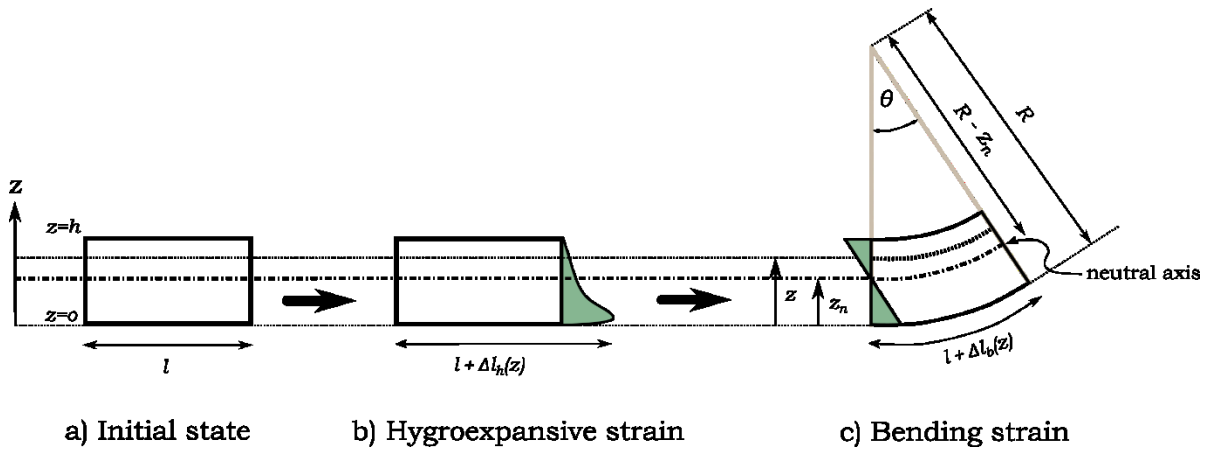


Figure 3.3 Schematic representation of the hygro-mechanical bending state.

### 3.2 Constitutive equations

The hygro-mechanical bending response can be divided into four physical phenomena occurring at the same time. Fig. 3.4 shows the block diagram of the multiphysics problem. The solution of the problem can be found as follows:

1. First, the moisture distribution  $\varphi$  is determined by means of the imbibition theory.
2. Then, the hygroexpansive strain  $\varepsilon_h$  and the relaxation of the Young modulus of elasticity  $E$ , which are function of the moisture content, can be evaluated.
3. Finally, the bending strain state is determined using the continuum mechanic of solids theory.

In the following subsections, the constitutive equations applied to describe imbibition and bending response are presented.

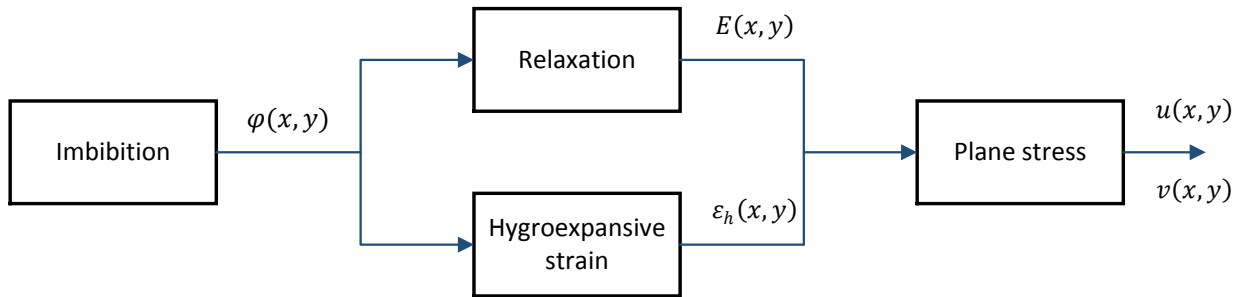


Figure 3.4 Block diagram of the imbibition-bending coupled problem.

### 3.2.1 Imbibition

Let us start by defining the model for the water transport into a paper-based beam. Authors in [58] claim that LW law for porous media can be applied to describe the water transport in tracing paper. It is well known that LW has been implemented to describe lateral transport in low-density

papers such as chromatography and filter papers [89] as previously described in chapter 2. However, a detail explanation of the transport theory is not discussed by the authors. For instance, LW theory yields to a discrete solution of the wet front as a function of the time. Such an assumption represents a significant drawback as both the hygroexpansive strain and Young modulus relaxation depend on the water content distribution across the thickness.

On the other hand, authors in [59] suggested that the molecular diffusion theory may be applied to describe the transport phenomena due to the fact that treated papers such as tracing paper have high density. They claim that capillary imbibition cannot be applied to model the water transport within the paper. The authors argue that the change of surface tension will induce a significant modification in the bending response. In their work, a simple experiment was conducted to verify this hypothesis. The authors found that the bending responses of paper under the influence of water and water-surfactant were similar. However, the authors neglected the fact that the time response of capillary imbibition is dominated by the permeability of the media, which depends on the ratio of the surface tension and the viscosity. By adding surfactant not only the surface tension is modified but also the viscosity; then, the ratio between both properties has to be determined in order to discard capillary imbibition as the transport phenomenon. The lack of understanding regarding the water transport within paper in previous works represents

an important drawback in the study of the hygro-mechanical response of paper.

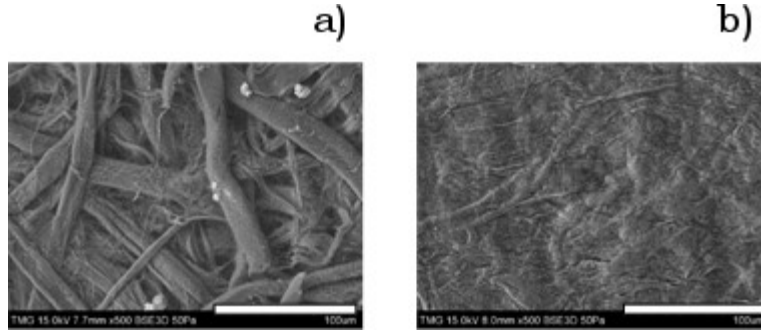


Figure 3.5 Comparison of 500X SEM images of a) tracing paper and b) filter paper. Bars scale represents 100  $\mu\text{m}$

The volumetric water content is related to the porosity of the material, which can be defined as the ratio of the pore volume of paper and the total volume of paper [144]. The visual comparison of filter and tracing paper using scanning electron microscopy (SEM) is illustrated in Fig. 3.5. It appears that the porosity of tracing paper is lower compared to that of the filter paper, which has larger voids among its fibers. However, one needs to account for the voids within the fibers as well since there is also water transport taking place through these micro-/nano- pores. Thus, despite the level of compactness of tracing paper as previously considered in [59] let us define paper as a porous material obeying Richard's equation for imbibition:

$$\frac{\partial \varphi}{\partial t} = \frac{\partial}{\partial x} \left( D(\varphi) \frac{\partial \varphi}{\partial x} \right) + \frac{\partial}{\partial z} \left( D(\varphi) \frac{\partial \varphi}{\partial z} \right) + \frac{\partial K(\varphi)}{\partial z} \quad (3.3)$$

where the moisture content in a continuum ( $\varphi$ ) region depends on moisture diffusivity and the conductivity functions of the medium,  $D(\varphi)$  and  $K(\varphi)$ , respectively. The initial moisture volumetric content is  $\varphi(z,0) = 0$  and the wetting boundary condition is saturated moisture ( $\varphi = \varphi_s$ ). It should be noted that the diffusivity and the conductivity are functions of the moisture content. Analyzing Eq. 3.3 it can be seen that a significant contribution of  $K(\varphi)$  will yield a nonhomogeneous moisture profile along  $z$  which would not concord with the straight final bending state observed in [58, 59]. Thus, it is suggested that the conductivity effect is extremely small compared to that of the diffusivity. In other works, the gravity effects are small enough to be neglected. Then, the moisture transport along the thickness of the paper can be expressed as presented in Eq. (3.4).

$$\frac{\partial \varphi}{\partial t} = \frac{\partial}{\partial x} \left( D(\varphi) \frac{\partial \varphi}{\partial x} \right) + \frac{\partial}{\partial z} \left( D(\varphi) \frac{\partial \varphi}{\partial z} \right) \quad (3.4)$$

As the water imbibition it is strongly dominated by the capillary pressure in the vertical direction, the problem can be reduced to the water imbibition into a thin rectangular section, similar to that described in chapter 2. In this case, the one dimension form of the Richard's equation is accurate enough to predict the imbibition. Thus, the one-dimension Richard's equation for unsaturated porous finite media in the water content form is applied [147].

$$\frac{\partial \varphi}{\partial t} = \frac{\partial}{\partial z} \left( D(\varphi) \frac{\partial \varphi}{\partial z} \right) \quad (3.5)$$

The moisture diffusivity can be expressed as

$$D(\varphi) = D_0 f_1(\varphi) \quad (3.6)$$

where  $f_1$  represents the characteristic function of the moisture diffusivity, and  $D_0$  the moisture diffusivity constant. Under Richards equation framework a good approximation of the diffusivity can be made by using the Brooks-Corey soil model as previously reported in [135]. Under this assumption, the diffusivity is described in this model as

$$f_1(\varphi) = \varphi^n(x, y) \quad (3.7)$$

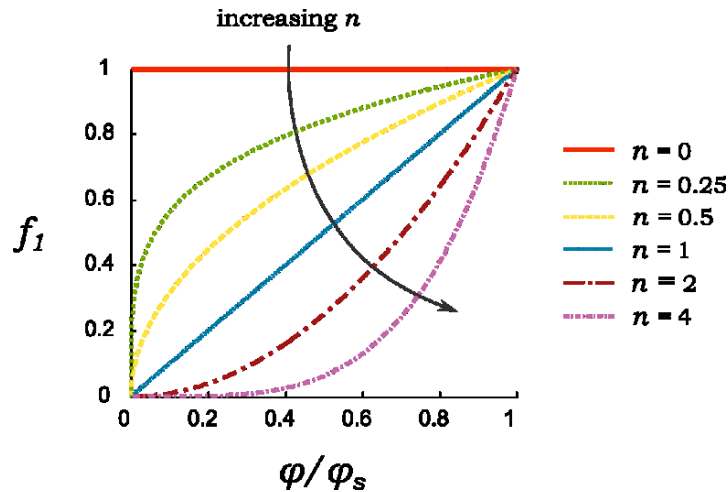


Figure 3.6  $f_1(\varphi)$  as a function of the normalized volumetric water content for various values of the exponent  $n$ .

The power term  $n$  dictates the dynamic response of the water transport, which is related to the moisture distribution along the thickness. Hence, it

is expected that a modification of the diffusion response due to the nonlinear diffusivity may have a significant effect on the curvature response of paper. It is important to establish that  $D_0$  is an equivalent diffusivity function that is not related to the molecular diffusivity. The plot of  $f_1$  for different values of  $n$  is presented in Fig. 3.6.

### 3.2.2 Hygroexpansive strain

The hygroexpansive strain can be expressed as a function of the hygroexpansive strain at saturation  $\varepsilon_{max}$  and the characteristic function  $f_2$ :

$$\varepsilon_h(\varphi) = \varepsilon_{max}f_2(\varphi) \quad (3.8)$$

It has been suggested that the hygroexpansive strain is linearly proportional to the moisture content [144], in such a case  $f_2 = \varphi$ . Models in [58, 59] assume this condition for the actuation strain in paper. However, a simple empirical expression for  $f_2$  can be defined as:

$$f_2(\varphi) = \varphi^p(x, y) \quad (3.9)$$

In this case, other possible scenarios rather than the linear one may be explored. As shown in Fig. 3.7. The cases in which the hygroexpansive strain responds faster ( $p=0.25$ ) and slower ( $p=4$ ) to the moisture content compared to the linear case can be examined using Eq. 3.9.

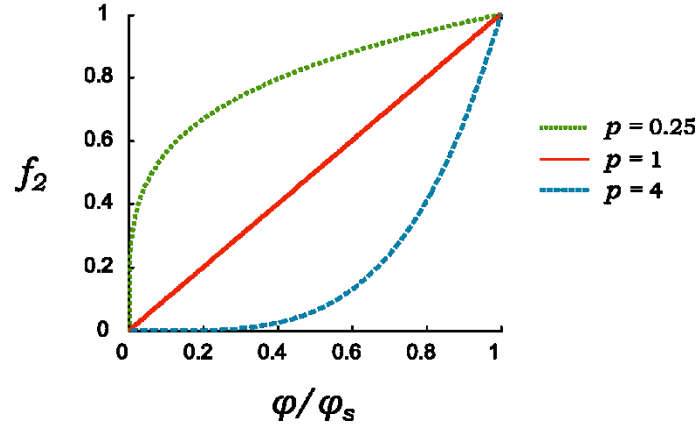


Figure 3.7  $f_2(\varphi)$  as a function of the normalized volumetric water content for different values of the exponent  $p$ .

### 3.2.3 Relaxation

Authors in [59] defined an empirical function to account for the relaxation of the wet paper. They suggested that such relaxation may be described as:

$$E(\varphi) = E_{dry}e^{-\beta\varphi(z,t)} \quad (3.10)$$

where  $\beta$  can be defined as a relaxation constant and  $E_{dry}$  as Young modulus of elasticity for dry paper. However, this function would not match the experimental results in [60]. In this regard another empirical function to take into consideration the relaxation of the Young modulus of elasticity is proposed. This expression is proposed based on the experimental results observed in [60]

$$E(\varphi) = E_{dry}f_3(\varphi) \quad (3.11)$$

where the function  $f_3$  can be defined as:

$$f_3(\varphi) = \frac{1}{m^{-1} + (1 - m^{-1})e^{-\beta\varphi(z,t)}} \quad (3.12)$$

where  $m$  represents the ratio between wet and dry Young modulus of elasticity. The shape of  $f_3$  for relaxation of the Young modulus of elasticity ranging from 0 to 4 orders of magnitude is presented in Fig. 3.8.

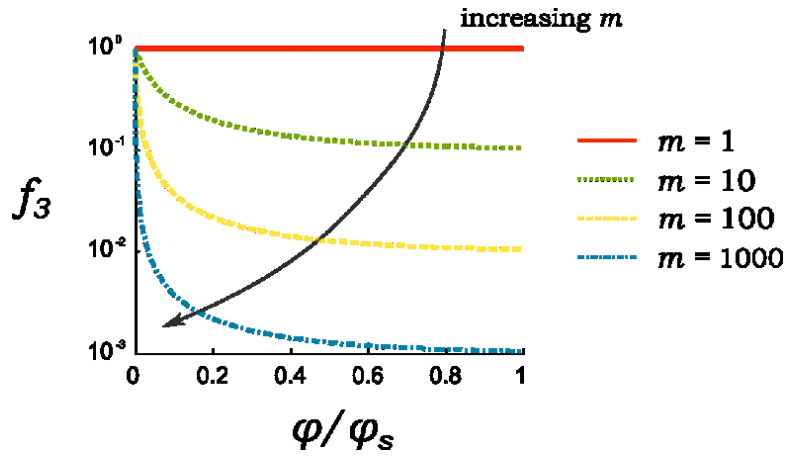


Figure 3.8  $f_3(\varphi)$  as a function of the normalized volumetric water content for various values of  $m$  and  $\beta=2$ .

### 3.2.4 Plane stress

Paper mechanics can be analyzed at three levels: macro, meso- and micro-scale [148]. In the former, the paper fibers are represented as a set of layers formed by a bunch of microfibrils. Each layer has a specific microfibril orientation and a different content of cellulose, hemicellulose, and lignin. In the meso-scale, fibers are assumed as equivalent elastic cells that form a porous matrix. Finally, at the macro scale, paper is assumed as a solid material with equivalent mechanical properties such as

Young modulus and Poisson's ratio. Further on, paper mechanics is studied at the macro-level as reported in previous works [57-60, 149]. Figure 3.9 shows the stress state of an infinitesimal element acting on a piece of paper. In this configuration, the thickness is parallel to the axis  $z$ .

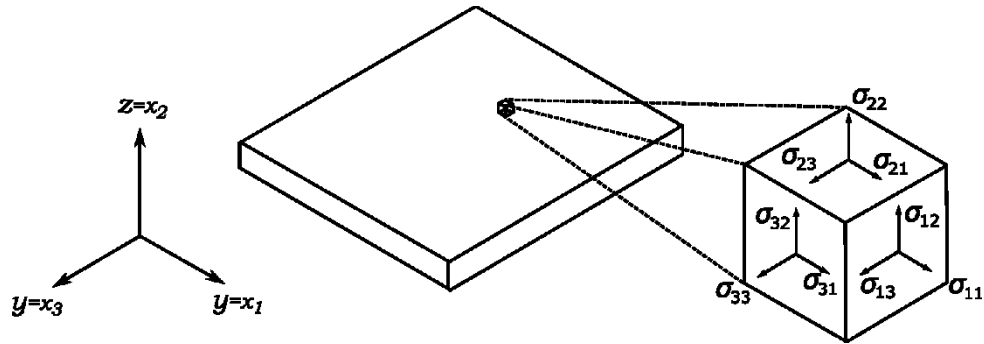


Figure 3.9 Schematic representation of stresses acting on an infinitesimal element of a piece of paper.

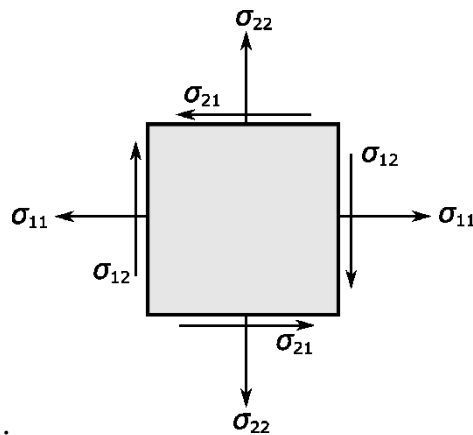


Figure 3.10 Schematic representation of plane stresses.

In the case of slender beams the stress state can be reduced to a plane stress problem where  $\sigma_{33} = \sigma_{32} = \sigma_{31} = \sigma_{13} = \sigma_{23} = 0$ . Thus, the two dimensional plane stress can be represented as depicted in Fig. 3.10.

Paper can be assumed as an orthotropic material [148] obeying the following strain-stress relationships:

$$\begin{Bmatrix} \varepsilon_{11} \\ \varepsilon_{22} \\ \varepsilon_{12} \end{Bmatrix} = \begin{bmatrix} \frac{1}{E} & -\frac{\nu}{E} & 0 \\ -\frac{\nu}{E} & \frac{1}{E} & 0 \\ 0 & 0 & \frac{1}{2G_{23}} \end{bmatrix} \begin{Bmatrix} \sigma_{11} \\ \sigma_{22} \\ \sigma_{12} \end{Bmatrix} \quad (3.13)$$

### 3.3 Reduced model

The bending problem can be described as a slender beam under the influence of a hygroexpansive strain input. The Euler-Bernoulli beam theory for small deformations, in which the strain components  $\varepsilon_{22}$  and  $\varepsilon_{12}$  can be neglected yielding to a pure bending state represented in Fig. 3.11, can be applied. In this case Eq. 3.13 reduced to the one dimension form

$$\varepsilon_{11} = \frac{1}{E} \sigma_{11} \quad (3.14)$$

In pure bending, the strain distribution along the thickness of the paper-based beam is considered as linear. As it can be seen in Fig. 3.11 the reference plane is set at  $z=0$ , and the neutral plane is defined as that in which the bending strain is zero. Moreover,  $R(t)$  represents the radius of curvature at the reference plane at a given time. The bending angle at any point can be expressed as a function of the radius of curvature and the deformed length at any point of  $z$ :

$$\vartheta(t) = \frac{l + \Delta l_b(z, t)}{\{R(t) - z\}} \quad (3.15)$$

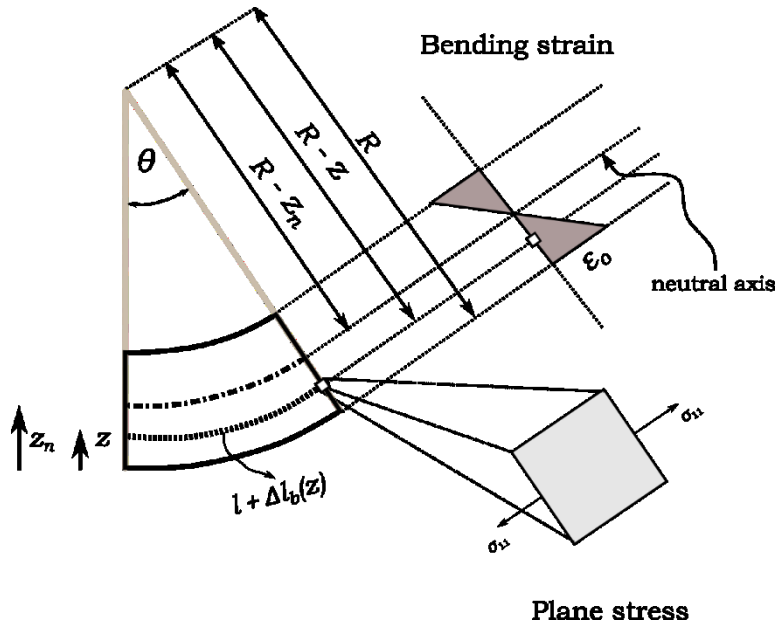


Figure 3.11 Schematic representation of pure bending state of a paper beam experiencing hygroexpansive strain actuation.

At the neutral axis the bending angle can be expressed as:

$$\vartheta(t) = \frac{l}{\{R(t) - z_n(t)\}} = l\kappa_n(t) \quad (3.16)$$

where  $\kappa_n$  is the curvature at the neutral axis. Combining Eqs. 3.15 and 3.16 the following relationship is found:

$$\frac{\Delta l_b(z, t)}{l} = \kappa_n \{R(t) - z\} - 1 \quad (3.17)$$

The left-hand side expression is nothing but the bending strain defined in Eq. 3.2. Thus the distribution of the bending strain along the z-axis can be expressed as:

$$\varepsilon_b(z, t) = \varepsilon_o(t) - \kappa_n(t)z \quad (3.18)$$

Where  $\varepsilon_o(t)$  is the bending strain at the reference level ( $z=0$ ) and is defined as:

$$\varepsilon_o(t) = \kappa_n(t)/\kappa_o(t) - 1 \quad (3.19)$$

Here,  $\kappa_o(t)$  stands for the curvature at the reference plane which is different from that at the neutral axis. Finally the neutral axis as a function of time can be represented as:

$$z_n(t) = \frac{1}{\kappa_o(t)} - \frac{1}{\kappa_n(t)} \quad (3.20)$$

Hence, the total strain  $e(z, t)$  can be represented by the difference between the bending and hygroexpansive strain as

$$\varepsilon(z, t) = \varepsilon_b(z, t) - \varepsilon_h(z, t) \quad (3.21)$$

The stress  $\sigma(z, t)$  can be calculated using Eq. 3.9, 3.12 and 3.14 as:

$$\sigma(z, t) = Ef_3(\varphi(z, t))\{\varepsilon_o(t) - \kappa_n(t)z - \varepsilon_{max}f_2(\varphi(z, t))\} \quad (3.22)$$

Finally, given the fact that the beam is not subject to any external load the force and moment equilibrium yields to Eqs. 3.23a-b. The curvature at any time  $\kappa_n(t)$  can be therefore evaluated by solving Eqs. 3.5 and 3.23a-b.

$$\int_0^h \sigma(z, t) dz = 0 \quad (3.23a)$$

$$\int_0^h \sigma(z, t) z dz = 0 \quad (3.23b)$$

### 3.3.1 Dimensionless formulation

In order to synthesize the analysis of the problem a dimensionless formulation is presented in this section. In this light, the following dimensionless parameters are introduced

$$\bar{z} = \frac{z}{h} \quad (3.24a)$$

$$\phi = \frac{\varphi}{\varphi_s} \quad (3.24b)$$

$$\bar{t} = \frac{t}{\tau} \quad (3.24c)$$

$$\bar{\kappa} = \frac{\kappa_n}{\eta} \quad (3.24d)$$

where  $\tau$  is the time-scale of the problem [s] and  $\eta$  represents the gain of the curvature [ $\text{mm}^{-1}$ ]. By balancing the time derivative with the diffusivity term in Eq. 3.5 the time-scale can be represented as

$$\tau = \frac{h^2}{D_0 \varphi_s} \quad (3.25)$$

Similarly, the gain of the curvature can be obtained as

$$\eta = \frac{\varepsilon_{max}}{h} \quad (3.26)$$

which denotes the ratio between the maximum hygroexpansive strain ( $\varepsilon_{max}$ ) and the thickness ( $h$ ). Thus, the nondimensionalized problem can be expressed as

$$\frac{\partial \phi}{\partial \bar{t}} = \frac{\partial}{\partial \bar{z}} \left( \phi^n \frac{\partial \phi}{\partial \bar{z}} \right) \quad (3.27a)$$

with the initial condition,

$$\phi(\bar{z}, 0) = 0 \quad (3.27b)$$

moreover, the boundary conditions

$$\phi(0, \bar{t}) = 1 \quad (3.27c)$$

$$\phi^n \frac{\partial \phi}{\partial \bar{z}} \Big|_{\bar{z}=1} = 0 \quad (3.27d)$$

subject to

$$\int_0^1 f_3(\phi(\bar{z}, \bar{t})) \left( \bar{\varepsilon}_0(\bar{t}) - \bar{\kappa}(\bar{t})\bar{z} - f_2(\phi(\bar{z}, \bar{t})) \right) d\bar{z} = 0 \quad (3.28a)$$

$$\int_0^1 \left\{ f_3(\phi(\bar{z}, \bar{t})) \left( \bar{\varepsilon}_0(\bar{t}) - \bar{\kappa}(\bar{t})\bar{z} - f_2(\phi(\bar{z}, \bar{t})) \right) \right\} \bar{z} d\bar{z} = 0 \quad (3.28b)$$

If the moisture distribution  $\phi(\bar{z}, \bar{t})$  is known the solution of Eqs. 3.12 and 3.15 can be expressed as a linear system as that described in [150] for bending response of multilayer beams:

$$\begin{bmatrix} a_{11} & -a_{12} \\ a_{12} & -a_{22} \end{bmatrix} \begin{bmatrix} \bar{\varepsilon}_0(\bar{t}) \\ \bar{\kappa}(\bar{t}) \end{bmatrix} = \begin{bmatrix} b_1 \\ b_2 \end{bmatrix} \quad (3.29)$$

Thus, the solution of the bending state at any time  $\bar{t}$  is given by:

$$\bar{\kappa}(\bar{t}) = (a_{11}b_2 - a_{12}b_1)/(-a_{11}a_{22} + a_{12}^2) \quad (3.30)$$

$$\bar{\varepsilon}_0(\bar{t}) = (a_{12}b_2 - b_1a_{22})/(-a_{11}a_{22} + a_{12}^2) \quad (3.31)$$

where the elements  $a$  and  $b$  of the linear system are defined as follows:

$$a_{11} = \int_0^1 f_3(\varphi) d\bar{z} \quad (3.32a)$$

$$a_{12} = \int_0^1 f_3(\varphi) \bar{z} d\bar{z} \quad (3.32b)$$

$$a_{22} = \int_0^1 f_2(\varphi) \bar{z}^2 d\bar{z} \quad (3.32c)$$

$$b_1 = \int_0^1 f_3(\varphi) f_2(\varphi) d\bar{z} \quad (3.32d)$$

$$b_2 = \int_0^1 f_3(\varphi) f_2(\varphi) \bar{z} d\bar{z} \quad (3.32e)$$

### 3.3.2 Bending response

The linear solution using LW theory is analyzed in this section to provide one useful reference to examine the hygro-mechanical bending response. In this case, there is neither moisture diffusivity nor relaxation of the Young modulus of elasticity. In addition, the hygroexpansive strain is found to be linearly proportional to the volumetric water content. Table 3.1 summarizes the equivalent functions  $f_i$  that described this scenario.

Table 3.1 Equivalent functions  $f_i$  for LW case

$f_1(\varphi)$	$f_2(\varphi)$	$f_3(\varphi)$
0	$\phi(\bar{z}, \bar{t})$	1

In this particular case, a discrete boundary between the saturated and unsaturated zone is considered. Such boundary condition was observed in the experiments carried out with chromatography paper in the previous chapter. In other words, the media is seen as a binary state either wet or non-wet zone. This problem represents a bilayer beam with hygroexpansive strain acting on the bottom layer as discussed in [58]. In this case, the moisture distribution can be represented as:

$$\varphi(\bar{z}, \bar{t}) = \begin{cases} 1, & \bar{z}(\bar{t}) \leq \bar{z}_w(\bar{t}) \\ 0, & \bar{z}(\bar{t}) > \bar{z}_w(\bar{t}) \end{cases} \quad (3.33)$$

where

$$\bar{z}_w(\bar{t}) = \sqrt{\bar{t}} \quad (3.34)$$

The solution of Eq. 3.32 yields to  $a_{11}=1$   $a_{12}=1/2$   $a_{22}=1/3$ : thus, the dimensionless curvature and the strain can be expressed as:

$$\bar{\kappa}(\bar{t}) = -12 \left( \int_0^1 \varphi(\bar{z}, \bar{t}) \bar{z} d\bar{z} - \frac{1}{2} \int_0^1 \varphi(\bar{z}, \bar{t}) d\bar{z} \right) \quad (3.35)$$

$$\bar{\varepsilon}_0(\bar{t}) = -12 \left( \frac{1}{2} \int_0^1 \varphi(\bar{z}, \bar{t}) \bar{z} d\bar{z} - \frac{1}{3} \int_0^1 \varphi(\bar{z}, \bar{t}) d\bar{z} \right) \quad (3.36)$$

The solution of this case is:

$$\bar{\kappa}(\bar{t}) = 6\bar{z}_w(1 - \bar{z}_w(\bar{t})) \quad (3.37)$$

$$\bar{\epsilon}_0(\bar{t}) = \bar{z}_w(\bar{t})(4 - \bar{z}_w(\bar{t})) \quad (3.38)$$

Using the above expressions one can examine the characteristic hygro-mechanical bending response with respect to time. Fig. 3.12 shows the curvature response as a function of the dimensionless time. As it is expected the bending curvature rises from a zero at  $p_1$  until a maximum point at  $p_3$ ; then, the curvature starts to decrease to  $p_5$ . The authors of [58, 59] focused their analysis only on the curvature, which is relatively easy to measure. However, to know the complete bending state one has to look at the bending strain as well. For instance, the two points  $p_2$  and  $p_4$  in Fig. 3.12a have the same bending curvature, but different bending strain at the bottom level as can be seen in Figure 3.12b. Thus, any combination of both  $\bar{\kappa}$  and  $\bar{\epsilon}_0$  determines a unique bending state during the time response.

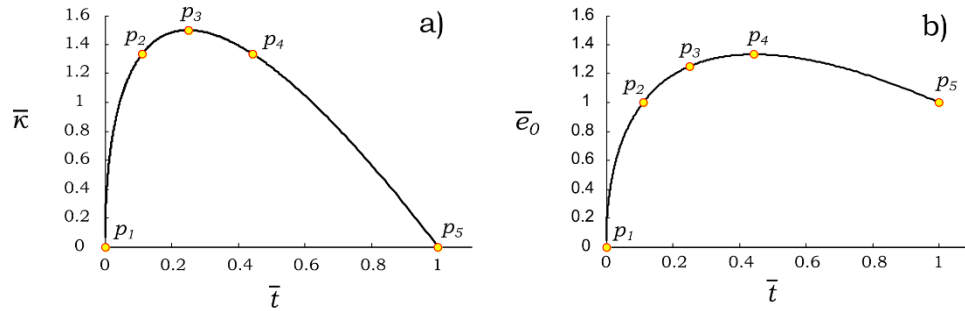


Figure 3.12 Pure bending response of a paper beam undergoing hygroexpansive strain actuation a) curvature b) bending strain at  $z=0$ .

Thus, it is suggested that a bending state analysis including both curvature and strain can provide a better understanding of the hygro-

mechanical response compared to previous discussions presented in [58, 59]. In this regard, a bending state plot is suggested to describe the bending state cycle. Such a plot is presented in Fig. 3.13, which shows the bending state of the five points  $p_i$  in Fig. 3.12a-b.

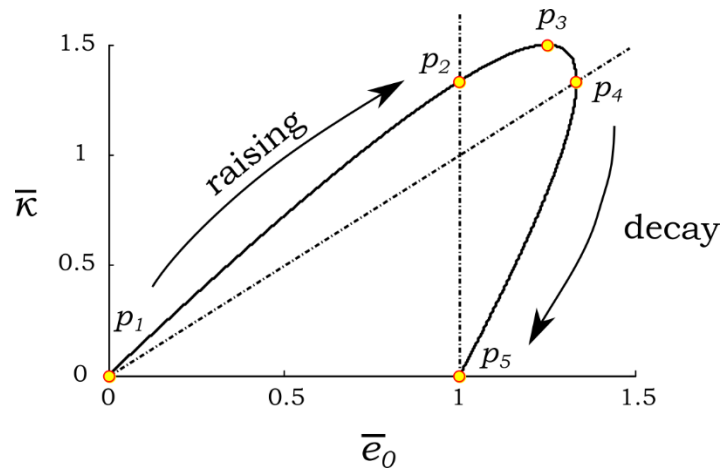


Figure 3.13 Hygro-mechanical bending state cycle of a paper beam due to hygroexpansive strain actuation.

Using the proposed bending state plot is possible to obtain the strain distribution in the paper beam. For instance, let us consider the point  $p_2$  ( $\bar{\kappa}=1, \bar{\epsilon}_0=4/3$ ) in Fig. 3.13. The curvature ( $\bar{\kappa}$ ) provides us information regarding the slope of the bending strain distribution as can be seen in Fig. 3.15b. However, it not possible to evaluate the bending strain distribution along the thickness of the beam without knowing one point within the linear distribution. In this light, the bending strain at the reference level ( $\bar{\epsilon}_0$ ) completes the necessary information to evaluate the bending strain distribution. Moreover, the total strain can be evaluated once the bending strain is assessed using Eq. 3.21. The estimation of the

total strain distribution at  $p_2$  is illustrated in Fig. 3.14a. Here, it can be seen that the beam experiences a compression-tension-compression (CTC) state from bottom to top with two neutral axes. Hence, it is suggested the analysis of the total strain distribution may contribute to the characterization of the hygro-mechanical bending response.

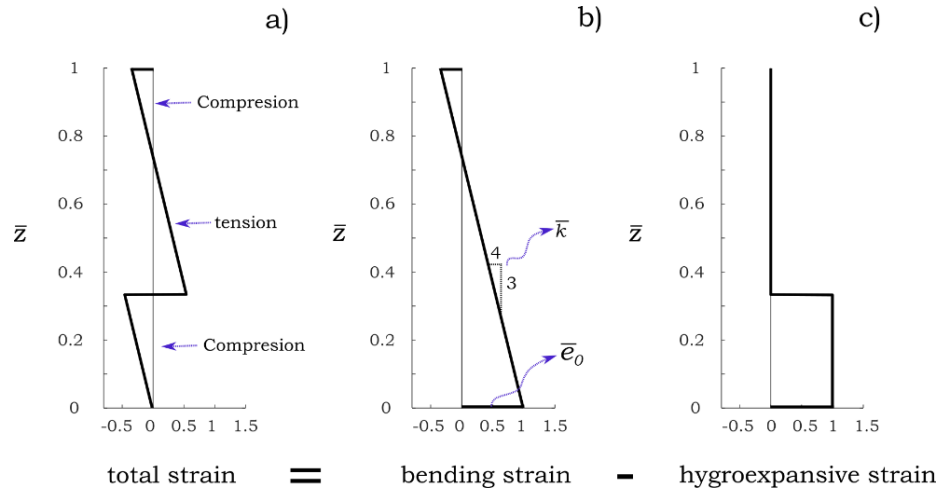


Figure 3.14 Strain state distribution at  $p_2$  a) total strain, b) bending strain, and c) hygroexpansive strain.

The total strain distribution of the points depicted in the bending state plot (Fig. 3.13) is presented in Fig. 3.15. The physical meaning of this distribution can be summarized as follows:

- At  $p_1$  the total strain is initially zero along the thickness of the paper-based beam. The beam does not experience either actuation strain nor bending strain;
- Then, the beam starts to bend until  $p_2$ , where the total strain at the bottom surface of the beam is zero. In other words, the bottom layer does not experience neither tension nor compression;

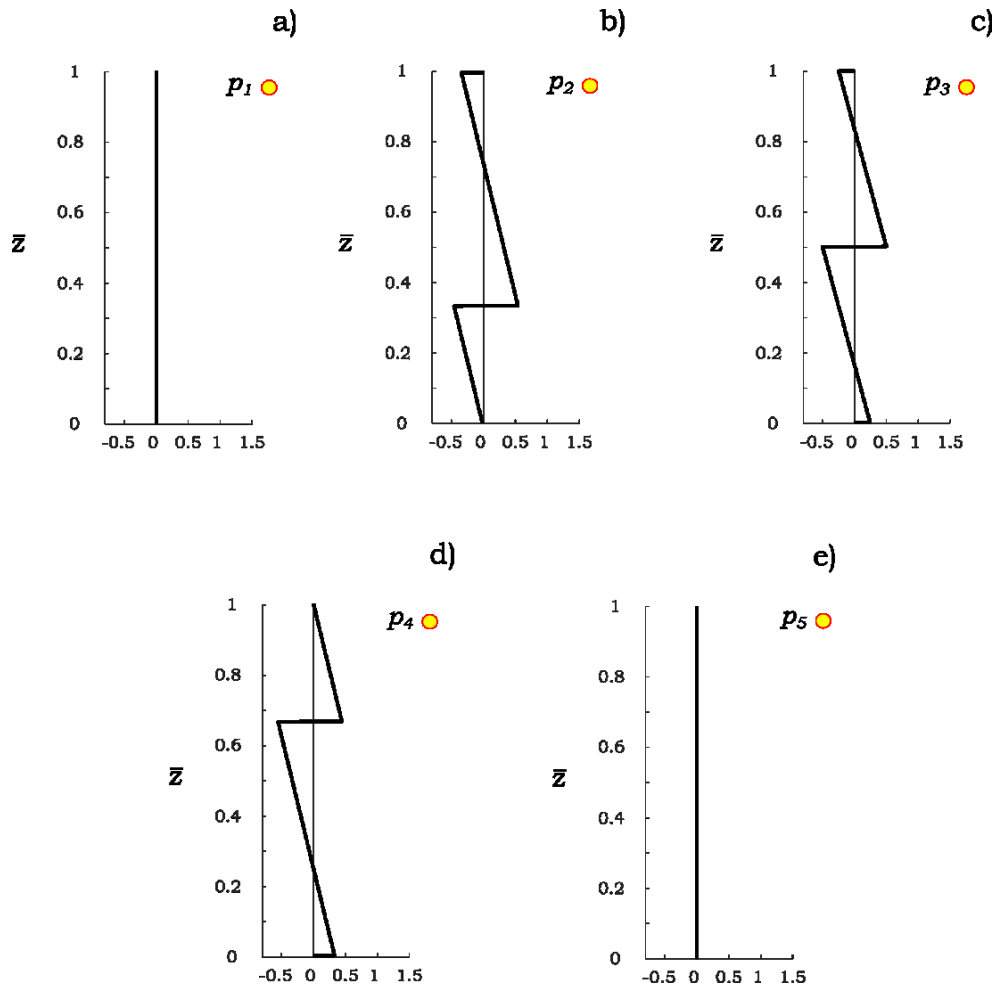


Figure 3.15 Total strain state distribution of a)  $p_1$ , b)  $p_2$ , c)  $p_3$ , d)  $p_4$ , and e)  $p_5$  from bending state plot presented in Fig. 3.13.

- The maximum curvature is achieved at  $p_3$ . Here the bending strain energy is maximum as this energy is proportional to the curvature;
- At  $p_4$  the bottom surface experiences the total strain extension (1/3), here upper surface ( $z=1$ ) of the beam exhibits neither tension nor compression;

- Finally, at  $p_5$  the total strain goes back to zero when the hygroexpansive strain is homogenous along the thickness of the paper. Here, the beam experiences hygroexpansive growth but not internal stresses.

Thus, one alternative approach to analyzing the hygro-mechanical bending response of paper-beams is to look at the pure bending state cycle instead of the time responses. Similar to the previous example, other points can be analyzed in the bending state cycle plot. It is expected that the individual influences of the three phenomena involved in the problem can be assessed by analyzing the bending state cycle instead of comparing the time responses. Such influences will be discussed in next the chapter.

### 3.4 Summary

An introduction to the hygro-mechanical response of paper-beams was discussed in this chapter. The three phenomena occurring during the bending response were analyzed. A practical imbibition-beam model that describes the characteristic bending response was developed. The dimensionless formulation of the proposed model provide a simple means to assess the individual influences of the three inherent phenomena on the characteristic bending response. The analysis of one example assuming LW imbibition was presented. A bending state cycle plot was proposed to analyze the hygro-mechanical bending response of paper-based beams.

The proposed model will be applied in next chapter to analyze the nonlinear influences on the bending state.

## Chapter 4 Nonlinear influences on the hygro-mechanical bending response of paper

*Previous formulations [58, 59] account only for one nonlinearity source related to the softening effect due to an increment on the moisture content in the paper. In this chapter the nonlinear influences on the hygro-mechanical bending response of paper-based beams are studied. In order to analyze such influences, the material nonlinearities are described by means of three functions dependent on three dimensionless parameters as described in chapter 3. The influences on both bending state and total strain distribution are studied to provide a better understanding of the phenomenon. The analytical solution of the linear problem is presented with the aim to provide a reference for comparing the aforesaid nonlinear effects. Finally, the proposed formulation is applied to describe the bending response of the experimental results presented in [59].*

## 4.1 Nonlinearity sources

It is evident that the nonlinearity sources in the hygro-mechanical actuation of paper-based beams play a major role in the typical bending response. According to Changizi [151] the nonlinearity sources in mechanical engineering can be divided into those related to the geometry and material properties. Geometrical nonlinearity is due to the nonlinear strain-displacement relationship, also known as large deformation or finite strain. Material nonlinearities are related to the nonlinear response of certain materials to a given physical input. In this chapter, the geometrical and material nonlinear influences are investigated using the formulation developed in chapter 3. The material nonlinearities in hygro-mechanical bending response can be represented using Eq. 3.6, 3.8 and 3.10. Table 4.1 presents the summary of the equivalent functions  $f$  describing the different scenarios. The linear case represents the linear form of the imbibition problem, a linear hygroexpansive strain actuation and no relaxation occurring during the bending cycle. The analytical linear solution of the problem is presented in next section in order to provide a reference to study the nonlinear effects. The solution of the nonlinear imbibition problem (Eqs. 3.27a-d) is carried out numerically by means of the finite difference PDE solver of MatLab, while the solution of the mechanical problem (Eqs. 3.32a-e) was obtained using numerical integration. Finally, the solution of nonlinear geometry problem was

performed using finite element software COMSOL. For more details about this solution refer to Appendix B.

Table 4.1 Equivalent functions  $f_i$  for accounting for nonlinear influences

Nonlinearity influence	$f_1(\varphi)$	$f_2(\varphi)$	$f_3(\varphi)$
None (linear problem)	1	$\phi(\bar{z}, \bar{t})$	1
Imbibition	$\phi^n(\bar{z}, \bar{t})$	$\phi(\bar{z}, \bar{t})$	1
Swelling	1	$\phi^p(\bar{z}, \bar{t})$	1
Relaxation	1	$\phi(\bar{z}, \bar{t})$	$\frac{1}{m^{-1} + (1 - m^{-1})e^{-2\phi(\bar{z}, \bar{t})}}$
Imbibition, swelling and relaxation	$\phi^n(\bar{z}, \bar{t})$	$\phi^p(\bar{z}, \bar{t})$	$\frac{1}{m^{-1} + (1 - m^{-1})e^{-2\phi(\bar{z}, \bar{t})}}$

#### 4.1.1 Linear problem

When  $f_1(\varphi) = 1$  Richard's equation is reduced to the linear form that can be solved using variable separation. In this case, the solution of the moisture content yields to [152]

$$\varphi(\bar{z}, \bar{t}) = 1 - \sum_{i=1}^{\infty} \frac{2}{\lambda_i} \sin(\lambda_i \bar{z}) e^{-\lambda_i^2 \bar{t}} \quad (4.1)$$

where

$$\lambda_i = \frac{(2i - 1)\pi}{2} \quad (4.2)$$

Thus, using Eq. 3.25 the dimensionless curvature can be expressed as

$$\bar{\kappa}(\bar{t}) = \sum_{i=1}^{\infty} \bar{a}_i e^{-\lambda_i^2 \bar{t}} \quad (4.3)$$

where

$$\bar{a}_i = (-12) \left[ \frac{\lambda_i + 2(-1)^i}{\lambda_i^3} \right] \quad (4.4)$$

Likewise, the reference strain can be expressed as

$$\bar{\varepsilon}_0(\bar{t}) = \sum_{i=1}^{\infty} \bar{b}_i e^{-\lambda_i^2 \bar{t}} \quad (4.5)$$

with

$$\bar{b}_i = (-12) \left[ \frac{\frac{2}{3}\lambda_i + (-1)^i}{\lambda_i^3} \right] \quad (4.6)$$

Table 4.2 First five values of  $\lambda_i^2, a_i$  and  $b_i$  of Eqs. 4.2, 4.5 and 4.7

$i$	$\lambda_i^2$	$\bar{a}_i$	$\bar{b}_i$
1	1/4	1.329	-0.146
2	9/4	-0.770	-0.475
3	49/4	-0.145	-0.105
4	81/4	-0.117	-0.075
5	121/4	-0.052	-0.036

The solution of this problem points to the same solution considering molecular diffusion problem presented in [59]. The first fifth values of

$\lambda_i^2$ ,  $\bar{a}_i$  and  $\bar{b}_i$  are presented in Table 4.2. The time responses of the curvature and bending strain at the reference level are presented in Fig 4.1. It can be seen that the analytical solution is in good agreement with the numerical solution.

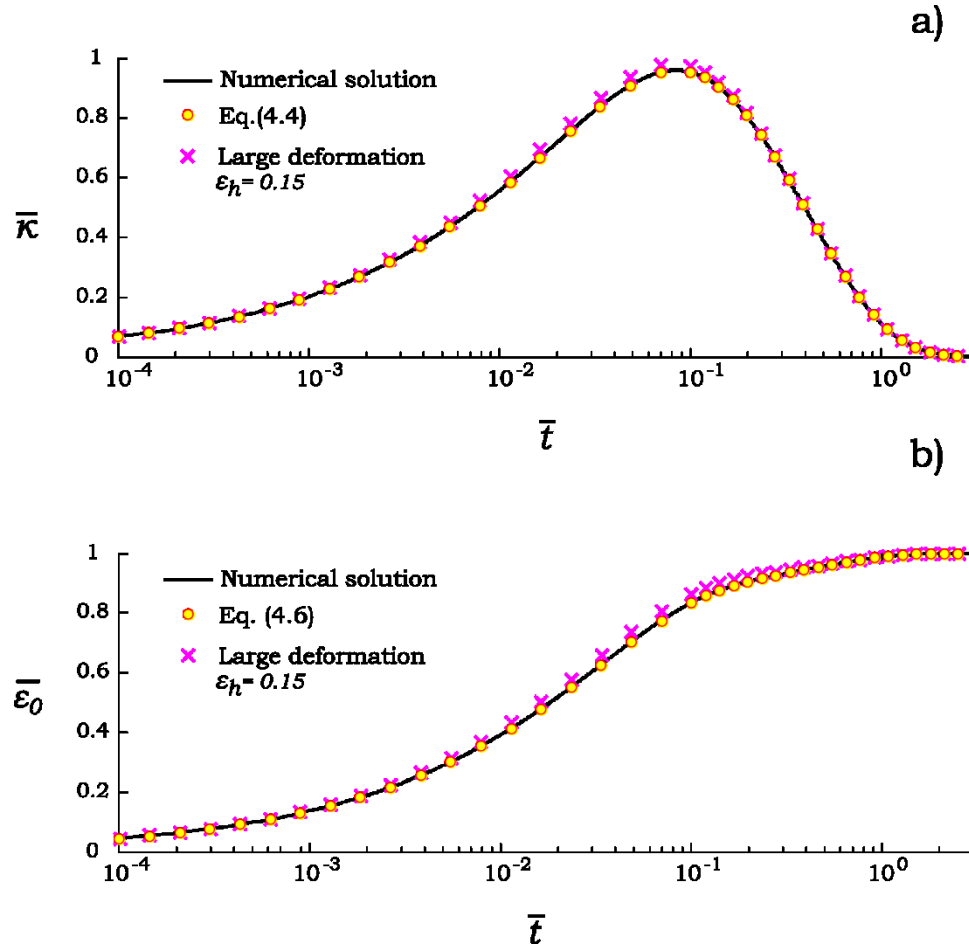


Figure 4.1 Hygro-mechanical bending response of a paper beam considering linear imbibition a) bending curvature and b) bending strain at reference level. Comparison among analytical, numerical and large deformation solutions.

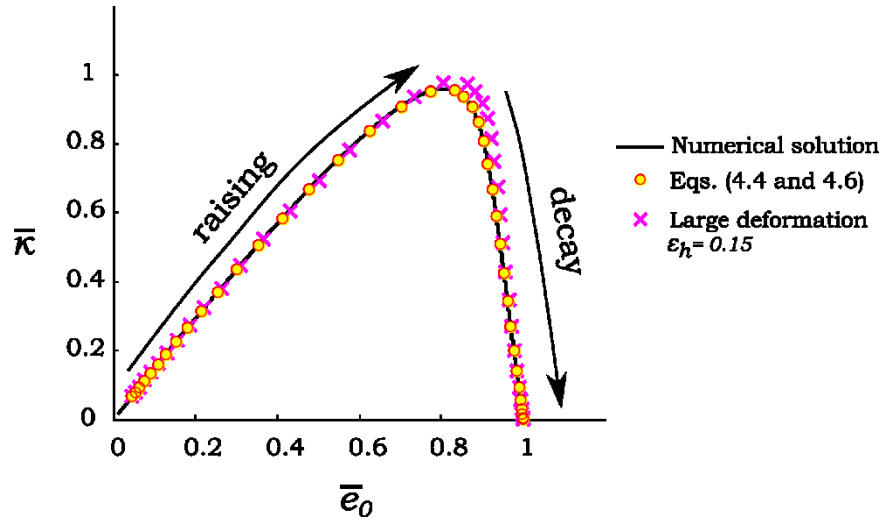


Figure 4.2 Hygro-mechanical bending state cycle using linear imbibition theory. Comparison among analytical, numerical and large deformation solutions.

One advantage of the dimensionless formulation developed in chapter 3 is that one can perform a simple comparison of the solution of the problem under different scenarios with respect to previous works [58, 59]. In this regard, the bending state plot provides an easy way to compare two scenarios. The bending state plot for the case of linear imbibition is presented in Fig. 4.2. In this case, two main differences with respect to the LW model are found. Such a solution is based on the Timoshenko bilayer problem [153] and was presented in chapter 3. First, it can be seen in Fig. 4.2 that the maximum curvature using linear imbibition is  $\bar{\kappa} = 0.96$ , which is almost 50% lower compared to the LW theory ( $\bar{\kappa} = 1.5$ ). This effect has been previously reported in [152]. Second, it is also interesting to look at the effect on the bending strain at the reference level. The results suggest that the bending strain at the reference level is always less than one during

the bending response. This implies that the extension of the bottom surface of the beam is always less than the hygroexpansion during the whole bending cycle.

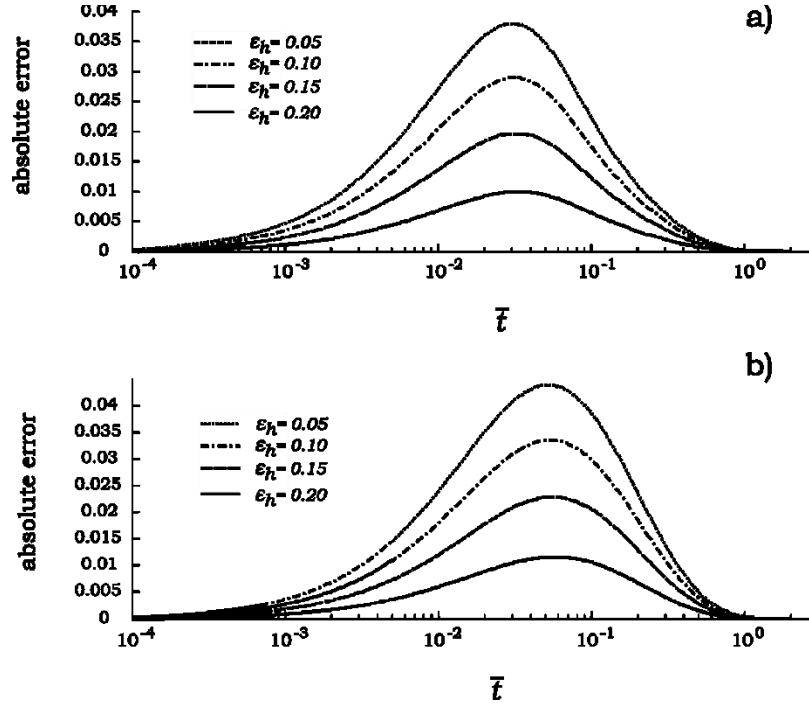


Figure 4.3 Error of the proposed model assuming linear imbibition theory due to geometrical nonlinearities. Absolute errors of both a) curvature and b) bending strain at reference level are presented. The hygroexpansive strain actuations applied are 0.05, 0.1, 1.15 and 0.2.

## 4.2 Nonlinear geometry

It has been suggested by Rafsanjani et al. [50] that the assumption of Euler-Bernoulli beam theory for the case of bilayer beams yields significant errors when dealing with moderate large strain actuation. For the linear imbibition case, the difference on the bending curvature and

strain reference under a hygroexpansive strain actuation of 0.15 is depicted in Fig. 4.1 and 4.2. The absolute error of both curvature and reference strain under strain actuation of 0.05, 0.10, 0.15 and 0.2 is presented in Fig. 4.3. It can be seen that the maximum absolute error occurs near to the maximum curvature.

Table 4.3 Relative error on curvature and bending strain reference due to nonlinear geometry.

Hygroexpansive strain	Curvature		Bending strain reference	
	RMSE	Maximum	RMSE	Maximum
0.05	0.6%	1.3%	0.9%	1.7%
0.1	1.3%	2.6%	1.8%	3.4%
0.15	1.9%	3.8%	2.6%	5.1%
0.2	2.5%	5%	3.4%	6.8%

The effect on the nonlinear geometry on the bending state cycle can be summarized in Table 4.3. This table presents the corresponding root mean square and maximum absolute errors corresponding to Fig. 4.3. It can be seen that the maximum relative error to predict the bending curvature increase from 1.3% to 5% when increasing the hygroexpansive strain from 0.05 to 0.2. Hygroexpansive strains below 0.1 have been reported in [58, 59]; in this case, the maximum relative error of both curvature and strain reference are 2.6% and 3.4%, respectively. Thus, it is important to

emphasize that the following discussion on the material nonlinearities using the proposed model is restricted to the case of moderate hygroexpansive strains actuation ( $\varepsilon_h > 0.15$ ), which leads to an error lower than 5.1% on both curvature and strain reference. As an example, the maximum bending curvature of a slender beam ( $l/h=30$ ) experiencing different hygroexpansive strains is illustrated in Fig. 4.4.

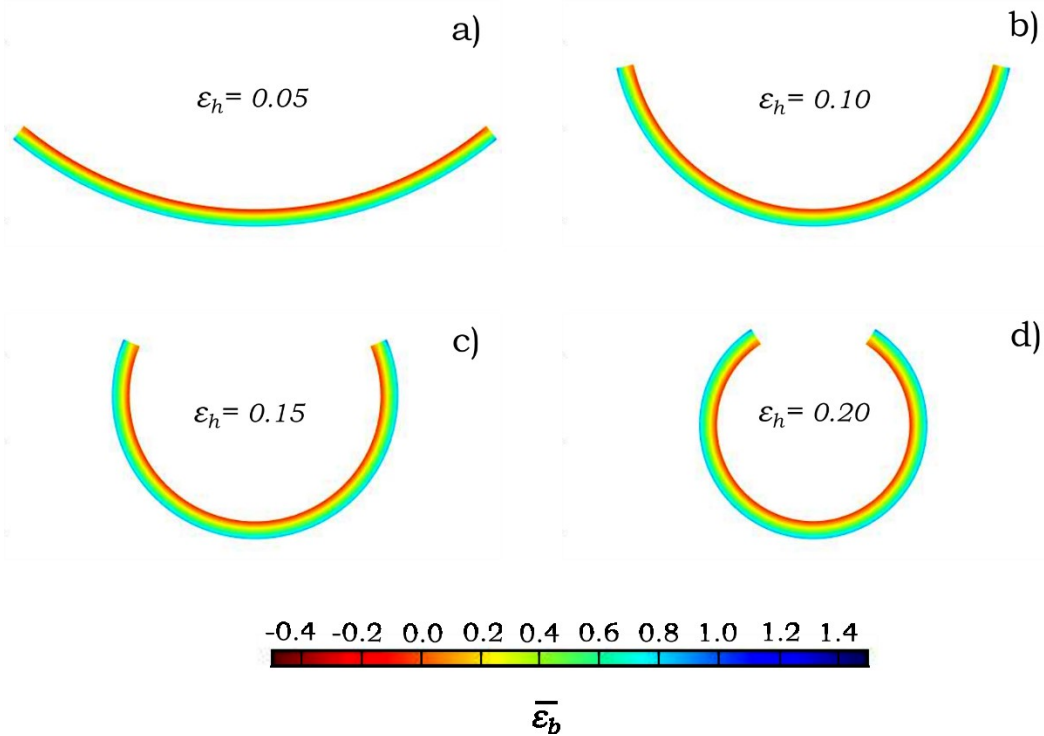


Figure 4.4 Illustration of the maximum bending curvature of a slender beam experiencing hygroexpansive strain actuation of a) 0.05, b) 0.10, c) 0.15 and d) 0.20.

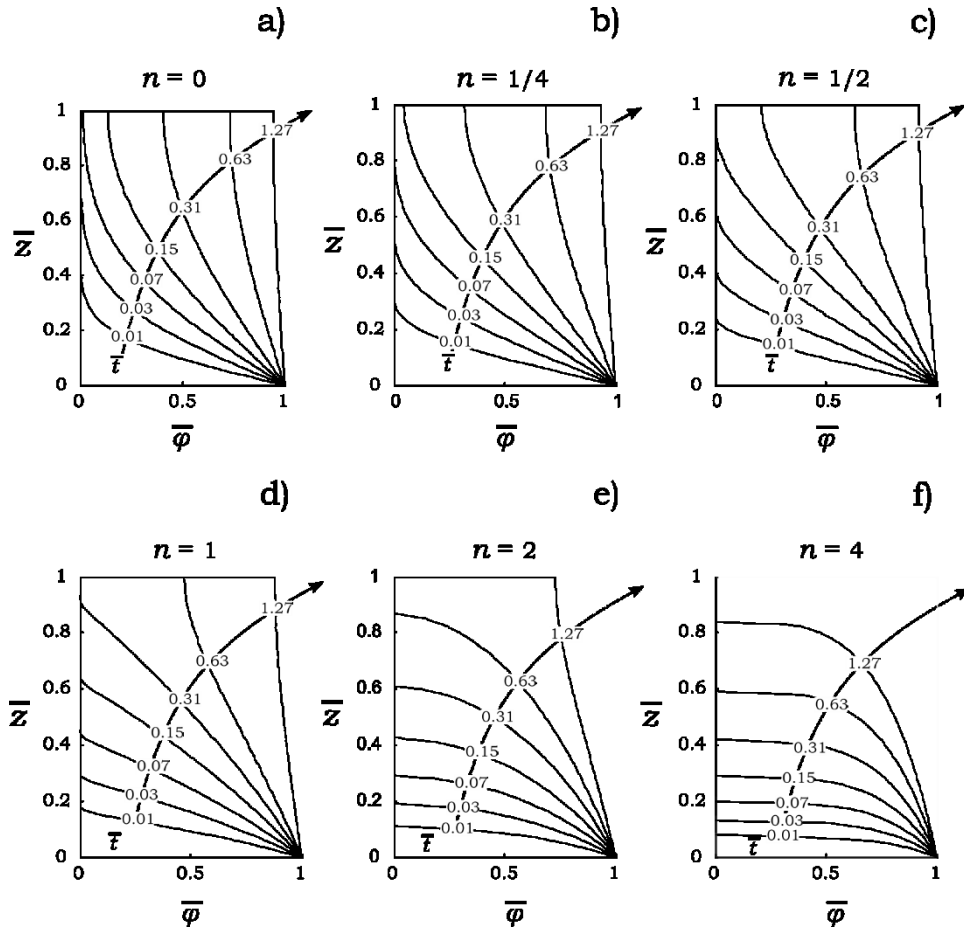


Figure 4.5 Water content distribution along  $\bar{z}$  assuming nonlinear imbibition using a)  $n = 0$ , b)  $n = 1/4$ , c)  $n = 1/2$ , d)  $n = 1$ , e)  $n = 2$  and f)  $n = 4$  for different values of  $\bar{t}$ .

### 4.3 Material nonlinearities

In order to further study the typical bending response of paper-based beams, the nonlinearities related to the three phenomena involved in the problem are individually analyzed in this section. The effects of such influences are analyzed using both bending and total strain distribution. The first provides an easy way to study the geometry of the induced

bending state, whereas the former offers information regarding the internal strain state of the material.

### 4.3.1 Imbibition

In the case of nonlinear imbibition the exponent  $n$  (refer to Table 4.1), which is related to the nonlinear water diffusivity, dictates the behavior of the imbibition. Two major influences of  $n$  on the dynamic imbibition can be appreciated in Fig. 4.5. First, it can be seen that the speed of the imbibition is reduced as  $n$  increases. Hence, the time response of the bending state is extremely dependent on the value of  $n$ . For instance, when  $n=0$  the homogenous distribution of the moisture is practically achieved at  $\bar{t}=1.27$  (see Fig. 4.5a). In contrast, at the same time the uptake of moisture is around 70% when  $n=4$ . Second, it can be noted that the shape of the moisture profile is also severely influenced by  $n$ . It can be seen that the moisture profiles change from convex (Fig. 4.5a) to concave (Fig. 4.5f) when increasing  $n$ . Therefore, it appears that the nonlinear imbibition has a strong effect on both the moisture speed of propagation within the paper-based beam and the shape of the moisture profile.

It is expected that any material may be characterized by a specific value of  $n$ . Hence, the influence of the nonlinear imbibition on the bending response can be analyzed in both time domain and the bending state cycle. However, the time response of the problem is also influenced by the moisture diffusivity constant of the material ( $D_0$ ). Thus, an analysis of the time response does not provide a clear means to compare the nonlinear

imbibition influences. In this regard, the bending state plot is most suitable to examine the response during the bending cycle.

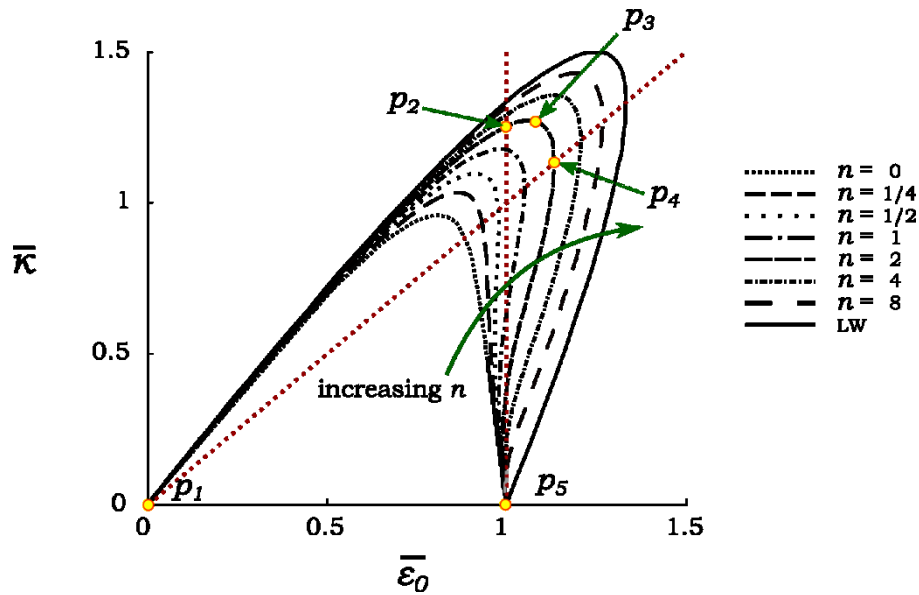


Figure 4.6 Influence of the nonlinear imbibition on the hydro-mechanical bending strain state cycle.

As previously discussed in chapter 3 the bending state plot only provides a general overview of the geometry imposed by the combination of both hygroexpansive and the total strain. The bending state cycle corresponding to the nonlinear imbibition cases illustrated in Fig. 4.5 are presented in Fig. 4.6. It can be seen that the initial bending state during raising ( $\bar{\epsilon}_0 < 0.5$ ) remains unaffected to the nonlinear imbibition. After this region, both curvature and bending strain reference are magnified as  $n$  increases. It should be noted that as  $n$  tends to high values the bending state response approaches the LW solution. In other words, using Richards's theory is it possible to predict the same bending states as those

found using molecular diffusion and capillary theory using  $n=0$  and  $n\rightarrow\infty$ , respectively.

Moreover, it can be noted that there is a threshold at which the reference bending strain is higher than the hygroexpansive strain actuation. This point is illustrated as  $p_2$  in Fig. 4.6 for  $n = 2$ . This threshold is only presented for  $n > 0.65$  according to the numerical results. Fig. 4.6 shows that the maximum curvature is magnified from 0.965 to 1.5 as  $n$  increases. Thus, it appears that the nonlinear imbibition plays an important role in the maximum bending energy that can be stored in the beam, which is proportional to the square of the bending curvature [146].

A further analysis of the nonlinear imbibition influence on the hygro-mechanical bending response may be performed by studying the internal strain state of the beam. However, it should be mentioned that the measurement of the total strain distribution represents a technical challenge compared to the assessment of the bending strain state. The distribution of the total strain for the case of the nonlinear imbibition is presented in Fig. 4.7. It is evident that these plots provide more information about the nonlinear effect compared to the bending state.

The results suggest that the nonlinear imbibition plays a major role in the total strain distribution in both raising and decay zone. For the case of linear imbibition (Fig. 4.7a), the paper beam experiences a compression-tension-compression (CTC) state along the axis  $z$  during the whole bending cycle. This state is formed by the contours lines ( $\varepsilon = 0$ ). It can be seen that the nonlinear imbibition has a strong influence on these contours. Fig.

4.7a-c have only two neutral points, which do not experiences neither compression nor tension. However, as  $n$  increases a state with three neutral points is induced, see Fig. 4.7d-f. This yields either a CTCT or a TCTC state.

In addition, the results suggest that the nonlinear imbibition also contributes to an amplification of the maximum total strain during bending cycle. The maximum total strain increases from 0.1925 to 0.3935 when increasing  $n$  from 0 to 2. That means that when  $n = 2$  the maximum total strain during the bending cycle is amplified almost twice compared to the case of the linear imbibition. For  $n > 16$  the maximum total strain is more than 0.98. This implies that when having high values of  $n$  the maximum total strain tends to be equal to the hygroexpansive strain actuation, which is in agreement with the case governed by the LW theory. This amplification of the total strain yields to an increment of the internal strain energy, which explains the magnification of the maximum curvature in the bending state plot (Fig.4.6).

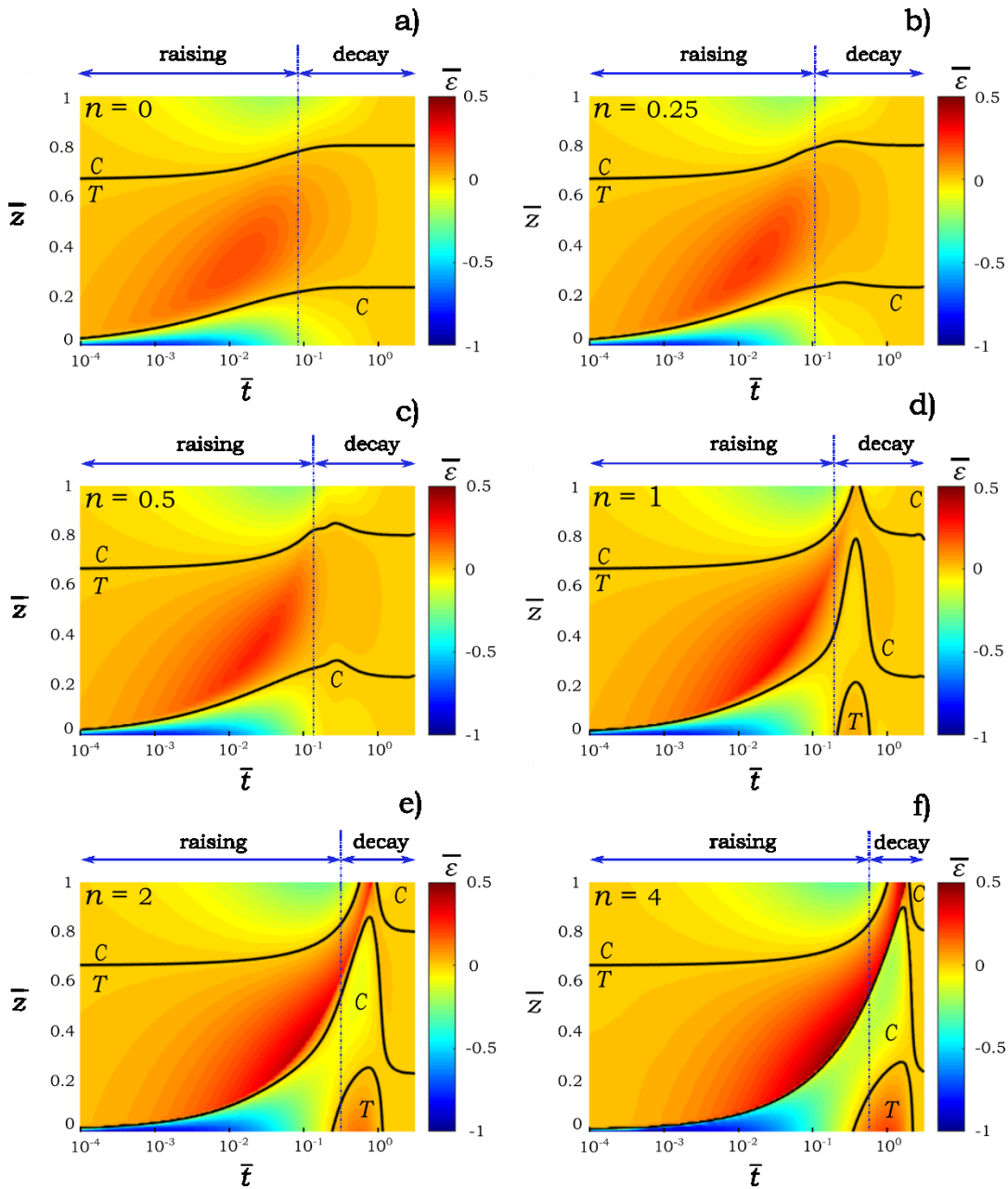


Figure 4.7 Total strain distribution along  $\bar{z}$  as a function of  $\bar{t}$  for the case of nonlinear imbibition. The nonlinear effect is studied by means of the exponent a)  $n=0$ , b)  $n=0.25$ , c)  $n=0.5$ , d)  $n=1$ , e)  $n=2$ , and f)  $n=4$ . Black lines represent contours at  $\varepsilon = 0$ . Zones T and C stand for regions experiencing tension and compression, respectively.

### 4.3.2 Softening effect

The relaxation of the Young modulus of elasticity is expected to have a contribution to the characteristic bending response. Such contribution can be studied by varying  $m$ , which is the Young modulus ratio between of wet and dry paper, see Table 4.1. This ratio provides similar information as in the case of the Timoshenko's bilayer theory [153]. It is well known that conventional metallic bilayer systems have usually ratios no more than one order of magnitude, and its influence on the bending response is minor. However, other bilayer systems such as silicon/PDMS have ratios up to five orders of magnitude; then, the effect of  $m$  becomes more important. In the case of wet against the dry paper, Young modulus ratios of two orders of magnitude have been reported in the literature [60]. In this section, the relaxation effects considering values of  $m$  up to three order of magnitude are analyzed.

The bending state corresponding to the nonlinear softening effect for the case of linear imbibition is presented in Fig. 4.8. The results suggest that the softening effect has a specific contribution to the bending state diagram. It can be seen in Fig. 4.8 that the softening effect on the linear imbibition case has a strong effect on the raising zone of the bending state plot. A reduction of the slope in the raising zone is induced by the softening effect as can be noted in Fig 4.8. However, the relaxation has an almost imperceptible impact on the decay zone.

In addition, one main difference of the softening effect on both LW theory and linear imbibing is the effect on the maximum curvature. The maximum curvature in the case of the LW case only experiences one shift on the strain reference, but it always has a maximum value of 1.5. However, for the case of the linear imbibition the maximum curvature is reduced by 14% when decreasing  $m$  two orders of magnitude. This value remains practically invariant if  $m$  is further increased as can be seen in the inset presented in Fig. 4.8. It should be mentioned that the effect of the weight is not taken into consideration in this formulation. Here, it is expected that the effect of the weight would become significant for high values of  $m$ . Hence, the whole bending state diagram may be different from that presented in Fig. 4.8.

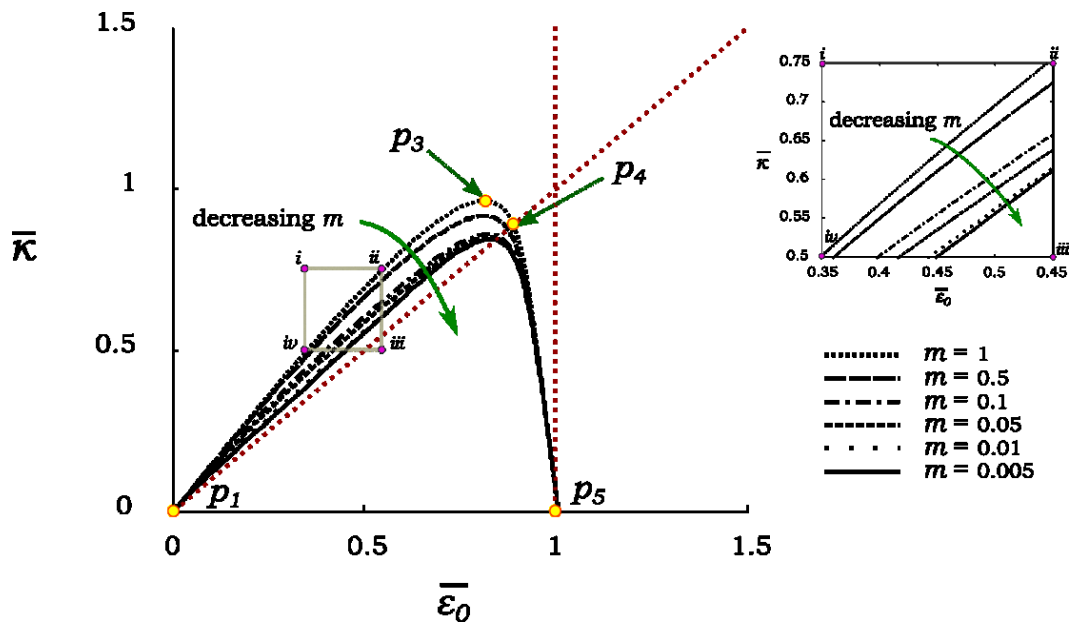


Figure 4.8 Influence of the nonlinear softening effect on the hygro-mechanical bending state cycle. Right-hand side image represents the magnification of the insert  $i-iv$ .

The total strain distribution for the case of the nonlinear softening effect is presented in Fig. 4.9. It is evident that the nonlinear softening effect has a moderate influence on the neutral axis of the total strain when the Young modulus of elasticity of wet paper is half of that corresponding to dry paper ( $m=1$ ). However, when further reducing  $m$  the shape of the contours ( $\varepsilon=0$ ) is substantially modified, see Fig. 4.9c-f. Despite this effect, the nonlinear softening effect does not induce any modification of the total strain state. Moreover, the total strain distribution has the same CTC state during the bending cycle for all the cases presented in Fig. 4.9a-f. It can also be seen that the maximum curvature experiences a minor shift on time compared to the effect of the nonlinear imbibition.

Furthermore, the nonlinear softening effect has a major influence on the distribution of the total strain in the rising zone. This effect is consistent with the bending state plot in Fig. 4.8. It can be seen in Fig. 4.9c-f that the distribution of the total strain in the compression zone near to the reference level ( $\bar{z} = 0$ ) is substantially amplified. In contrast, the gradient density of the total strain on the other two regions is reduced. This can be illustrated with the maximum values of the total strain in these zones when reducing  $m$  two orders of magnitude corresponding to Fig 4.9e. Such a reduction has been reported for filter paper in [60]. In this case, the maximum total strain in the tension zone is reduced 44.9%; whereas, the maximum negative total strain in the top compression zone is decreased 46.0% compared to the case in which  $m = 1$ .

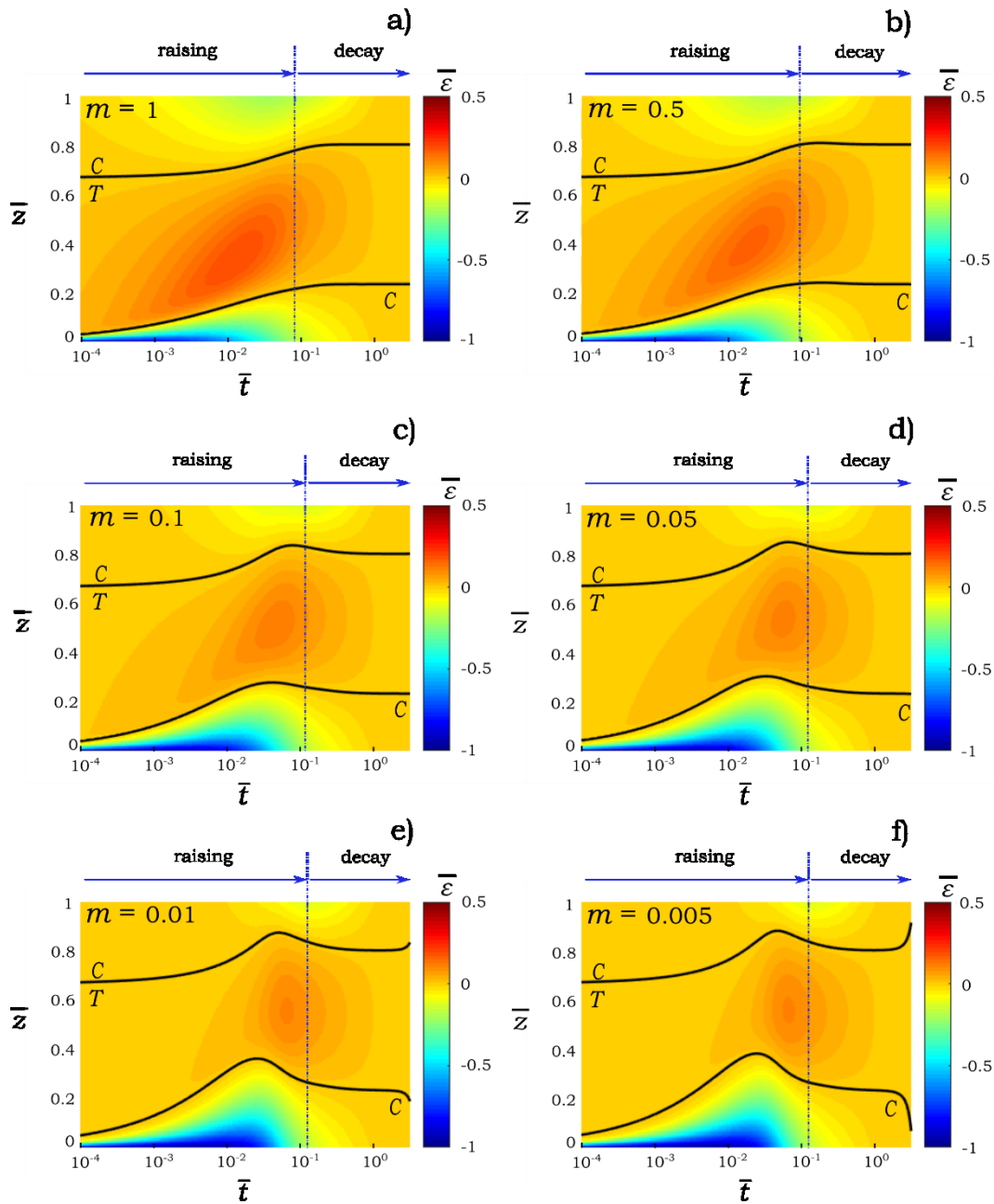


Figure 4.9 Total strain distribution along  $\bar{z}$  as a function of  $\bar{t}$  under the influence of nonlinear softening. The nonlinear effect is studied by means of a)  $m=0$ , b)  $m=0.5$ , c)  $m=0.1$ , d)  $m=0.05$ , e)  $m=0.001$ , and f)  $m=0.005$ . The contours at  $\varepsilon=0$  are represented as black lines. Zones T and C stand for regions experiencing tension and compression, respectively.

### 4.3.3 Hygroexpansive strain

Nonlinear swelling behavior paper is the most difficult to address nonlinearities to study in this investigation. Compared to the other nonlinear influences, nonlinear theories regarding swelling of paper as a function of the volumetric water content have not been developed yet. For this reason swelling is often modeled as a linear phenomenon when dealing with hygroexpansive strain actuation [57-59]. As previously discussed in chapter 3 other different scenarios could be studied by using a hypothetical nonlinear hygroexpansive strain actuation. Further, a function  $f_3$  (see Table 4.1) is applied to study such two possible scenarios: faster and slower swelling response to moisture content. Such cases can be represented using the exponent  $p$ . Here,  $p < 1$ ,  $p=1$ ,  $p > 1$  stand for the faster, linear and slower swelling of paper, respectively.

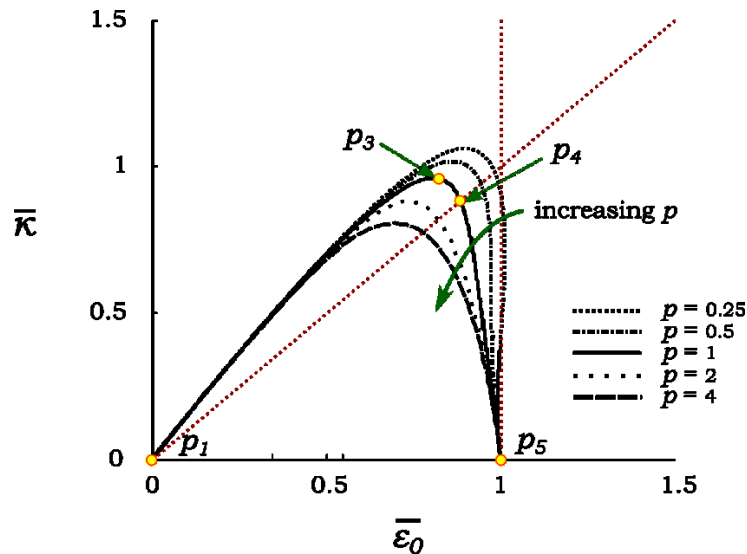


Figure 4.10 Influence of the nonlinear swelling on the hygro-mechanical bending state cycle.

The effect of the nonlinear swelling on the bending state cycle corresponding to the case of linear imbibition is presented in Fig. 4.10. It can be assumed that the nonlinear swelling has a strong effect on the maximum curvature of the bending strain state. It appears that fast swelling yields to an increment of 5.9% on the maximum curvature with respect to the maximum curvature of the linear swelling ( $p=1$ ) when  $p = 0.25$ . In contrast, the results suggest that slow swelling induces a reduction of the maximum curvature of 8.2% when  $p = 2$ . It can also be seen in Fig. 4.10 that the nonlinear swelling effect modifies the slope of the decay zone. In contrast, the slope of the raising region appears to remain unaffected by the nonlinear swelling. This effect implies that the nonlinear swelling only influences the shape of the bending curvature response near to the maximum curvature and the decay zone.

The nonlinear swelling effect on the total strain distribution is presented in Fig. 4.11. The results suggest that a fast swelling yields to a modification of both neutral axis and strain distribution similar to the case of nonlinear imbibition, see Fig. 4.11a-b. When reducing  $p$  the shape of the contours ( $\varepsilon = 0$ ) induces a TCTC state after the maximum curvature occurs as can be seen in Fig. 4.11a. In contrast, it is suggested that a slow swelling ( $p > 1$ ) only induced a slight modification of the strain distribution similar to the case of nonlinear softening effect, see Fig 4.11d-e.

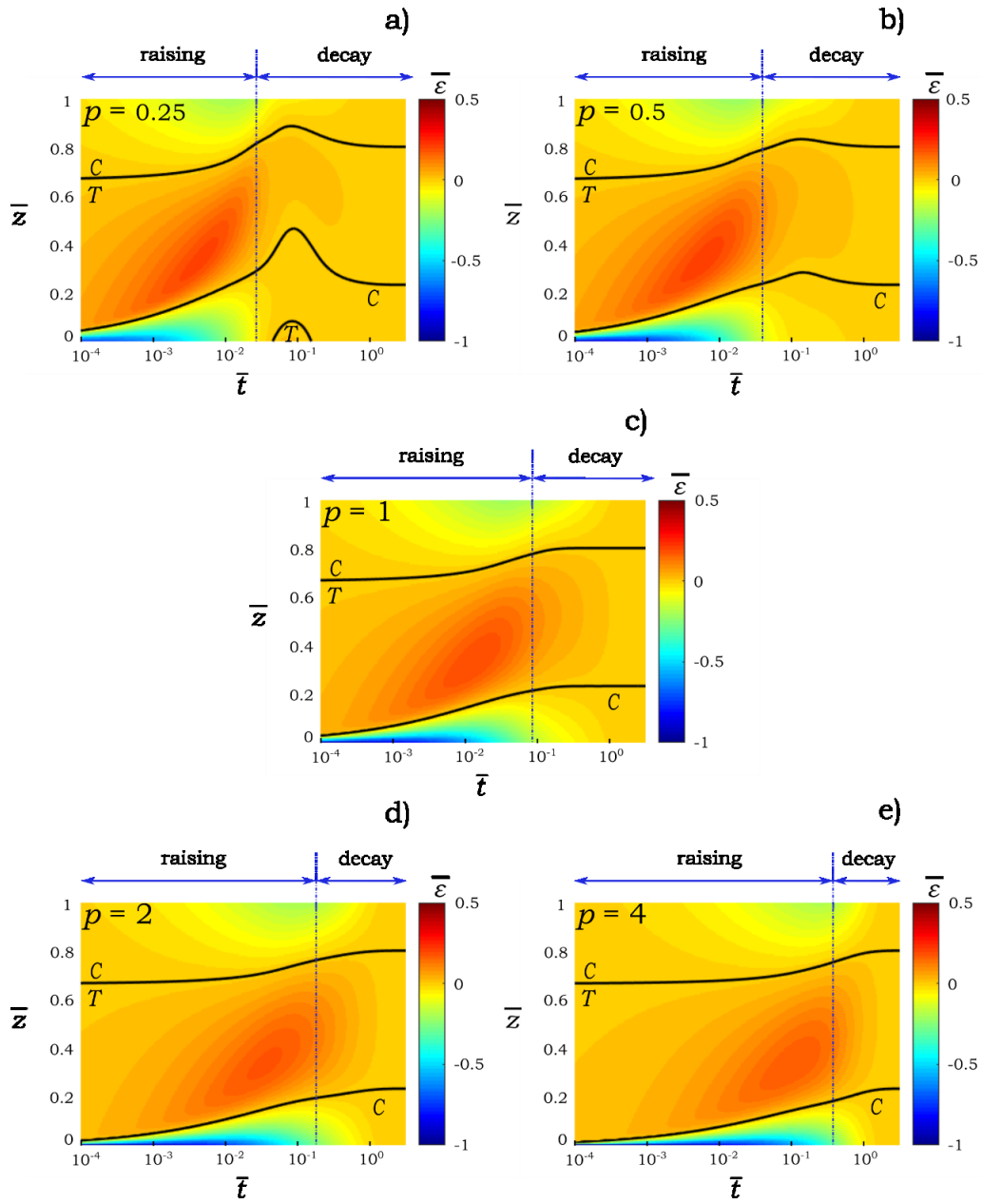


Figure 4.11 Total strain distribution along  $\bar{z}$  as a function of  $\bar{t}$  under the influence of nonlinear swelling. The nonlinear effect is studied by means of the exponent a)  $p=0.25$ , b)  $p=0.5$ , c)  $p=1$ , d)  $p=2$ , and e)  $p=4$ . The contours at  $\varepsilon = 0$  are represented as black lines. Zones T and C stand for regions experiencing tension and compression, respectively.

As it was expected the time at which the maximum curvature occurs is shifted backward and forward, for the case of fast and slow swelling response, respectively. Compared to the two previous cases, nonlinear swelling does not have a major effect on the maximum total strain. For the case of fast swelling response the maximum strain is amplified 8.2% compared to the linear response ( $p = 1$ ) when  $p = 0.25$ , while, a reduction of 13.1% occurs when  $p = 4$ . These results are consistent with the magnification and reduction of the maximum curvature in the bending state plot presented in Fig. 4.10.

#### 4.4 Characterization of the bending response

The bending curvature response of the hygro-mechanical bending response can be represented by a set of five parameters:  $\tau$ ,  $\eta$ ,  $n$ ,  $m$  and  $p$ . The first two define the time and the amplification scales. Their dimensions are [s] and [mm<sup>-1</sup>], respectively. The last other three parameters, which are dimensionless, determine the bending state cycle and the total strain distribution of the paper-based beam. The dependence of the physical phenomena occurring in the problem on these five parameters is summarized in Table 4.3. This table provides a simple means to predict the effect of one of the physical parameters on the curvature response.

It can be seen in Table 4.4 that the imbibition has a strong influence not only on the characteristic bending response but also on the time and

amplification scales. For instance, by changing the thickness of the paper beam the response yields to the same bending cycle but different amplitude and time scales, which is consistent with the experimental observations in [59]. Such behavior is due to the fact that parameters that are influenced by the thickness  $h$  are only the amplification gain and the time constant, while the parameters  $n$ ,  $m$  and  $p$  remaining invariant to  $h$ . Swelling, as an actuation strain source, has a significant influence on the amplification curvature scale but no impact on the time scale of the problem. Finally, the relaxation constant only influences the bending state cycle as well as total strain distribution; but without any effect on neither time nor curvature amplification scales.

Table 4.4 Dependence of the five necessary parameters to describe the hygro-mechanical response of paper-based beams.

Phenomenon	$\tau$	$\eta$	$n$	$m$	$p$
Imbibition	✓	✓	✓		
Softening				✓	
Swelling		✓			✓

The proposed model brings a practical means to characterize the bending curvature of paper-based beams. The curvature amplification can be determined by measuring the maximum hygroexpansive strain actuation and the thickness of the beam. Both parameters can be easily obtained using different techniques such as optical methods. In the same

way, the ratio between the wet and dry Young modulus of elasticity ( $m$ ) can be determined by performing tensile tests such as those conducted described in [60]. In contrast, the other three parameters are harder to be estimated due to the lack of experimental methods regarding both imbibition and swelling. However, these parameters can be estimated by minimizing the error with respect to the experimental results.

#### 4.4.1 Experimental validation

In order to validate the performance of the proposed model the characterization of the hygro-mechanical bending of a paper based beam studied in [59] is presented. Consider swelling behavior as linear ( $p = 1$ ); it is only necessary to determine the four remaining parameters to characterize the curvature. The amplification curvature can be evaluated by using the experimental values provided by the authors in [59] for both the maximum hygroexpansive strain (0.06-0.1) and the thickness of the beam (91  $\mu\text{m}$ ). A good estimation of  $m$  can be adopted by the experimental results in [60]. Those experiments showed a reduction of two orders of magnitude of  $m$ . Thus,  $n$  and  $\tau$  can be obtained by minimizing the RMSE between the proposed model and the experimental results. Such evaluation was performed using the optimization toolbox of MatLab yielding to an RMSE of 0.009  $\text{mm}^{-1}$ . The five parameters that describe the bending response of the paper-based beam are provided in Table 4.5.

Table 4.5 Parameters used in the proposed model to describe the experimental results presented in [59].

Parameter	$p$	$m$	$n$	$\eta$	$\tau$
Value	1	$10^{-2}$	1.13	1.52 mm	99.34 s

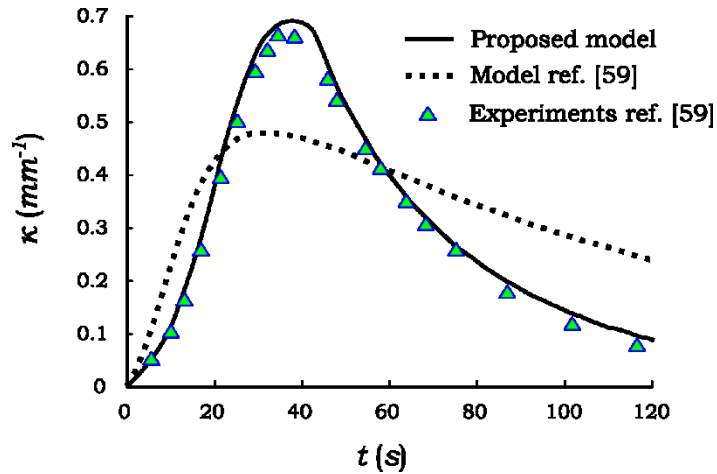


Figure 4.12 Comparison of the curvature response using the proposed model including nonlinear imbibition with experimental results presented in [59]. The RMSE for the proposed model is  $0.009 \text{ mm}^{-1}$ . In addition, the attempt to match the experimental result with the model developed in [59]. The RMSE for this attempt is  $0.120 \text{ mm}^{-1}$ .

The comparison of the proposed model and the experimental results in [59] is presented in Fig. 4.12. It can be seen that the proposed model considering the nonlinear imbibition, whose parameters are listed in Table 4.5, is in good agreement with experimental results. Similarly, an attempt to match the experimental data with the model governed by linear imbibition is also presented in Fig 4.12. The results suggest that the

accuracy of the proposed model lies in the physical assumptions of the nonlinear imbibition rather than the error minimization process. The root mean square error of the bending curvature corresponding to Table 4.3 is  $0.009 \text{ mm}^{-1}$ .

## 4.5 Summary

A better understanding of the problem is achieved by taking into consideration the nonlinear influences involved in the hygro-mechanical problem. Such influences were studied looking at both the bending state and the total strain distribution during the bending cycle. It was found that the nonlinear imbibition plays a crucial role in the bending response on both curvature and total strain distribution in the whole bending cycle. In contrast, it was found that the softening and swelling nonlinearities only influence a limited zone of the bending cycle. The softening effect has a major influence in the raising zone, while the nonlinear swelling effect is situated near to the maximum curvature and decay zone.

The proposed dimensionless novel formulation presented in chapter 3 provides a simple approach to characterize the hygro-mechanical bending response of paper-based beams. The curvature response can be described by means of five parameters. The proposed formulation was tested by characterizing the bending response of a paper-based beam presented in [59]. The results reveal a good agreement with experimental results reported in previous work.

## Chapter 5 Paper-based hygro-mechanical systems as sensing elements

*The hygro-mechanical response of paper has been studied only as a physical phenomenon. Thus, the main objective of this chapter consists of taking advantage of the hygro-mechanical response of paper to develop PB-HMS sensors for physical characterization of aqueous solutions. The feasibility to characterize these solutions by means of the dynamic bending response of paper is studied in this chapter. A new PB-HMS as a potential sensor is proposed. It is suggested that the characteristic bending response of the PB-HMS may provide crucial information about certain properties of the tested liquid. The proposed PB-HMS is formed using a cantilever-droplet design. The bending response of different PB-HMS using different aqueous solutions containing methanol, hydrogen peroxide, glycerol, and sucrose are experimentally tested. The experimental results show the sensitivity of the proposed PB-HMS by comparing the phase portrait (bending velocity against acceleration) of different liquids. It is expected that the final application of these PB-HMS may lead to the characterization of bio-fluids, the identification of hazardous liquids and the estimation of concentrations in aqueous solutions.*

## 5.1 PB-HMS design

Authors in [58, 59] focused on the theoretical study of the hygro-mechanical response of tracing paper due to its interaction with water. They provide an explanation of this phenomenon from a physical point of view. However, this phenomenon can be exploited to characterize different aqueous solutions that are of extremely importance in different areas. For instance, determination of alcohol or sugar content of commercial beverages in food industry. In addition, this phenomenon can also be applied to characterize bio-fluids as they are water based (i.e. urine, saliva, and blood). Another application may be the identification of forbidden liquids such as explosives at safety checkpoints. Hence, it is suggested that paper-based hygro-mechanical (PB-HMS) systems could be developed to perform these tasks. Based on the analysis performed in chapter 4 it is expected that the bending response of PB-HMS may be applied to characterize liquids. The design of the PB-HMS for characterization of liquids is presented in the following subsections. The design is divided into two stages: conceptual and physical.

### 5.1.1 Conceptual design

Characterization of liquids can be performed by measuring their physical or chemical properties. In this regard, optical properties of liquids have been applied to perform characterization of fluids. For instance, infrared (IR) and ultraviolet (UV) spectrometers measure the absorbance of

light to characterize one liquid. However, these spectrometers make use of very specialized hardware yielding to high-cost equipment. In another example, refractometers measure the refraction to evaluate the concentration of aqueous solutions such as sucrose content in beverages. The cost of this equipment is lower than the one of the spectrometers due to the simplified hardware. However, these tools can be applied to estimate the concentration of a known solution but cannot be implemented to perform identification of liquids. Thus, an interesting challenge is to develop a method to both characterize and identify liquids with a very low-cost of equipment.

It is suggested that the characterization of liquids can be conducted by means of the hygro-mechanical bending response. As previously discussed in Chapter 4 the bending state truly depends on the concurrent phenomena: imbibition, swelling and softening effects. Such phenomena are related to the physical and geometrical properties of the paper-based beam. The physical properties could be classified as those pertaining to both paper and liquid. Although it is difficult to assess the individual influence of each property, it is possible to characterize either paper or fluid using the bending response of PB-HMS. Liquid characterization can be performed by using the same type of paper and geometry while using different liquids.

Let us consider that a given type of paper with a specific thickness is applied to develop a PB-HMS. Here, it is evident that the only way to modify the dynamic bending response is by changing the properties of the

liquid. In other words, the sensitivity of the hygro-mechanical bending response will truly depend on the liquid. Therefore, the characterization of polar liquids can be performed by means of the characteristic bending response of the PB-HMS. It is expected that the beam-liquid interaction yields a unique response that may be applied to characterize the liquid. However, it is necessary to determine some features such as the beam-liquid configuration and readout that simplify the operation of the paper-based device. The rationale of these elements is presented in the following subsection.

### 5.1.2 Physical design

From a practical point of view, the beam-liquid interaction mechanism applied in [58, 59], positioning the paper-based beam on water, represents a major drawback as the measurement of the bending response requires sophisticated techniques due to the lack of alignment between the beam and the optical detector. In this regard, an alternative approach to form the PB-HMS is to deposit a small droplet of liquid on the surface of the beam [79]. In this case, a local variation of the water content that selectively modifies the moisture content in the paper-based beam is achieved (see Fig. 5.1). This type of moisture source provides an easy way to modify the moisture content by using a standard mechanical pipette.

Another key property that will affect the output of the system are the boundary conditions of the paper-based beam, which become crucial to reach a proper measurement of the bending response. In this case, a

cantilever beam configuration is set as it provides an easy way to align the beam with the optical detector while enabling a large deflection response. Such large deflection response allows easy measurement of the bending response. Fig. 5.1 shows the schematic representation of the proposed configuration of the paper-based sensing element. In this case, the droplet is positioned at the center of the beams length.

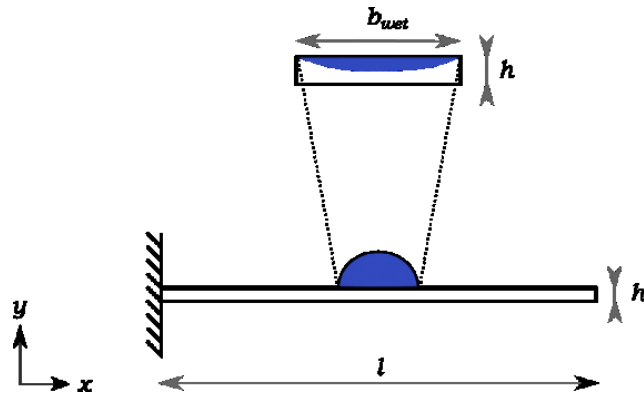


Figure 5.1 Proposed configuration of the PB-HMS. The sensing element is a paper-based cantilever beam of length  $l$  and thickness  $h$ . The bending response is triggered by a small droplet that wets a portion  $b_{wet}$  of the cantilever length.

An example of the proposed configuration is presented in Fig. 5.2. Here, the bending response of two paper-based microcantilever beams due to their interaction with a  $1.5 \mu\text{L}$  droplet of distilled water ( $1.5 \times 10^{-6} \text{ kg}$ ) is illustrated. One microcantilever beam was fabricated along the machine direction (MD) of tracing paper and the other one along its cross section (CD). It was previously found that the tracing paper on water swells up to 8% in CD, while it does only 1% in MD [58]. For more detail on the characterization of these directions on a rectangular sheet of paper please

refer to [144, 148]. After the droplet is deposited on the microcantilever surface, the CD microcantilever starts to swell non-homogeneously along the thickness producing a curvature in the local wet area. Then, a maximum curvature is reached at  $t \approx 70$ s. Although the droplet evaporates, the microcantilever beam can achieve a steady state curvature ( $t \approx 350$ s). In contrast, the MD microcantilever beam remains practically straight as the droplet evaporates suggesting that the weights of the droplet and beam do not have a substantial influence on the bending response of the CD microcantilever. Thus, it is suggested that the proposed PB-HMS offers a similar bending response as that analyzed in chapter 3 and 4.

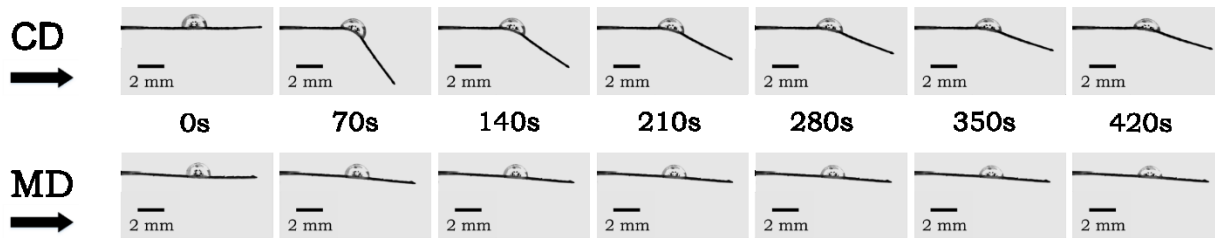


Figure 5.2 Time lapse side view of paper-based microcantilever beam experiencing hygro-expansion along both cross (CD) and machine (MD) direction.

## 5.2 Experimental section

In order to study the dynamic response of the PB-HMS two cantilever paper-based beams are fabricated (C1 and C2). The cantilever beam C1 is made of tracing paper (Carson® as used in [58, 59]) and the cantilever C2 is made of standard pad paper supplied by a local store. The cantilever

beams C1 are made using tracing paper as received, while the beams C2 are filled by soaking the paper with an acrylic resin. This treatment is performed to mimic the structure of tracing paper and to study the effect of particular fluid on the filled resin. The dimensions of the beams are presented in Table 5.1.

Table 5.1 Properties of cantilever beams C1 and C2.

Cantilever	Paper	Length (mm)	Width (mm)	Thickness ( $\mu\text{m}$ )	Treatment
C1	Tracing	15	1	91	Used as received
C2	Pad	15	1	30	Filled with acrylic resin

### 5.2.1 Cantilever beams fabrication

A set of cantilever beams (length=15mm, width=1mm) were fabricated. The fabrication procedure is extremely simple as it involves only one and two steps for the cases C1 and C2, respectively. The main step in both cases is the cutting process. This process was performed using a commercial electronic paper cutter (Silhouette Portrait®). This step process requires only a few minutes (<5min) in order to fabricate more than 100 microcantilever beams. Fig. 5.3 shows the fabrication process of a cantilever beam made of tracing paper. In the case of C2, the pad paper is previously filled with acrylic resin using a permanent marker ink.

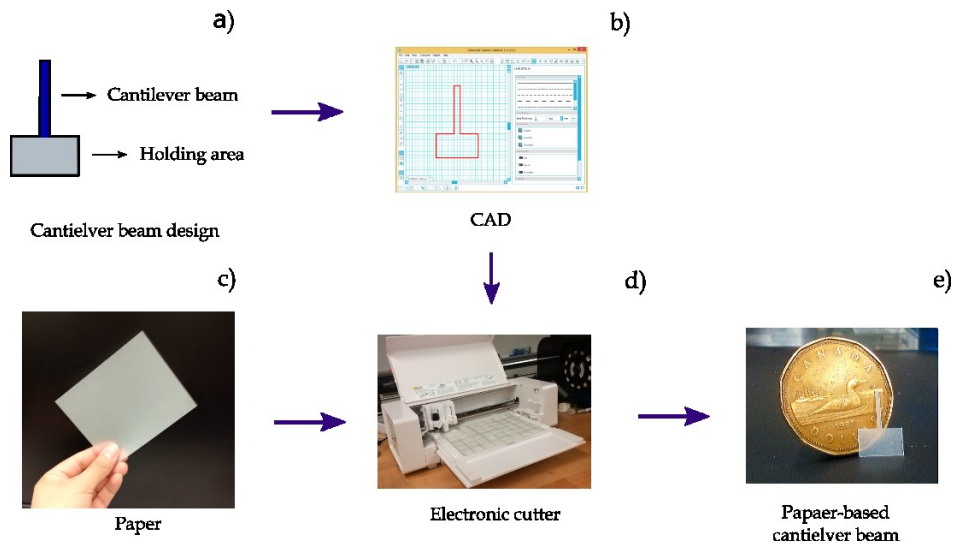


Figure 5.3 Fabrication process of the paper-based cantilever beams. a) A rectangular area is added to the cantilever beam for holding purposes. b) The design is implemented using CAD. c) The paper is placed on an electronic cutter. d) The paper-based elements are cut. f) A fabricated paper-based cantilever beam is compared to the size of a one Canadian dollar coin.

### 5.2.2 Experimental setup for measuring the dynamic response of the PB-HMS

All the experiments were carried out in a chamber at a room temperature at 24°C with a relative humidity of 50%. Figure 5.4a shows the experimental setup for the measurements carried out in this chapter. The paper-based cantilever beam is placed in a metallic holder as illustrated in Fig. 5.4b. Then, a digital microscope (Celestron®) is perpendicularly aligned to the cantilever holder to record the motion of the

cantilever beam (Fig. 5.4c). Finally, the water droplet is deposited on the cantilever surface by using a metered pipette (Figure 5.4d).

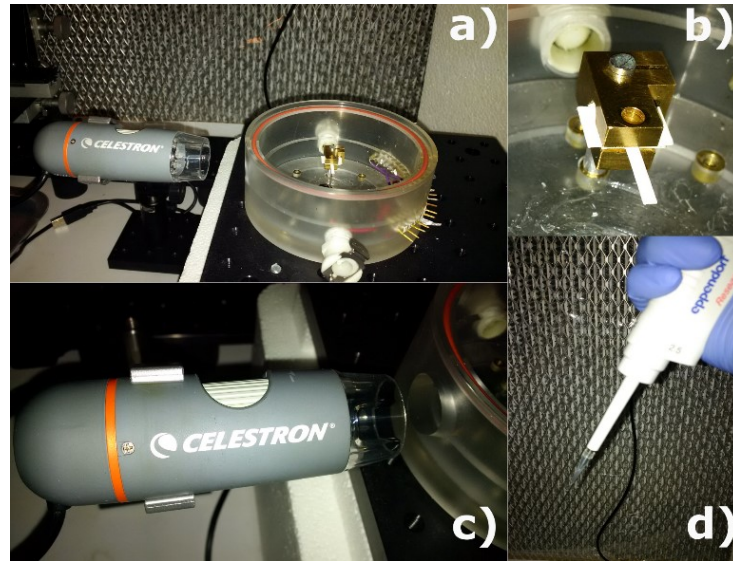


Figure 5.4 Measurements of the hygro-mechanical bending response. a) Experimental setup and b) a detail of the cantilever holder. c) The portable microscope and d) the mechanical pipette used to deposit the fluid droplet on the surface of the cantilever beam.

### 5.2.3 Read-out of the bending response

In order to extract the hygro-mechanical dynamic response of the system (droplet-cantilever), a sequence of images was acquired using the digital microscope (Fig. 5.4c). The portable digital microscope was chosen as the read-out of the bending response since they offer specific advantages. They are highly available in several versions and are highly portable as they are light weight. Here, it is important to mention that this setup can be only functional for those dynamic responses with low

frequency compared to the sampling rate of the microscope. The digital microscope has a maximum sampling rate of 30 frames per second (fps) at a resolution of 1280 x 960 pixels. The sampling recording rate selected for the case of C1 and C2 were 2 and 1 fps, respectively, with a resolution of 2048 x 1536 pixels.

#### 5.2.4 Image processing

The hygro-mechanical bending response of the paper-based cantilever beams was characterized by measuring the bending angle  $\Omega$ , which is proportional to the curvature of the wetted portion of the beam. Fig. 5.5 illustrates the steps involved in the image processing method to evaluate such a bending angle. The images were captured using a black background to facilitate the image process. The set of acquired images corresponding to one bending cycle is imported to ImageJ as a stack of pictures. In this case, all the operations in the image processing method are applied simultaneously to all images. These operations performed in the image processing method can be summarized as follows:

- i) The contrast of the images is enhanced to enable an easy detection of the cantilever beam.
- ii) The format of the image is transformed from grayscale to binary.
- iii) The clamp and the wetted area are subtracted from the images, such that two straight segments are clearly defined

- iv) The orientation of each segment is measured using the “Analyze particles” plugin of ImageJ.
- v) Finally, the bending angle is evaluated as the difference of the orientation of both segments.

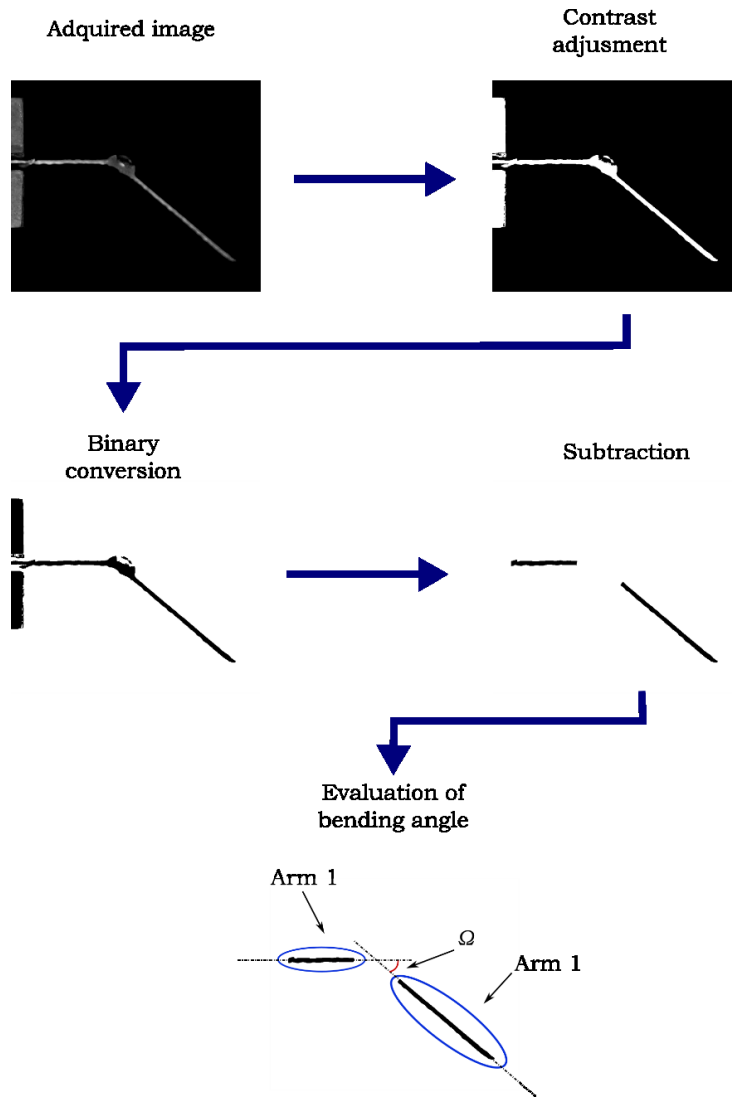


Figure 5.5 Image processing method to evaluate the bending angle of the paper-based cantilever beam using ImageJ.

### 5.3 Dynamic performance of the PB-HMS

The measured bending angle response of C1 and C2 due to their interaction with a 1.5  $\mu\text{L}$  droplet of distilled water is presented in Fig. 5.6a and 5.6b, respectively. The characteristic bending response of both cantilever beams are similar to that found in [59] and discussed in chapter 3 and 4 for the case of paper-based beams placed on water. However, it can be seen that the steady state bending angle does not come back to the initial straight configuration as reviewed in chapter 3 and 4. This effect may be due to the fact that the mass of both beam and droplet became significant for the proposed cantilever beam configuration. These loads would play a major role in the bending response as soon as the softening effect occurs. Both cantilever beams yield a similar bending angle response suggesting that this phenomenon is not exclusively presented in tracing paper.

It can be noted in Fig. 5.6a-b that the bending angle response of cantilever C1 has a slight deviation when performing several experiments ( $N=7$ ). In contrast, the response of the C2 has a significant deviation. Such effect is reasonable due to the fact that C2 is made of pad paper that has a less consistent quality than the tracing paper. In addition, the result may be influenced by the filling process. Although this deviation in the bending angle has been observed, it can be noted that the characteristic shape of the response appears to be unaffected. This effect suggested that such a deviation is dominated by the maximum hygroexpansive strain actuation,

which only modifies the amplitude of the response without affecting the shape of the bending state.

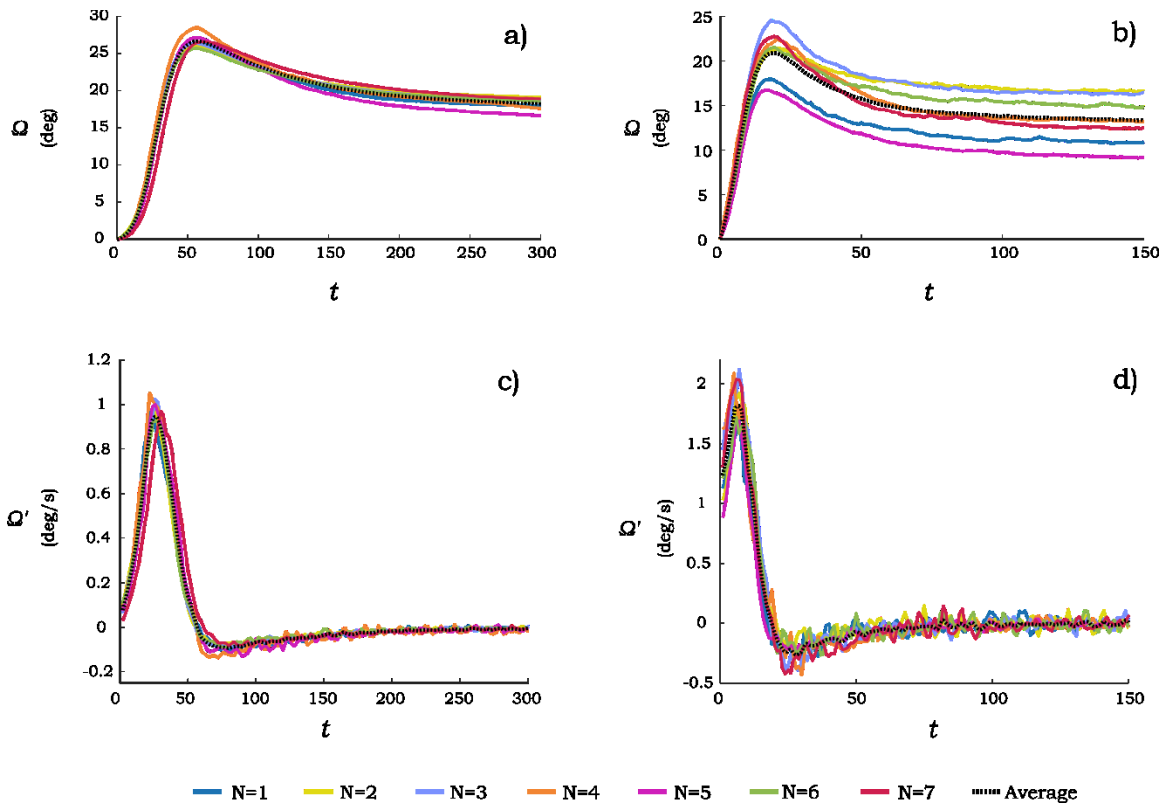


Figure 5.6 Dynamic response of paper-based cantilever beams C1 and C2. Bending angle response of a) C1 and b) C2. c) and d) represent their first derivative with respect to time. Time sample recording is 2s and 1s for C1 and C2, respectively. In each case the number of experiments carried out was  $N=7$ .

To further study the dynamic response of the paper-based cantilever beams the first derivative of the bending angle with respect to the time, namely bending velocity, is presented in Fig. 5.6c-d. These velocities were

estimated from the bending angles measurements using the centered differentiation numerical method. It can be noted that such bending velocities can be described as a single oscillation of a very slow dynamic system. It can be seen in Fig. 5.6d that the bending velocity that the significant deviation presented in the bending angle is compensated. Hence, it can be concluded that the deviation presented in Fig. 5.6b is mainly produced by the amplification effect of the hygroexpansive strain actuation rather than effects associated with either imbibition or softening effect. Thus, it is suggested that to avoid deviations due to a variation on the hygroexpansive strain actuation, the bending velocity would represent a better choice to characterize the dynamic response of the paper-based beams.

Moreover, the response of C2 is almost twice faster than the one of the C1, which is consistent with the analyses performed in chapter 4. Since the thickness of C2 is smaller than that of C1, the imbibition speed increases. This increment on the time response induces a proliferation of the noise on the bending response. The propagation of the noise in the response of C2 is slightly appreciated in Fig 5.6b, and more evident in Fig 5.6d. Thus, it can be seen that the bending response behaves as any other dynamic system but at a very low frequency. Thus the main idea of the proposed sensing principle is to extract information of liquids by means of the dynamic features of such similar system. However, rather than using harmonic excitations at high frequencies (~kHz) as conventional dynamic microcantilever sensors, the novelty of this sensor lies in the fact that only

one single response at very low frequency ( $\sim$ mHz) is needed to assess the measurement.

### 5.3.1 Liquid sensitivity

Another important aspect to be considered is the sensitivity of the paper-based cantilever beam to different liquids. The feasibility of developing PB-HMS sensors depends on their response to different liquids. In this regard, the dynamic response of C1 and C2 due to their interaction with distilled water, water-methanol, and water-hydrogen peroxide are presented in Fig 5.7 and 5.8. The binary solutions were prepared at a concentration of 20% (v/v) such that the water content in both solutions remains constant. The second derivative of the bending angle is also presented in Fig 5.7 and 5.8 as they provide an extended means to evaluate the dynamics response. In Fig. 5.7 it can be seen that C1 is sensitive to the presence of methanol and hydrogen peroxide at the given concentration. The analysis of the response of both binary solutions can be performed by taking as reference the response of pure water, see Fig. 5.7a-b.

On one hand, the dynamic responses of methanol solution appear to experience a delay in the time response as can be seen in Fig 5.7c. This effect is more evident if one looks at the bending acceleration in Fig. 5.7d. Here it can be seen that the time duration of the bending acceleration is longer compared to that of the water response. According to the analysis performed in chapter 4, it is suggested that this effect on the time scale is

mainly dominated by imbibition. It is also remarkable that the amplitude of the acceleration is significantly reduced compared to the case of pure water. In this case, the reduction of the acceleration may be due to the other phenomena including softening and swelling.

On the other hand, the effect on the time response of the hydrogen peroxide solution when comparing with water appears to be minor. It can be seen that the time duration of the bending acceleration is similar to both water (Fig. 5.7b) and water-hydrogen peroxide solution (Fig. 5.7d). That means that the imbibition rate is only partially influenced by the addition of hydrogen peroxide. Moreover, the maximum amplitude of the bending velocity (Fig. 5.4b) for this case is higher compared to that of water. In addition, hydrogen peroxide appears to induce an increment on the negative peak of the acceleration from  $-0.045 \text{ deg/s}^2$  to  $-0.066 \text{ deg/s}^2$  when increasing the concentration of hydrogen peroxide from 0% to 20%. Therefore, it is suggested that the cantilever beam C1 is sensitive to other liquids. The effect of the liquid on the paper-based cantilever beam can be associated with the time response and amplitude of both signals bending angle and velocity.

The dynamic response of the cantilever C2 due to its interaction with water, water-methanol and water-hydrogen peroxide is presented in Fig. 5.8. It can be noted that the bending acceleration (Fig 5.8a-b) produced by water is similar to that corresponding to C1. Hence, it is suggested that the filling process of C2 has not a significant influence on the characteristic bending response.

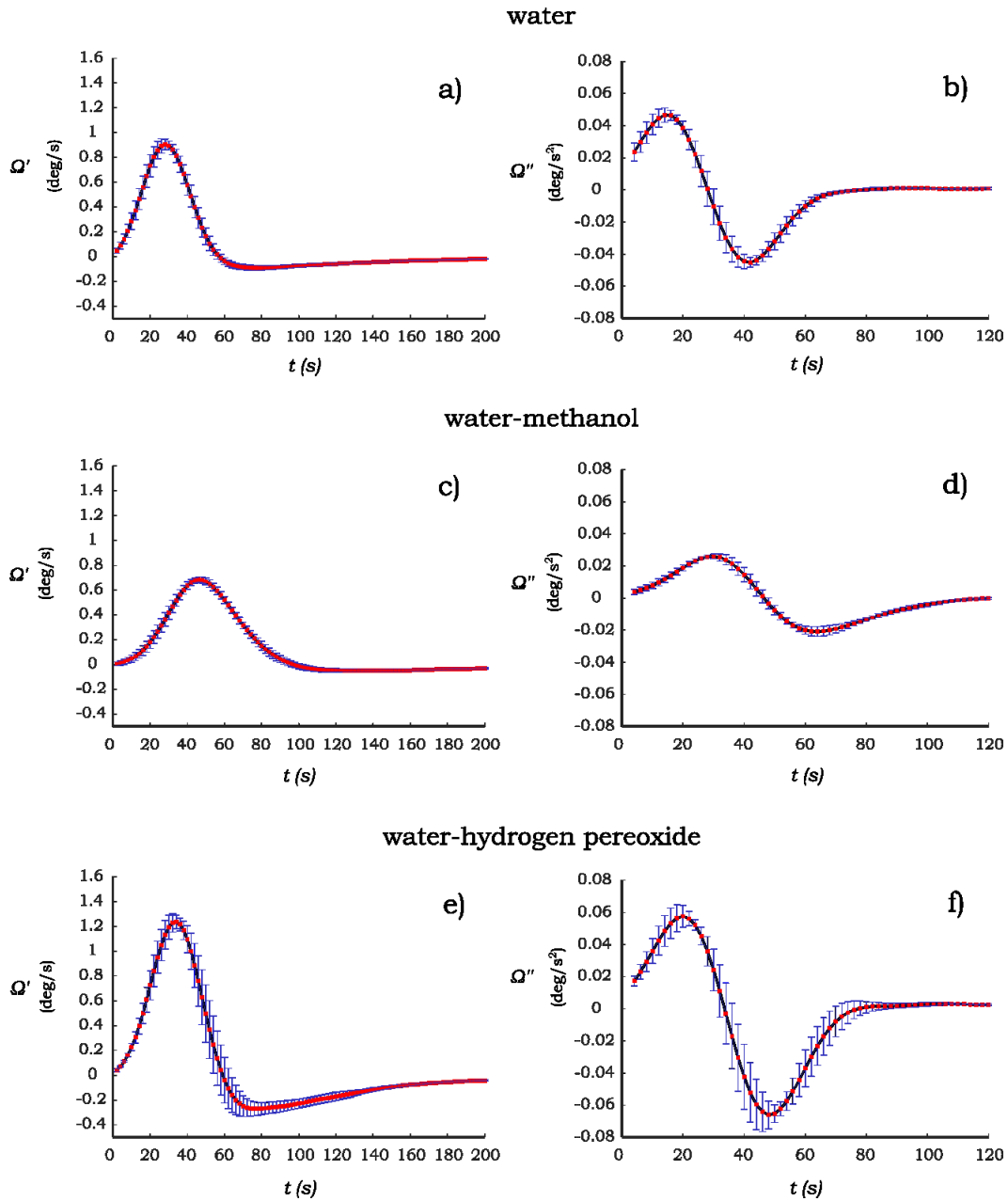


Figure 5.7 Dynamic response of paper-based cantilever beam C1 under the influence of a-b) water, c-d) water-methanol and e-f) water-hydrogen peroxide. The bending velocity ( $\Omega'$ ) is presented in the left column, while the bending acceleration ( $\Omega''$ ) on the right column. Time sample recording is 2s, and bars represent the standard deviation for  $N=7$ .

By adding methanol, the bending response (Fig. 5.8c-d) is modified in both time response and amplitude. This effect is notable in the bending acceleration of the water-methanol solution. As in the case of C1, the peaks of maximum and minimum acceleration (Fig. 5.8d) are reduced almost to half of those corresponding to water (Fig. 5.8b). This implies that the three hygro-mechanical response of water-methanol has similar behavior for both types of cantilever beams C1 and C2.

It can be seen that the response of C2 (Fig 5.8e-f) to the water-hydrogen peroxide solution is different from the one found using C1 (Fig. 5.8e-f). This discrepancy can be assessed when comparing the bending acceleration of the water-hydrogen peroxide solution with that of the water. Here, the bending acceleration has a reduction of the amplitude and a significant increment on the time response compared to pure water. While the bending acceleration of water (Fig. 5.8b) at the 30s is practically equal to zero, the one corresponding to water-hydrogen peroxide (Fig. 5.8f) is  $\sim -0.05 \text{ deg/s}^2$ . In contrast, the time response of both water and water-hydrogen peroxide are similar when using C1. This results may be related to the softening effect since hydrogen peroxide is chemically active and may degrade the acrylic resin filler in C2. Thus, it is suggested that the hygro-mechanical bending response of the paper-based beams is sensitive to aqueous solutions.

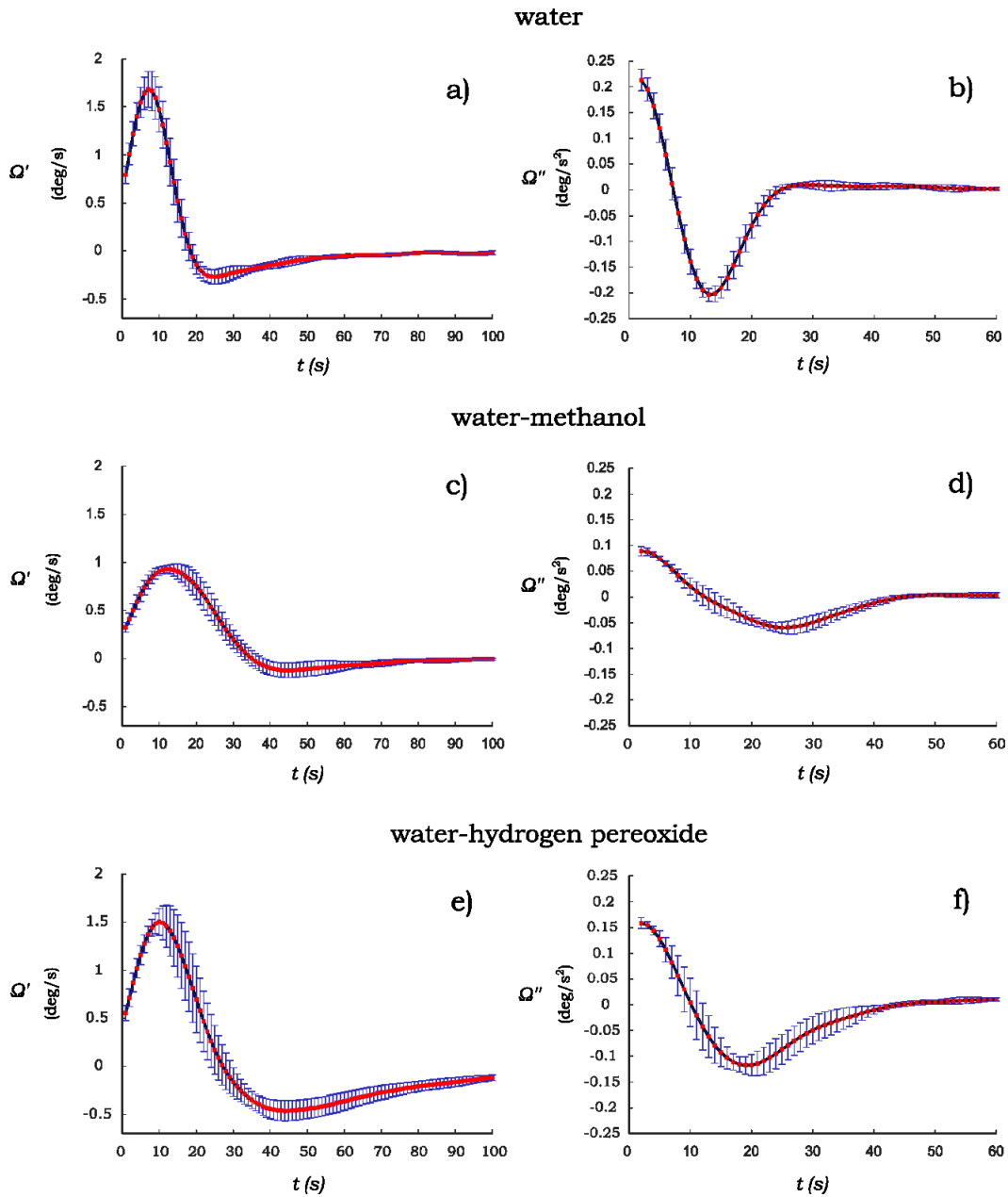


Figure 5.8 Dynamic response of paper-based cantilever beam C2 under the influence of a-b) water, c-d) water-methanol and e-f) water-hydrogen peroxide. The bending velocity ( $\Omega'$ ) is presented in the left column, while the bending acceleration ( $\Omega''$ ) on the right column. Time sample recording is 1s, and bars represent the standard deviation for  $N=7$ .

## 5.4 Portrait signature of PB-HMS

As any other dynamic system, an alternative approach to assessing one influence is to look at the phase portrait. Hence, it is suggested that the evaluation of the effect of any liquid in one aqueous solution may be synthesized in one phase portrait of the bending velocity and acceleration presented in Fig 5.7 and 5.8. These portraits may provide valuable information regarding the content of the binary solution. Fig. 5.9-5.13 show the phase portrait of the bending response of the cantilever beams C1 and C2 under the interaction of distilled water, water-methanol, water-hydrogen peroxide, water-glycerol, and water-sucrose.

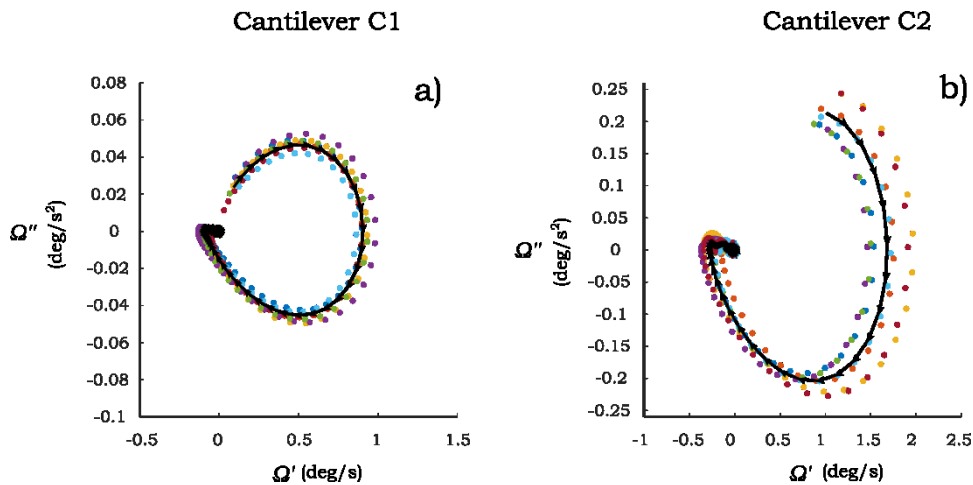


Figure 5.9 Phase portrait of the dynamic response of the cantilever beams a) C1 and b) C2 under the influence of water. The black line represents the phase portrait of the average response. Color points represent experimental measurements using  $N=7$ . Sample recording is 2s and 1s for C1 and C2, respectively.

The phase portraits of water (see Fig. 5.9) reveal that the dynamic bending response can be described as a single oscillation of a stable dynamic system. It is important to establish that as the bending velocity and acceleration were estimated numerically, the portrait charts begin in 2s and 4s for C1 and C2, respectively. Both phase portraits (C1 and C2) exhibit similar shape as expected from the time responses in Fig. 5.7 and 5.8. Hence, the presence of other liquid in a binary solution may be studied by comparing its phase portrait to the one corresponding to pure water. The phase portraits of four different binary aqueous solutions are presented in the following subsections. The components of such solutions are methanol, hydrogen peroxide, glycerol, and sucrose. The first three concentrations were made at 20% (v/v) and the former at 60g/L.

#### 5.4.1 Methanol

The phase portraits of the water-methanol solution are presented in Fig. 5.10. It can be seen that the presence of methanol yields to phase portrait inside the one corresponding to water. This indicates that the velocity and acceleration of the response of methanol are slower compared to the response of water. The reduction of the amplitude of both bending velocity and acceleration is a result of the decrease in the imbibition rate. However, in both cases (C1 and C2) the shape of the portrait is very similar to the one of water. This implies that the combination of the swelling and softening effects of the water-methanol solution are similar to the effects of

pure water on both types of beams. In other words, methanol is not significantly altering either softening or swelling phenomena.

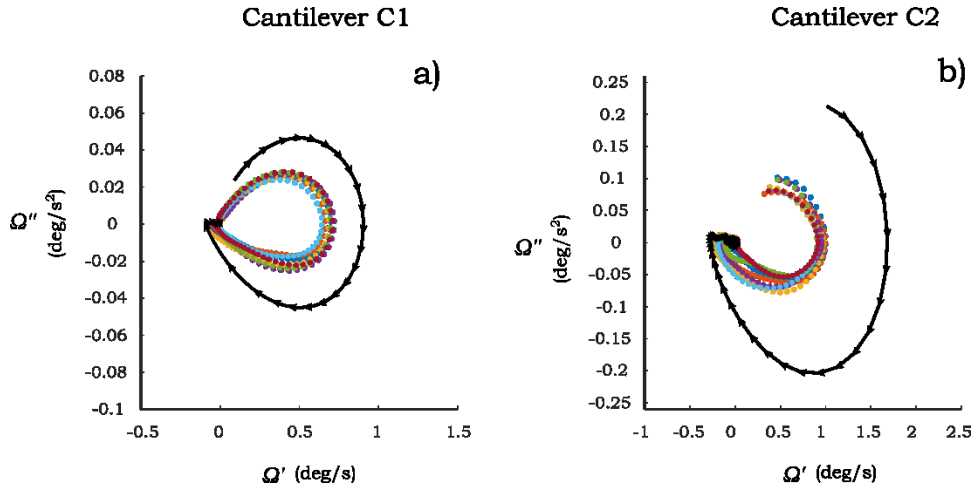


Figure 5.10 Phase portrait of the dynamic response of the cantilever beams a) C1 and b) C2 under the influence of water-methanol solution. The black line represents the phase portrait of the average response of water. Color points represent experimental measurements using  $N=7$ . Sample recording is 2s and 1s for C1 and C2, respectively.

#### 5.4.2 Hydrogen peroxide

Fig. 5.11 presents the phase portraits of the water-hydrogen peroxide solution. Hydrogen peroxide is known as an active chemical material that may react with different materials including living tissue. It is expected that its interaction with the paper-based beams may produce a different portrait shape. It can be seen in Fig. 5.11a that hydrogen peroxide produces a phase portrait outside the one corresponding to water for C1. In contrast, the phase portrait of C2 is inside the reference portrait

(water). Moreover, the shape of the portrait of C1 is very similar to the one of water forming concentric lines. In contrast, the portrait of C2 does not form concentric lines with respect the water reference portrait. These results suggest that the softening effect of both cantilever beams are different as the hydrogen peroxide may structurally degrade each beam in a different mode.

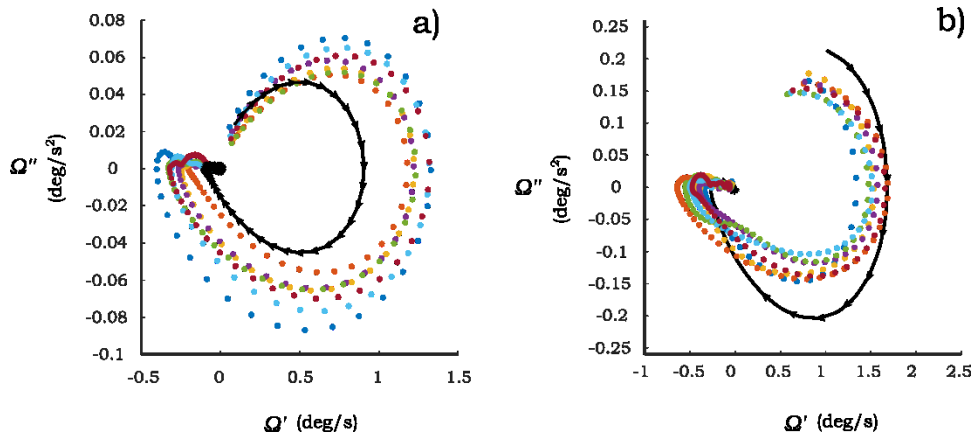


Figure 5.11 Phase portrait of the dynamic response of the cantilever beams a) C1 and b) C2 under the influence of water. The black line represents the phase portrait of water. Color points represent experimental measurements using  $N=7$ . Sample recording is 2s and 1s for C1 and C2, respectively.

### 5.4.3 Glycerol

The phase portraits of water-glycerol solutions are presented in Fig 5.12. Such solution is expected to have specific effects on each beam (C1 and C2) as glycerol is a hygroscopic substance. Glycerol holds water molecules; this effect reduces the evaporation rate. Such feature has been

applied to slow the drying process on adhesives and glues [154]. Glycerol is often applied as a plasticizer in a variety of materials such as gaskets, paints, and inks to add softness. It is expected that the combination of these two properties will lead to a specific phase portrait for each type of cantilever.

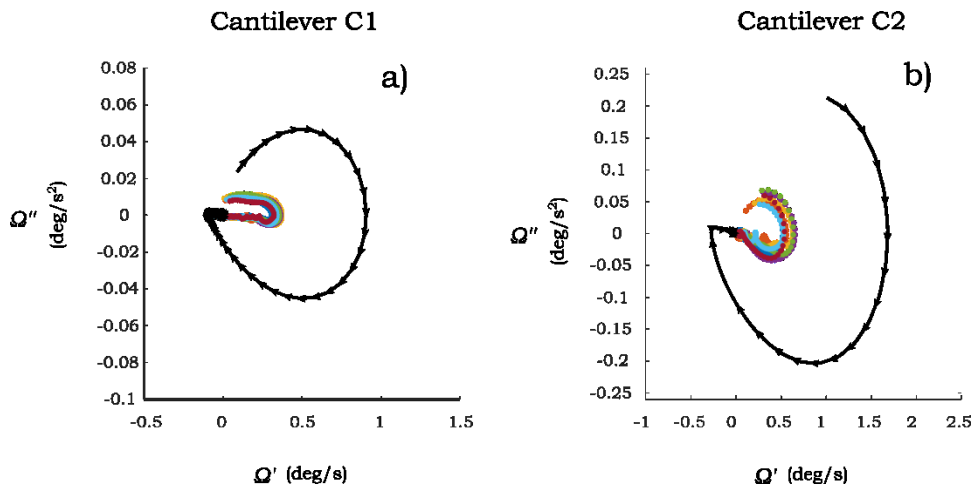


Figure 5.12 Phase portrait of the dynamic response of the cantilever beams a) C1 and b) C2 under the influence of glycerol. The black line represents the phase portrait of water. Color points represent experimental measurements using  $N=7$ . Sample recording is 2s and 1s for C1 and C2, respectively.

It can be seen in Fig. 5.12a that the portrait phase of C1 is significantly smaller in amplitudes compared to the water reference portrait. However, the shape of the phase portrait is different from that corresponding to pure water. Here, the aspect ratio between the velocity and acceleration of the water-glycerol solution is outstretched along the velocity axis. Hence, the

glycerol is affecting C1 in a different way that pure water does on at least one of the three phenomena involved in the hygro-mechanical bending response. In contrast, the aspect ratio of the phase portrait associated with C2 is similar to the one of the water reference portrait. Thus, glycerol does not significantly modify the shape of the phase portrait of C2.

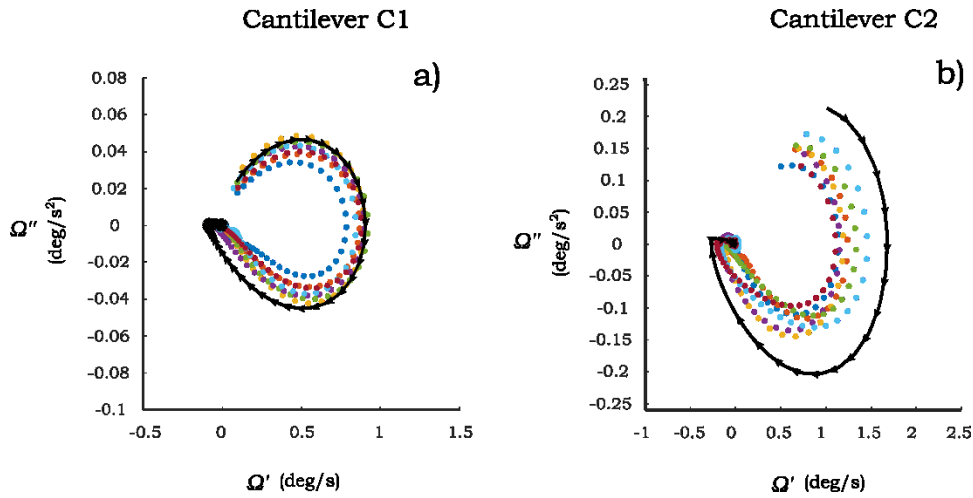


Figure 5.13 Phase portrait of the dynamic response of the cantilever beams a) C1 and b) C2 under the influence of sucrose. The black line represents the phase portrait of water. Color points represent experimental measurements using  $N=7$ . Sample recording is 2s and 1s for C1 and C2, respectively.

#### 5.4.4 Sucrose

Finally, the phase portraits of the water-sucrose solution are presented in Fig. 5.13. Similar to previous substances the response the portraits of both beams C1 and C2 are dissimilar. While the phase portrait of C1 exhibits low sensitivity to the presence of sucrose, the phase portrait of C1

appears to be more sensitive with respect to the water portrait. Both portraits have similar shape compared to the one of pure water, suggesting that the effect of the sucrose on softening and swelling are comparable to those of water. It is interesting to see that up to some extent all the phase portraits are unique, and it is possible to identify the substances presented in the aqueous solution using either C1 or C2. However, more liquid must be tested to verify the uniqueness of their portraits, and eventually develop a database of such portraits.

## 5.5 Summary

The applicability of PB-HMS as a sensing element to characterize liquid is discussed in this chapter. A PB-HMS using a cantilever-droplet configuration was proposed. It is interesting to remark that the excitation of the sensor is generated by the interaction of the substrate and the polar liquid. In other words, no external power is needed to produce the bending response of the sensor. The experimental results using two types of paper-based cantilever beams (C1 and C2) suggest that the proposed PB-HMS are sensitive to different aqueous binary solutions.

The dynamic bending response of the PB-HMS may be applied to characterize and/or identify binary solutions by means of a phase portrait (velocity, acceleration). It was found that same liquid may have different portrait shapes for a different type of beams depending on their interaction with the beam. From the tested fluids, it was found that those containing

hydrogen peroxide and glycerol yield various shapes when using C1 and C2. In contrast, the aqueous solutions that enclose alcohol and sugar exhibit similar portrait shape when comparing to the water reference portrait but different amplitude scale. Thus it is expected that conditioning the paper-based beams with different fillers may enhance the selectivity of the sensing element to be able to detect one specific substance. From the phase portraits, it is suggested that using either C1 or C2 it is possible to identify the substance in the binary solution. It might also be possible to quantify the amount of the substance in the aqueous solution. A discussion on this matter will be presented in the next chapter.

Besides the well-known of advantages of paper-based systems, low cost and highly disposable, one significant advantage of the proposed PB-HMS is the simplicity of the hardware involved in the measurements. First, the bending response of the paper-based beam is recorded using a portable digital microscope. Other digital cameras including webcams or cell phones may be adopted to simplify the hardware. Second, the bending response is obtained by processing the recorded images. Although the image processing was performed in open source software, a specialized software or smartphone application may be developed to integrate both acquisition and image processing stages.

## Chapter 6 Characterization of liquids by means of PB-HMS

*In the previous chapter, it was found that certain liquids in interaction with paper-based beams yield an atypical hygro-mechanical bending response pointed out by their phase portrait. However, such analysis does not provide the means to quantify the performance of the hygro-mechanical response. In this chapter a method to quantify the performance of the PB-HMS in order to characterize liquids is proposed. The bending response of the PB-HMS is approximated using a linear transfer function model that determines an equivalent system. The dynamic response of PB-HMS shows a similar behavior of their counterpart MEMS; however, it exhibits a very low frequency response. The results show the feasibility of this approach to characterize binary aqueous solution using the proposed method. In addition, the analysis of the hygro-mechanical systems enables the identification of liquids. The proposed method promises a good alternative to performing characterization and/or identification of liquids at a very low cost compared to other commercial equipment such as refractometers and near infrared spectrometers.*

## 6.1 Analogy to high order linear systems

It is suggested that representation of the dynamic response of PB-HMS as an equivalent linear system may provide an alternative approach to quantitatively evaluate the effect of different liquids. In this regard, the interaction of the paper-based cantilever beam and the liquid droplet can be defined through the dynamic response of PB-HMS. This approach may be applied to developed sensors that use similar well-known phenomena such as thermo-mechanical, electro-mechanical, and magneto-mechanical interactions.

Looking at the bending response of PB-HMS presented in the previous chapter (Fig. 5.8) it is not hard to determine that such responses are very similar to well-known dynamic systems (i.e. electromechanical systems). However, the response of the PB-HMS (beam-droplet) exhibits a very low frequency. Taking as a reference the period of the single oscillation describing the bending acceleration presented in Fig. 5.8b, the frequency of the system may be estimated as 33.3 mHz. Such a frequency is very low; it is two orders of magnitude lower compared to typical mechanical systems such as bounce in vehicles and in the heart beating in one adult.

In the view to representing the bending response of PB-HMS as equivalent linear systems, let us assume that the response  $\xi$  (bending angle, velocity or acceleration) can be described by means of one ordinary linear differential equation of  $n^{\text{th}}$  order under a step input ( $u_0$ ) as described in Eq. (5.1).

$$A_n \frac{d^n \xi}{dt^n} + \dots + A_2 \frac{d^2 \xi}{dt^2} + A_1 \frac{d\xi}{dt} + A_0 \tag{5.1a}$$

$$= B_n \frac{d^n u_0}{dt^n} + \dots + B_2 \frac{d^2 u_0}{dt^2} + B_1 \frac{du_0}{dt} + B_0$$

$$u_0(t) = \begin{cases} 0 & t < 0 \\ 1 & t \geq 0 \end{cases} \tag{5.1b}$$

The coefficients of Eq. 5.1 can be easily obtained using experimental data and applying optimization algorithms. The approximation of such coefficient was performed by means of the identification toolbox of MatLab®. The parameter setting to carry out the system identification are summarized in table 6.1.

Table 6.1 Parameter setting applied on the hygro-mechanical system identification.

Parameter	Value
Estimation	Transfer function model
Initial condition	Zero
Initialization method	IV
Search method	Gradient search (grad)

Table 6.2 shows different attempts to fit the experimental results of C2 under the influence of water. The accuracy of the approximation in this toolbox is measured by the “*fit*”, which is the normalized root mean square error and is defined as:

$$fit = \left[ 1 - \frac{\sum(Y - Y_p)}{\sum(Y - \bar{Y})} \right] * 100 \quad 5.2$$

where  $Y$  represents the experimental amplitude of the bending acceleration,  $Y_p$  stands for the value of the output of the transfer function, and  $\bar{Y}$  denotes the mean value of the measured signal. In the case of  $\sum(Y - Y_p) = 0$  a perfect match of 100% is found.

Table 6.2 Fits values of the different identified hygro-mechanical systems.

Transfer function	Number of poles	Number of zeros	fit
$H_1(s)$	2	1	38.15
$H_2(s)$	2	2	72.62
$H_3(s)$	3	1	73.73
$H_4(s)$	3	2	83.16
$H_5(s)$	3	3	91.69
$H_6(s)$	4	1	87.84
$H_7(s)$	4	2	46.29
$H_8(s)$	4	3	42.6
$H_9(s)$	4	4	98.83

From table 6.2 it can be seen that the two best fits are obtained when using the  $H_5(s)$  and  $H_9(s)$  systems, which fits are 91.69% and 98.83%, respectively. The comparison of both systems responses with respect to the experimental bending acceleration is presented in Fig. 6.1. Fig. 6.1a reveals that both systems provide good accuracy. The corresponding

absolute errors of both approximations are presented in Fig. 6.2b. Here, it is shown that these errors are well distributed along the time span.

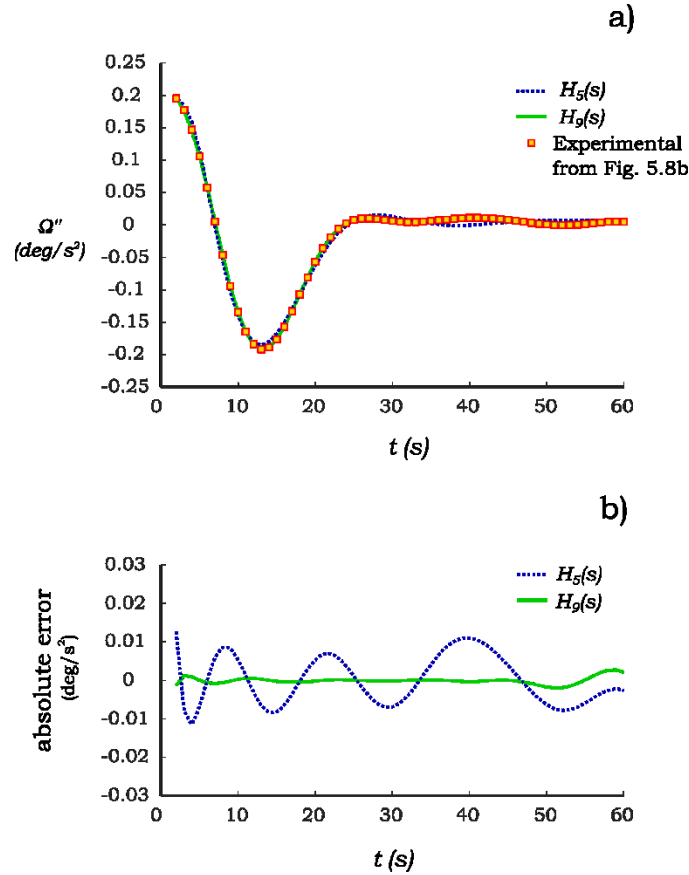


Figure 6.1 Comparison of the estimated transfer function  $H_5(s)$  and  $H_9(s)$  with the experimental acceleration of cantilever C2 under the influence of distilled water. a) Time response signals and b) absolute errors.

Although  $H_9(s)$  provides the best fit it is suggested that  $H_5(s)$  should be used to model the response of the PB-HMS for two reasons. First,  $H_5(s)$  has only three poles, which makes easier the analyses of the hydro-mechanical system. Second, the transfer function  $H_5(s)$  provides a good approximation in the dominant part of the acceleration response ( $t < 30$ s), but exhibits

some discrepancy near to 40s (see Fig. 6.1a). However, this apparent oscillation behavior of the acceleration appears to be irrelevant as it may be due to noise rather than the dynamic response of the PB-HMS. This can be appreciated in Fig. 5.8 where the average of the bending acceleration measurements (N=7) compensates such oscillation behavior. Thus the generic structure of the transfer function of the PB-HMS is defined as:

$$H(s) = \frac{B_3s^3 + B_2s^2 + B_1s + B_0}{s^3 + A_2s^2 + A_1s + A_0} \quad 5.3$$

The PB-HMS described by  $H_5(s)$  can be represented as one pair of complex eigenvalues (poles) and another one real. This transfer function structure is in concordance with the experimental data as one pair of complex poles is needed to describe their oscillatory behavior. Moreover, all the approximations performed in this chapter yield the same transfer function structure. Thus, the conventional frequency analysis of linear systems theory can be performed once the transfer function is estimated.

## 6.2 Frequency analysis

As in the case of the dynamic response of MEMS [61], PB-HMS can also be utilized to analyze liquids. The most common way to investigate the dynamic response of the hygro-mechanical system is to analyze the Bode plot. The Bode plot of the experimental data shown in Fig. 6.1, which includes magnitude and phase, is presented in Fig. 6.2. Here, it can be seen that the hygro-mechanical system exhibit a very low frequency

response (mHz) which is almost six orders of magnitude lower than that of typical microcantilever sensors (kHz) [155]. Perhaps the main parameter to characterize the performance of the hygro-mechanical system is to evaluate the resonance frequency ( $f_r$ ), which represents the excitation frequency that maximized the gain of the system. This maximum gain is known as gain peak ( $G_p$ ) and is often expressed in dB as presented in Fig. 6.2.

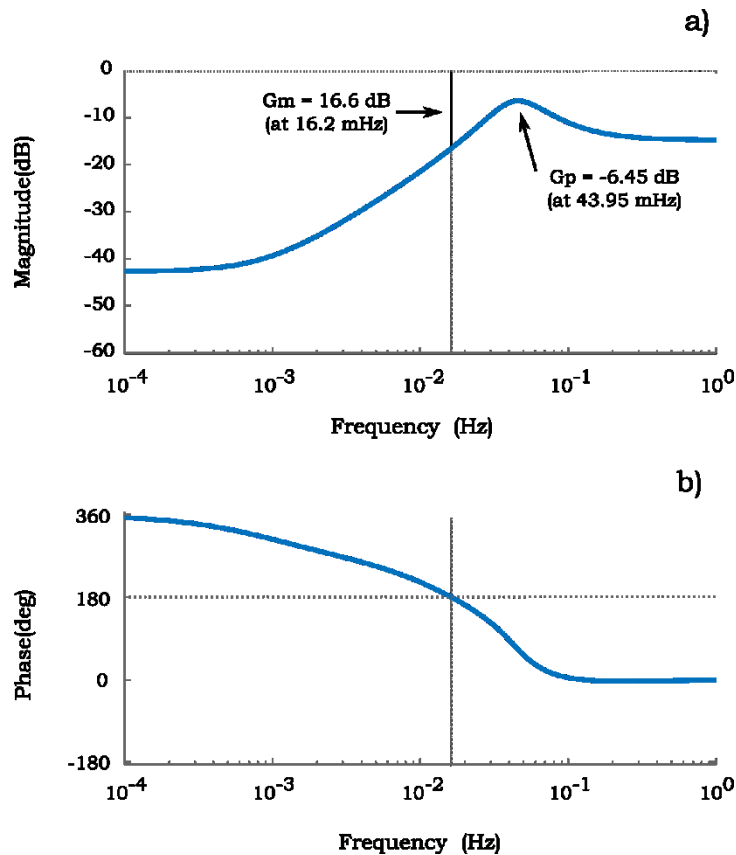


Figure 6.2 Bode plot of the identified hygro-mechanical system corresponding to Fig. 6.1 a) magnitude and b) phase. Both resonance and crossover frequencies are illustrated along with their respective gains peak and margin.

Thus, an alternative approach to characterize the hygro-mechanical system is to evaluate the shift of  $f_r$  as the composition of the binary solution is modified. Such method has been applied to characterize the performance of microcantilever beams sensors [61, 155]. In addition, one may also look at the  $G_p$  of the system in order to obtain further information about the performance of the system. Furthermore, another parameter that describes the performance of the system may also be applied to quantify the response of the system. In the next subsection, a description of the stability analysis is presented in order to investigate the dynamic response of PB-HMS.

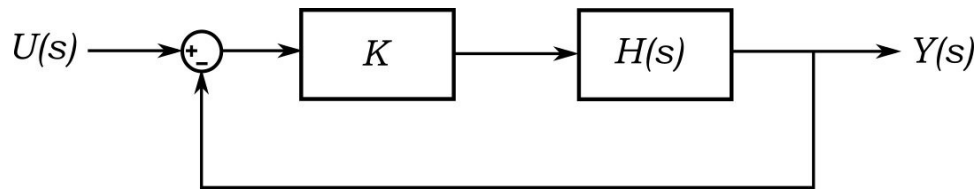


Figure 6.3 Close loop configuration of the hygro-mechanical system under a proportional gain  $K$ .  $U(s)$  and  $Y(s)$  stand for the step input and the virtual bending acceleration, respectively.

### 6.2.1 Stability

From Fig. 6.1 it can be seen that the step input response produces a stable response of the hygro-mechanical system. However, it is possible to perform virtual experiments to the identified hygro-mechanical system to evaluate its performance. In other words, one may evaluate several virtual bending accelerations under different hypothetical scenarios. One of this

possible scenarios is the close loop configuration of the hygro-mechanical system, which is usually applied to control similar systems, see Fig 6.3. Here, the stability of the system may be studied by means of the root locus of the system. Fig. 6.4 shows the root locus plot corresponding to the hygro-mechanical system presented in Fig. 6.1. This plot shows the movement of the poles of the system as the proportional gain  $K$  increases. Here, it can be seen that complex poles tend to move to the positive side of the real part, which is known as the unstable zone. It was found that the hygro-mechanical system identified using Fig. 6.1 remains stable for  $K < 6.72$ ; and, any other higher gain would induce instability.

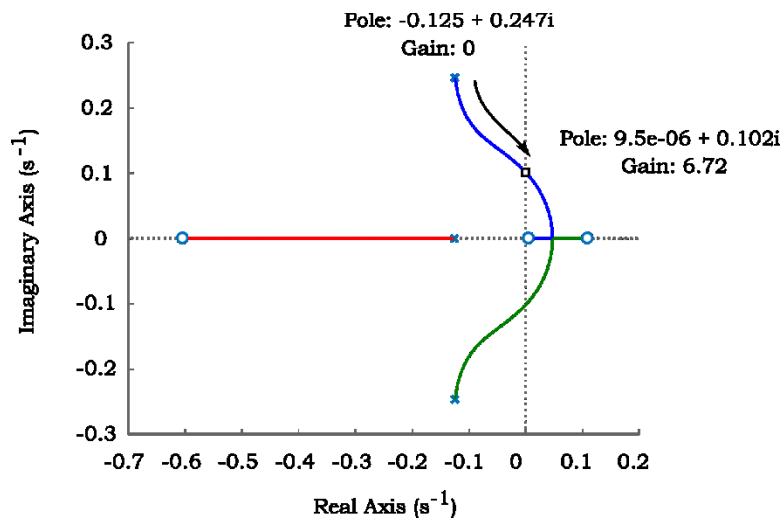


Figure 6.4 Root locus plot of the hygro-mechanical system presented in Fig. 6.1.

In order to illustrate the instability of the close loop hygro-mechanical system, Fig. 6.5 shows the step response in the time domain of such a system under two different gains  $K=6$  and  $K=7$ . It can be seen that the

virtual bending acceleration for  $K=6$  is still stable, but when increasing to  $K=7$  the system becomes unstable.

The stability study can be performed by means of the parameters extracted from the Bode plot known as gain margin ( $G_m$ ). According to Nagurka and Kurfess [156], the gain margin is defined as “*the number of decibels by which the magnitude of the open loop frequency response falls short of unity when the phase angle is 180°*”. The frequency where the phase angle is 180 degrees is often known as crossover frequency. The corresponding gain margin and crossover frequency of the hygro-mechanical system under discussion are illustrated in the Bode plot presented in Fig 6.2. Both parameters may be taken into consideration to quantify the performance of the hygro-mechanical system.

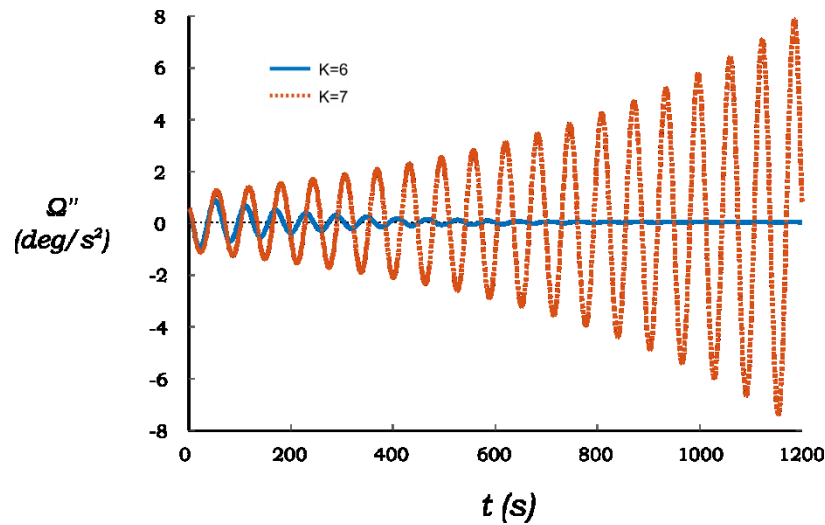


Figure 6.5 Virtual bending acceleration due to a step input of the close loop system exhibiting stable and instable behavior for  $K=6$  and  $K=7$ , respectively.

## 6.3 Characterization of binary aqueous solutions

In order to assess the feasibility of the quantification of the dynamic response of PB-HMS two different binary aqueous solutions are studied in this section. The first is made from methanol at different concentrations 10%, 20%, 30%, and 40% (v/v). The second solution is form from sucrose at the following concentrations: 30 g/L, 60 g/L, 90 g/L, and 120 g/L. Both solutions were made using distilled water and the experiments were carried out according to the description presented in chapter 5. Paper-based cantilever beam C2 was chosen to perform the experiments since it provides a faster time response (~60s) compared to that of the cantilever C1 (~120s). All the hygro-mechanical systems corresponding to these aqueous solutions were estimated using the identification toolbox of MatLab using the setting summarized in Table 6.1.

### 6.3.1 Resonance frequency

The simplest parameter to correlate the concentration of the aqueous solutions is the resonance frequency of the hygro-mechanical system. This parameter has been extensively applied to characterize the performance of MEMS such as cantilever beams, bridges, and membranes. Fig. 6.6 shows the correlation between the concentrations of both aqueous solutions with respect to the resonance frequency ( $f_r$ ). Here, the standard deviation of the resonance frequency is relatively high. As discussed in chapter 5 this source of deviation may be due to the quality of the paper and/or the

filling process of the acrylic resin. It can be seen in Fig. 6.6a that the resonance frequency decreases as the methanol concentration increases. In contrast, the  $f_R$  of the sugar solutions exhibits a very low sensitivity to the increment of sucrose content. Thus, it is suggested that the  $f_R$  of the hygro-mechanical system would be not suitable to estimate the concentration of the binary solution.

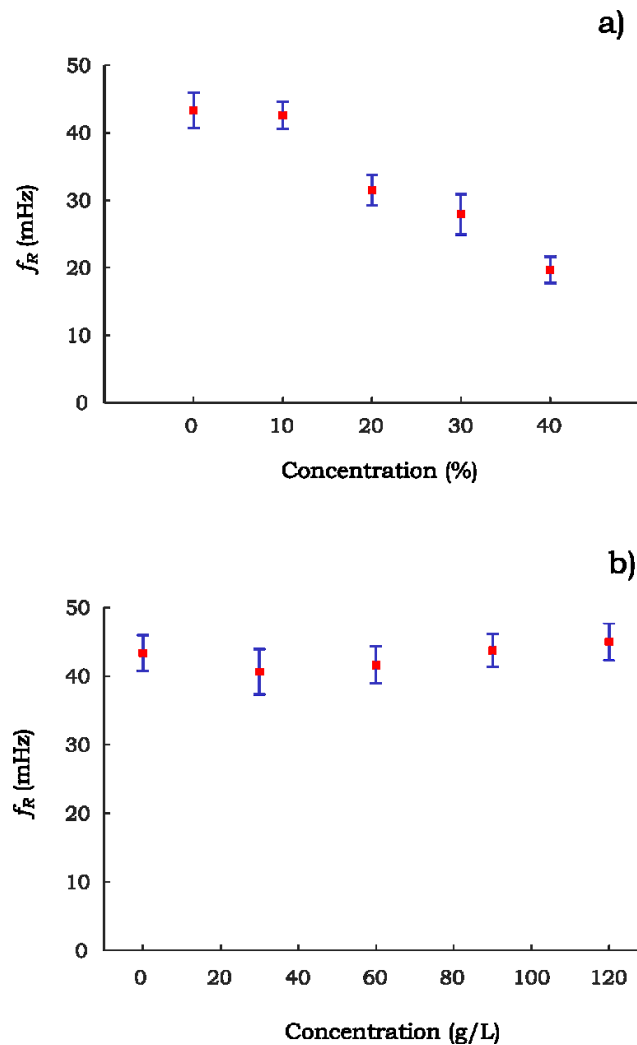


Figure 6.6 Characterization of water-methanol solutions by means of the resonance frequency a) methanol, and b) sucrose solutions (N=7).

### 6.3.2 Gain margin

In addition to the resonance frequency the stability analysis may also be performed. The margin gains of all the identified hygro-mechanical systems were estimated. It was found that the sensitivity of the close loop hygro-mechanical system becomes more robust as the water content in the binary solution decreases. Although the stability study does not represent any physical response of the hygro-mechanical system, this behavior is consistent with the fact that the motion of the system is triggered by water. In other words, less water content would lead to a more stable hygro-mechanical system. Moreover, it was found that the relationship between the gain margin and the concentration of the solutions is almost linear.

Fig. 6.7a presents the gain margin of the hygro-mechanical systems corresponding to the water-methanol solutions. The gain margin increases almost linearly with respect to the methanol concentration. A comparison with the characterization of the methanol solutions by means of the refraction index is presented in Fig. 6.7b. The refraction indexes were measured with a digital refractometer (DR 301-95, Kruess®). This instrument is one of the most common equipment to characterize aqueous solutions by means of its refraction index. The gain margin relationship with the methanol concentration is similar to that corresponding to the refraction index. Hence, it is suggested that this parameter may be applied to characterize the concentration of the water-methanol solutions.

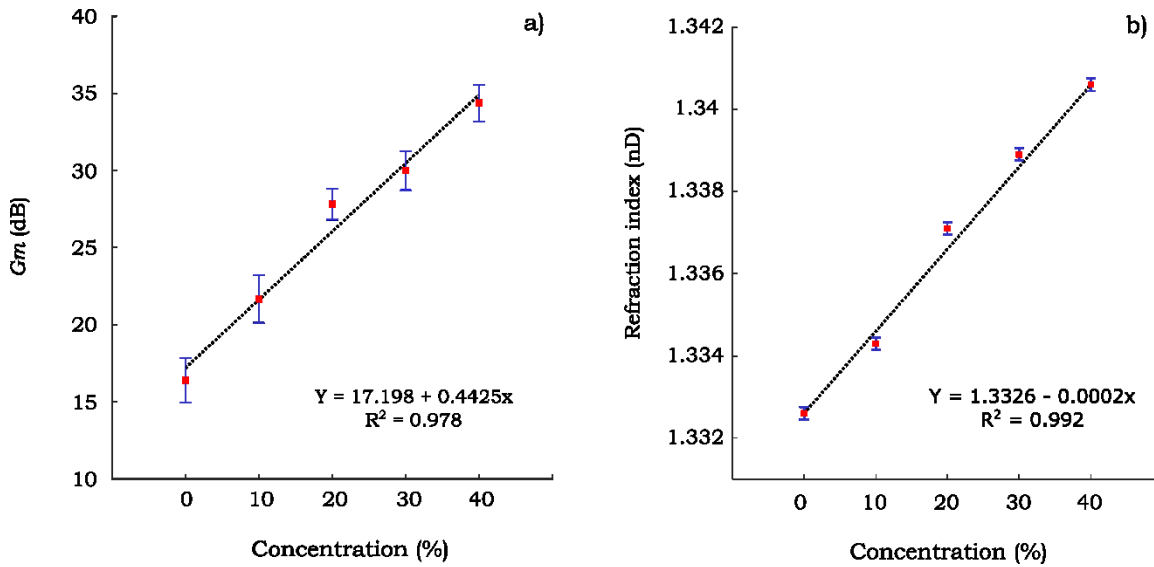


Figure 6.7 Characterization of water-methanol solutions by means of a) hygro-mechanical system using its gain margin (N=7) and b) refraction index via a digital refractometer (N=7).

The gain margin of the hygro-mechanical systems corresponding to water-sucrose solutions and its comparison with the index refraction characterization are presented in Fig. 6.8. The gain margins of the sugar solutions exhibit a similar trend as the case of methanol solutions when increasing their concentration. However, the standard deviation of the gain margin measurements is higher compared to those obtained for methanol solutions. Furthermore, the margin gain appears to be sensitive to both aqueous solutions (methanol and sucrose) compared to the resonance frequency that showed good sensitivity to methanol solutions only.

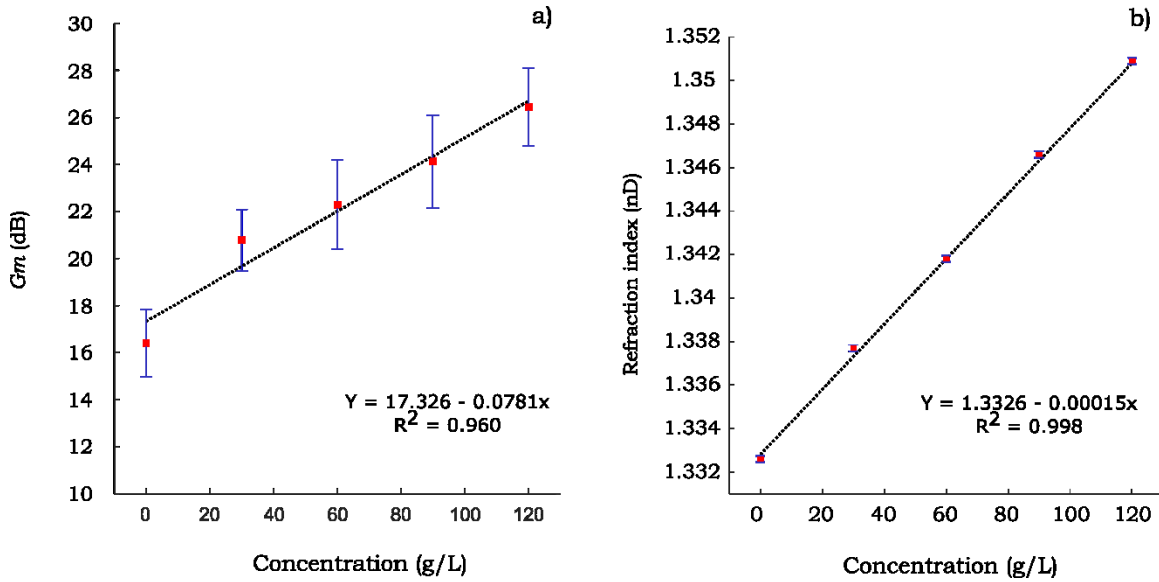


Figure 6.8 Characterization of water-sucrose solutions by means of a) hygro-mechanical system using its gain margin (N=7) and b) refraction index via a conventional refractometer (N=7).

The sensitivity associated with the characterization water-methanol and water-sucrose solutions using both gain margin and index refraction detection is presented in Table 6.3. As can also be seen in Fig 6.7 and 6.8 the hygro-mechanical system is more sensitive to the methanol solutions than to the sucrose solution within the concentration ranges. For these ranges the sensitivity of methanol solutions is almost six times higher than that corresponding to the sucrose solutions. In contrast, for the case of the characterization using the index refraction both solutions exhibit a similar sensitivity for the given range of concentrations. It is expected that the sensitivity of sucrose solution may be increased by modifying the type of paper and/or the filling polymer.

Table 6.3 Sensitivity of tested binary aqueous solutions using both gain margin and index refraction by means of PB-HMS and refractometer, respectively.

Aqueous solution	PB-HMS	Refractometer
Methanol	0.4425 dB/%	0.0002 nD/%
Sucrose	0.0781 dB L/g	0.00015 nD L/g

It can be seen in Fig. 6.7 and 6.8 that the deviation of the gain margin ( $Gm$ ) is extremely high compared to that of the index refraction ( $nD$ ). However, considering that the design of the paper-based cantilever beams can be enhanced it is expected that this drawback may be minimized. Despite the associated drawbacks on the prelaminar results such as high deviation and low sensitivity to sucrose solutions, it is expected that the measurement of the gain margin may be applied to characterize binary aqueous solutions.

Moreover, the characterization of liquids by means of the hygro-mechanical systems has some advantages against conventional refractometers. First, the sample volume to perform the characterization is remarkably small. The required volume to characterize a liquid using the hygro-mechanical detection is  $1.5\mu\text{L}$ , three orders of magnitude smaller to that necessary to measure the index refraction using digital refractometers. Second, the hygro-mechanical characterization eliminates the cross contamination as the sensing elements are disposable. These

features may be of interest in biological applications, where the volume of biohazard analyte is examined using small volumes, usually in the range of  $\mu\text{L}$ .

## 6.4 Liquid identification

Perhaps one of the most significant advantages of the proposed sensing method is that it provides a frequency spectrum rather than one single measurement value such as the refraction index using commercial refractometers. In this case one can describe the performance of the hygro-mechanical system by using more than one variable. It is suggested that this property may be exploited to perform accurate identification of specific liquids, which represents one drawback of the commercial refractometers.

In this section the analysis of the dynamic performance of the hygro-mechanical system with the aim to identify liquids is presented. To illustrate this principle the identification of hydrogen peroxide is discussed. Detection of hydrogen peroxide is of interest in safety areas as it can be used to produce powerful liquid explosives in combination to several combustible substances [157].

### 6.4.1 Identification chart

In chapter 5 it was shown that hydrogen peroxide yields to a different phase portrait compared to other three substances (methanol, glycerol, and sucrose) when using the paper-based cantilever beam C2. This effect

was attributed to the corrosive interaction of hydrogen peroxide with the acrylic resin filler. Although the phase portrait indicates a clear difference of the hydrogen peroxide portrait compared to the other substance, it is not possible to estimate how different the portraits are. In this regard, both gain margin and crossover frequency represent good alternatives to quantify the discrepancy between hydrogen peroxide and the other three substances in water solutions.

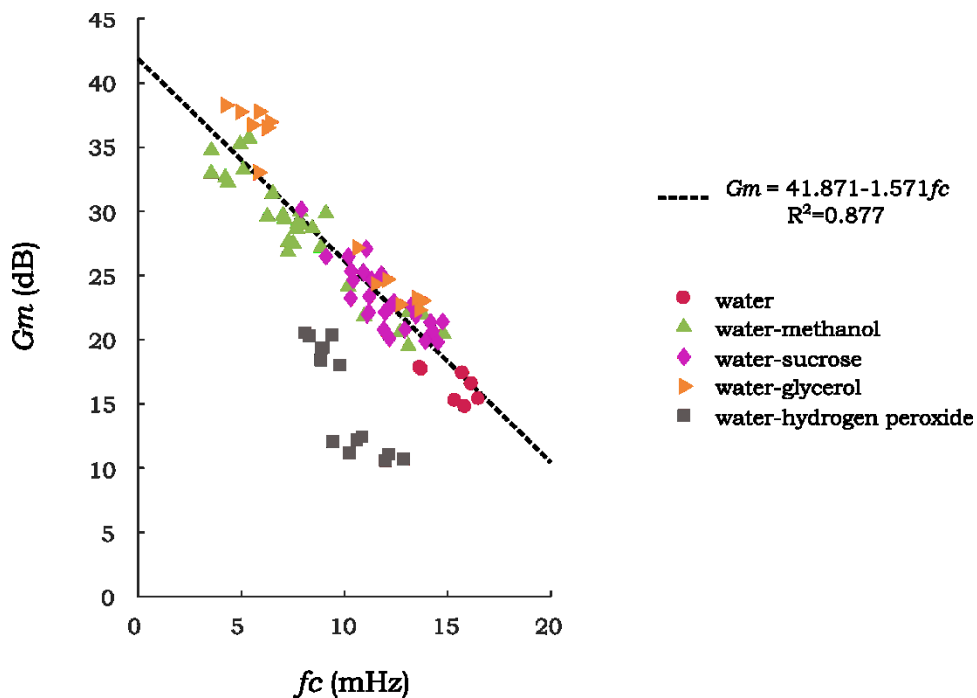


Figure 6.9 Identification chart (crossover frequency against gain margin) of hydrogen peroxide aqueous solutions. Hydrogen peroxide (N=21) exhibit a different trend compared to the methanol, sucrose and glycerol solutions (N=70).

One alternative to identify liquids is to look at the relationship between the crossover frequency and the gain margin. The plot of this relationship

using the data from the previous section (water-methanol and water-sucrose solution) is presented in Fig. 6.9. It can be seen that the all the points related to these aqueous solutions collapse in a single path. Moreover, the corresponding points of water-glycerol solutions (10% and 20% v/v) follow a similar trend. In contrast, the results of the hydrogen peroxide solutions show a different tendency. This behavior is consistent with the phase portrait analysis presented in chapter 5. Thus, it is suggested that such plot can be used as an identification chart.

Based on the identification chart PB-HMS can be classified into two categories according to their dynamic behavior: typical and abnormal. In the first group are those substances that do not severely modify the dynamic response of PB-HMS; in this case, these substances are methanol, sucrose, and glycerol. In the identification chart all of these substances collapse in a linear path ( $R^2 = 0.877$ ), which can be used as a reference line (see Fig. 6.10). In the second group are liquids that significantly alter the dynamic performance of the PB-HMS. The location of these liquids in the identification chart is distant from the reference line. For the tested liquids using paper-based cantilever beams C2 it was found that only hydrogen peroxide belongs to this category.

Furthermore, the proposed identification chart allows the quantification of how different the abnormal hygro-mechanical systems are compared to the typical ones. This task can be carried out by measuring the distance from the reference line to the characteristic point A ( $f_{cA}$ ,  $G_{mA}$ ) of a particular hygro-mechanical system. The schematic representation of this

distance is presented in Fig. 6.10. Considering that the reference line can be represented as:

$$Gm = 41.871 - 1.571fc \quad 6.4$$

the distance  $d$  can be estimated using Eq. 6.5. Here, a negative and positive value of  $d$  represent one point above and below the reference line, respectively.

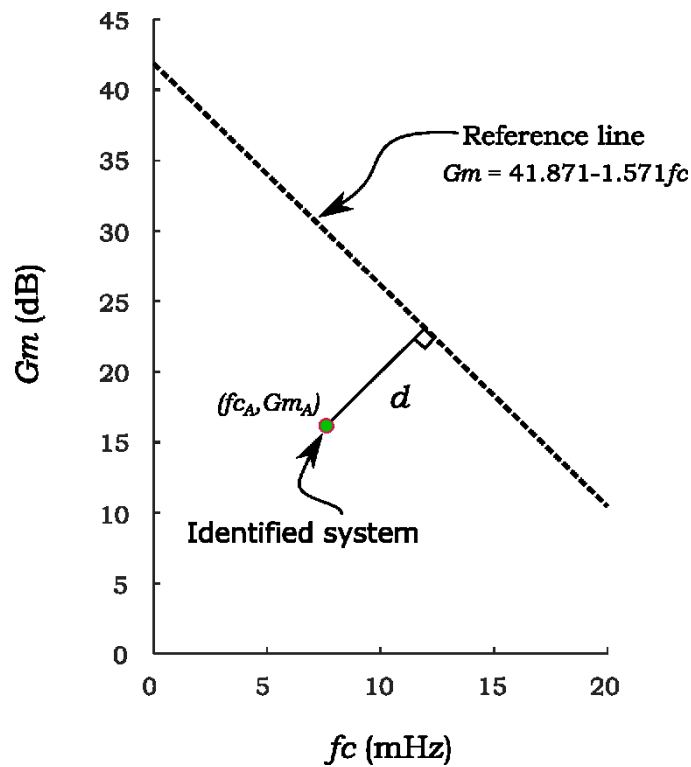


Figure 6.10 Sematic representation of the distance from the reference line to a characteristic point A ( $fc_A$ ,  $Gm_A$ ) of a given hydro-mechanical system.

$$d = \frac{41.871 - Gm_i - 1.571fc}{\sqrt{1 + 1.571^2}}$$

6.5

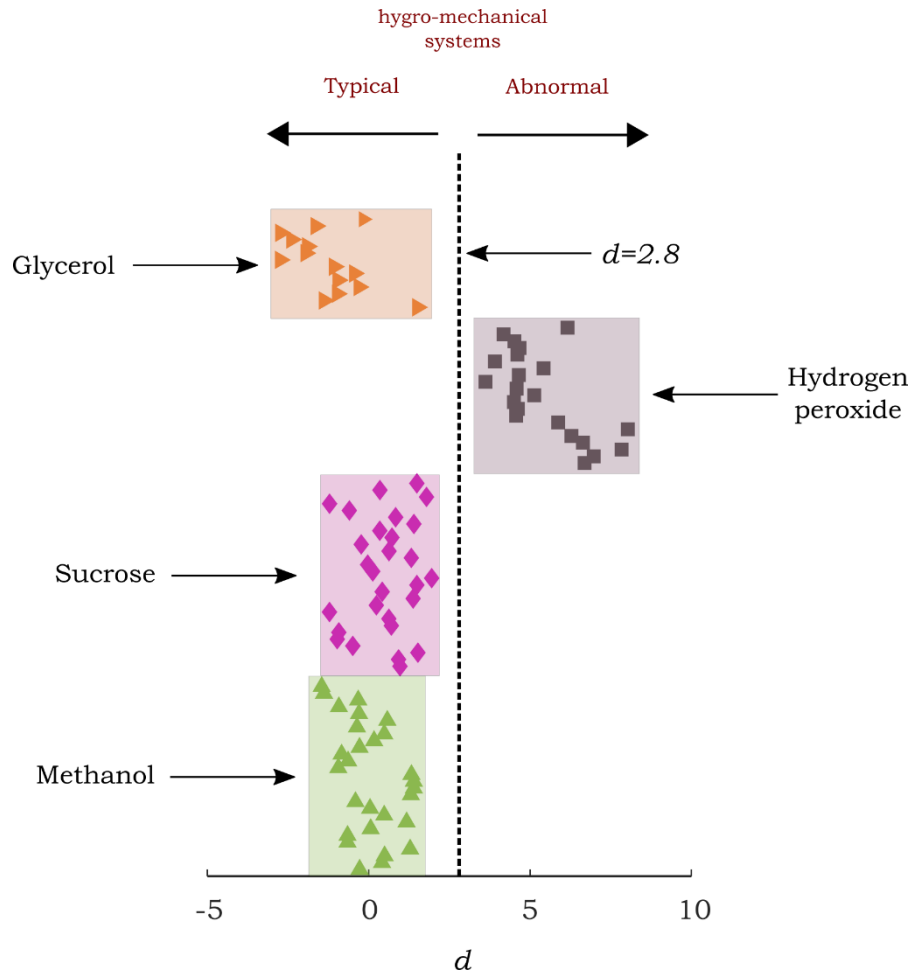


Figure 6.11 Evaluation of the distance  $d$  using Eq. (5.4) to determine a threshold between typical and abnormal hygro-mechanical systems. Typical hygro-mechanical systems  $d < 2.8$ , and abnormal hygro-mechanical systems  $d > 2.8$ .

The estimated values of  $d$  corresponding to the points presented in Fig 6.9 are present in Fig. 5.11. Here, a threshold ( $d=2.8$ ) is determined to classify the hygro-mechanical systems. It can be seen that all the typical

hygro-mechanical systems, those corresponding to methanol, sucrose, and glycerol, have a value of  $d$  less than 2.8. In contrast, the abnormal hygro-mechanical system yields to values of  $d$  higher than 2.8. This proposed approach has one major advantage compared to the phase portrait analysis. As the proposed method yields to a quantitative means to evaluate the dynamic response of PB-HMS it is possible to perform a quick classification using the proper algorithm. Thus, the suggested method represent a good alternative to perform classification of liquids. Although the present analysis was performed using MatLab, the proposed method can be implemented within a microcontroller or microprocessors to enhance the portability of the device.

## 6.5 Hygro-mechanical sensing capabilities

The hygro-mechanical sensing method promises good capabilities to perform characterization and/or identification of liquids. In this section, a brief comparison of the proposed method with respect to commercially available equipment for liquid characterization is presented. Two portable instruments are chosen to perform such a comparison. These two devices are the refractometer DR 301-95 from Kruess® and the near infrared (NIR) spectrometer DWARF-Star from StelleNet®. Both of them are portable equipment. Some of the key features of these instruments in comparison with the proposed hygro-mechanical detection are presented in Table 6.4.

Table 6.4 Comparison of the features of the proposed hygro-mechanical detection with other commercially available techniques.

Instrument	Cost (US dollar)	Characterization of binary solutions	Liquid identification		Tested materials
			Capability	Selectivity	
Refractometer DR 301-95 Kruess®	1000	Yes	No	----	Liquids
NIR spectrometer DWARF-Star StelleNet®	13 000	Yes	Yes	Extremely high	Liquids, gases, and solids
Paper-based Cantilever sensor	Hardware 70 <sup>2</sup> Sensing element:0.00005 <sup>3</sup>	Yes	Yes	low	Polar liquids

<sup>2</sup> Cost estimated considering only equipment cost.

The cost of the proposed sensing method is remarkable low compared to the refractometer and NIR-spectrometer. The cost of the proposed method is below two hundred US dollars compared to the other two instruments that are in the thousand range. Moreover, the hardware cost of the proposed method can be reduced by replacing the digital microscope by a small image sensor. In addition, the cost of the sensing element is very low as the cases of the paper-based microfluidics devices.

Regarding functionality, the proposed method is able to perform the same task as both the refractometer and the NIR-spectrometer with a few limitations. The proposed method is capable of performing characterization of binary solutions same as the refractometer does. However, the improvement of the sensitivity is needed to implement such kind of characterizations. Perhaps the main limitation of the proposed method is that only aqueous liquid can be tested. Nevertheless, the proposed method may be useful in fields that deal with water based solutions (i.e. food industry).

Furthermore, according to the results presented in the previous section it is suggested that the proposed method is capable of performing identification tasks. However, this functionality is still limited compared to the performance of the NIR-spectrometer. First, the type of substance that can be tested for the proposed method is restricted. NIR-spectrometers are capable of performing analyses of substance in different states (liquid, solid and gas), whereas the hygro-mechanical sensing principle is restricted to polar liquids. Second, the selectivity of the proposed method

is limited compared to that of the NIR-spectrometers. The type of liquids that can be detected using NIR-spectrometers is very wide-range. In contrast, the proposed method is only able to classify liquid into two groups. Those liquids that are sensitive to the filler of the paper-based beam can be identified. Thus, the selectivity of the method depend on the sensing element; for example, the paper-based cantilever beams C2 were sensitive only to hydrogen peroxide among the tested liquid. Despite this issue it is expected the proposed method can be applied to identify liquids in practical applications such as body fluids, contaminated water/food and potential dangerous liquids at security check points.

## 6.6 Summary

The analysis of the hygro-mechanical bending response of paper-based beams was preformed using linear systems dynamic theory. It was found that the dynamic response of PB-HMS can be represented as an equivalent linear dynamic system of third order. Crucial information can be extracted by using this approach such as the gain margin, which is related to the stability of the system in close loop. The results show that such a parameter is more sensitive to the water content in the binary solution than the resonance frequency is. It was found experimentally that it is possible to correlate the concentration of a particular binary solution by using the gain margin.

In addition to the conventional advantages of paper-based systems (i.e. low cost, disposability and environmentally friendly) the proposed method offers two other advantages over commercial refractometers: small amount of sample liquid and elimination of cross contamination. However, the experimental results show that the characterization of liquids by using the identified hygro-mechanical system has some drawbacks to overcome, such as low sensitivity to sugar content and high measurement deviation. It is expected that these issues may be solved by improving the design of the paper-based cantilever beam.

Most important, the results suggest that it is possible not only to characterize binary solutions but also to perform identification of liquids. By using an identification chart (gain margin vs. crossover frequency) it is possible to identify those liquids that induce a modification on the dynamic performance of the hygro-mechanical system. This property of the paper-based hygro-mechanical systems was illustrated by performing the identification of hydrogen peroxide. This feature of the hygro-mechanical detection may be of interest in different areas such as safety, biological assays, and food industry.

The proposed method for performing hygro-mechanical characterization and/or identification of liquid is summarized in the following steps:

- i) To fabricate the paper-based sensing element using the proper type of paper and filler.

- ii) To acquire the bending angle of the sensing element due to its interaction with the tested liquid.
- iii) To obtain the bending acceleration by means of the centered differentiation numerical method.
- iv) To perform the identification of the hygro-mechanical system that matches the bending acceleration response.
- v) To execute a post-processing analysis of the identified system by evaluating the margin gain and its associated crossover frequency.
- vi) To estimate the content of the binary solution or to perform the identification test.

However, the previous steps could be modified to improve the performance of the hygro-mechanical detection. Some of the suggested modifications are presented in next chapter.

## Chapter 7 Conclusions and future work

*This chapter presents the conclusion of this research as well as the suggested future work. The general conclusions of this thesis are stated in the first section of this chapter. The second section summarized the particular contributions of the conducted research and presented the suggested future work.*

## 7.1 Conclusions

Numerous efforts have been conducted to develop paper-based microfluidics systems for diverse applications over the past few years. However, it is expected that many other paper-based systems may also be developed by taking advantage of the physical properties of paper. The principal intention of this thesis was to extend the current knowledge regarding paper-based systems (PB-HMS); in particular, by developing PB-HMS for sensing purposes. In this thesis, the development of a novel paper-based system, which capitalizes the hygroscopic properties of paper, was achieved.

The developed (PB-HMS) is formed by the interaction of a liquid droplet and a paper-based cantilever beam. In this configuration, the cantilever beam acts as a sensitive element, while the liquid droplet starts out the bending response of the PB-HMS. The developed PB-HMS exhibit one main advantage over current paper-based mechanical sensors and actuators. Paper plays an active role in the production of motion compared to other works that used paper only as a structural material. Hence, these systems do not require an external source of energy to excite the sensing element (i.e. electric or magnetic field) as the motion is triggered by the liquid droplet to be tested.

The brought up PB-HMS represents a novel alternative to performing characterization and/or identification of water-based liquids at an extremely low cost. The results suggest that the developed PB-HMS are

sensitive to the amount of water in the droplet. Perhaps one of the most interesting potential applications of the developed PB-HMS is the characterization of bio-fluids. However, one of the challenges here is to increase the sensitivity of the PB-HMS to be able to carry out the characterization of these liquids since the water content on them is usually more than 95%. In addition, the reduction of the time response of the paper-based hygro-mechanical is needed in order to perform quick identifications as those performed by spectrometers.

It is expected that this work may contribute to the development of other PB-HMS not only for sensing but also for actuation applications. The possibility of new PB-HMS developments is wide-ranging. This thesis focused on the bending response of PB-HMS. However, another type of motions inspired on those presented in plants (twisting and cooling) can be applied to design new PB-HMS. In addition, another type of system arrangements can be developed instead of the beams-droplet configuration proposed in this thesis. For instance, the interaction of paper-based beams as vapor can also be applied.

## 7.2 Particular contributions and future work

In this thesis, different gaps in the knowledge found in the literature were addressed in order to develop the PB-HMS sensor. In the following subsections, the particular contributions of this thesis, as well as the suggested future work, are presented.

### 7.2.1 Two-dimensional imbibition model

LW theory has been extensively applied to describe the liquid imbibition into paper-based networks. However, this model is restricted to describe the imbibition into one dimension paper-based configurations. Some attempts to describe the imbibition into two-dimensional paper-based networks have been presented by reducing the given geometry to a one dimension problem. However, it was found that in order to potentiate the performance of paper-based systems a better model that predict the imbibition in the whole two-dimensional domain is needed. To accomplish this task a model based on Richards' equation that has been extensively applied in hydrology, was proposed in this thesis to predict liquid imbibition in complex networks. The RMS and maximum relative error of the experimental validation for the wetting area were found to be smaller than 5.4% and 8.9%, respectively, for geometries that do not consider cutouts. In addition, for the case of design including perforation these errors were estimated as 9.3% and 13.5%. However, it is expected that taking into consideration other factors such as anisotropic diffusivity, the accuracy of the model can be improved.

The proposed model is simple and requires only three parameters, which can be easily evaluated experimentally using conventional rectangular paper-based networks. Richard's equation based model presents two main advantages over the LW models. First, this model is able to predict the capillary imbibition into complex geometries networks

including cut-outs and asymmetrical designs. It is expected that this can be exploited to develop new design rules for tuning the flow in paper-based microfluidics devices. Second, Richard's based model is it able to predict the unsaturated water content distribution within the two-dimensional domain. This feature is crucial to predicting the dynamic response of PB-HMS. Perhaps one of the main drawbacks of the proposed model is that the analytical solution of a nonlinear PDE is needed. However, the numerical solution of this types of problems do not require huge computational efforts and can be solved within few minutes. In this work, the solution of such an equation was carried out using MatLab®.

In this thesis, Richard's equation based model was validated using paper-based networks exhibiting near to saturated behavior (chromatography paper). The experimental study of the unsaturated water distribution in treated papers (i.e. printer and tracing paper) is recommended as a future work. The measurement of the water content gradient within the two-dimensional networks represents a technical challenge. Most of the available techniques allow the identification of wet areas but not the quantification of the water content distribution. Thus, it is expected that the development of an experimental technique to assess the water distribution during imbibition would contribute to improving the understanding of this phenomena.

### 7.2.2 Model of hygro-mechanical dynamic response

A better understanding of the hygro-mechanical response of paper under the influence of water was needed as some drawbacks were found in the previous models presented in the open literature. First, the models are not accurate enough to predict the bending response whole time response. Second, these models focus only on the analysis of the curvature, which provides a partial overview of the bending state. Hence, a revisiting formulation of the hygro-mechanical bending response of paper-based structures that overcomes these drawbacks of the previous models was proposed.

The basic concepts of the hygro-mechanical motion induced by hygromorphism as well as the phenomena taking place were reviewed in this thesis. The constitutive equations were applied to develop a one dimension stress-imbibition modeling including three main nonlinearity (imbibition, swelling and softening). The developed model was presented in a dimensionless form, which offers a clear form to identify the influences of such nonlinearities on the typical hygro-mechanical bending response of paper-based beams.

Moreover, a bending state plot was proposed in order to synthesize the bending response. This bending state is the plot of the curvature at the neutral axis against the total strain at the reference layer. Using this plot is possible to know the whole bending state at any time including not only curvature but also the total strain distribution within the paper beam. The

analytical solution of the linear problem was presented with the aim to provide a reference for understanding the hygro-mechanical bending response using the proposed bending state plot. It is suggested that the analysis of the bending response including both curvature and total strain state would be applied to describe different systems including hygro-mechanical bending response as well as other similar soft materials.

### 7.2.3 Nonlinear influences in the bending response

The previous models found in the literature review for hygro-mechanical applied linear water transport models including LW and Fick's law. In addition, these models account only for one nonlinearity source, which is related to the softening effect to of water on paper. However, these models yield a high error when predicting the hygro-mechanical bending curvature of paper. In this thesis, it was proposed that a better understanding of the problem could be achieved by taking into consideration all the three nonlinear influences involved in the hygro-mechanical problem.

In this regard, it was shown that the combination of the nonlinearities related to imbibition, swelling, and softening effect yield a better description of the problem. Indeed, it was found that the nonlinear imbibition plays a fundamental role on the bending response including both curvature and total strain distribution in the entire bending cycle. Moreover, it was found that the softening and swelling nonlinearities only influence a partial zone of the bending cycle. The model including these nonlinearities provides a better estimation of experimental results

presented in previous works compared to the other available models. The RMS error of the proposed model was determined  $0.009 \text{ mm}^{-1}$  compared to  $0.120 \text{ mm}^{-1}$  using model in [59]. Such a difference between the two models is associated to the nonlinear imbibition occurring in the paper-based beam.

Although the nonlinearities related to softening and swelling were included in the proposed model a better understanding of these phenomena at the micro level is needed. The response of these phenomena was estimated using empirical expressions due to the lack of theories regarding these subjects. Hence, an in deep study of these phenomena is suggested as an upcoming research. The development of micro- or meso-models that describe the behavior of paper is needed. In addition, experimental procedures to characterize the softening and swelling response of paper under the influence of different water-based liquid is needed.

#### 7.2.4 PB-HMS as sensors

The hygro-mechanical response of paper has been studied only as a physical phenomenon in the past years. However, in this thesis, it was proposed that it is possible to develop paper-based sensors, which take advantage the hygroscopic properties of paper. In this regard, paper-based cantilever beams were designed and fabricated. The PB-HMS is formed by a sensitive element (cantilever beam) triggered by a small droplet of water-

based liquids. The transient quasi-static bending response of the developed PB-HMS reveals an oscillatory behavior similar to other mechanical systems such as MEMS. It was found that the dynamic bending response of the PB-HMS provides crucial information about the tested liquid compared to single static deflection measurement. In addition to the well-known advantages of paper-based systems (low cost and highly disposable) one advantage of the proposed PB-HMS is the easiness of the read-out method. The bending response of the PB-HMS is recorded using a portable digital microscope and measured using image processing.

Although the proposed method provided a straightforward means to evaluate the bending response of PB-HMS, some modifications are suggested to improve their performance. First, additional sensing element configurations may be studied in order to hence the performance of the PB-HMS. For example, other boundary conditions and/or geometries may be studied. Second, the read out principle may be improved. For instance, the digital microscope may be replaced by a smaller camera or an image sensor to reduce the size of the hardware. Finally, the image processing can be migrated from a personal computer to portable devices such as smartphone or “microprocessors board” to perform real time measurements.

#### 7.2.5 Hygro-mechanical detection

From the dynamic response analysis of the developed PB-HMS, it was found that different aqueous solutions yield a different characteristic

response. However, from the dynamics analysis carried out it was not possible to quantify the performance of the PB-HMS. In this light, a method to quantify the performance of the PB-HMS in order to characterize liquid was implemented in this thesis. This method consists of representing the PB-HMS response as a transfer function model of an equivalent linear system. The transfer function model of the system PB-HMS exhibit a similar response to their counterpart MEMS but having a very low-frequency response. The results showed that it is possible to carry out the characterization of binary aqueous solutions as well as identification of liquids using the proposed method.

Future work regarding the improvement of both sensitivity and selectivity is suggested. First, some issues regarding sensitivity and standard deviation on the experimental characterization of binary aqueous solutions using PB-HMS were observed experimentally. Alternative designs of the sensing element may be considered to overcome these issues. Second, the feasibility to perform characterization of ternary aqueous solutions using has to be assessed. Second, the selectivity for the case of liquid identification has to be studied to identify the suitable combination of paper/filler that has to be applied to perform the identification of a specific liquid. Finally, the feasibility of developed PB-HMS for action purposes may also be explored.

## References

- [1] J. Iannacci, Reliability of MEMS: A perspective on failure mechanisms, improvement solutions and best practices at development level, *Displays*, 37 (2015) 62-71.
- [2] J. Han, X. Liao, A Compact Broadband Microwave Phase Detector Based on MEMS Technology, *Ieee Sensors Journal*, 16 (2016) 3480-3481.
- [3] A. Hati, C.W. Nelson, D.A. Howe, Oscillator PM Noise Reduction From Correlated AM Noise, *Ieee Transactions on Ultrasonics Ferroelectrics and Frequency Control*, 63 (2016) 463-469.
- [4] A. Lucibello, G. Capoccia, E. Proietti, R. Marcelli, B. Margesin, V. Mulloni, F. Giacomozzi, F. Vitulli, M. Scipioni, G. Bartolucci, Reliable response of RF MEMS LTCC packaged switches after mechanical and thermal stress, *Microsystem Technologies-Micro-and Nanosystems-Information Storage and Processing Systems*, 22 (2016) 495-501.
- [5] J. Sun, J. Zhu, L. Jiang, Y. Yu, Z. Li, A broadband DC to 20 GHz 3-bit MEMS digital attenuator(3), *Journal of Micromechanics and Microengineering*, 26 (2016).
- [6] A. Khan, Z. Abas, H.S. Kim, I.-K. Oh, Piezoelectric thin films: an integrated review of transducers and energy harvesting, *Smart Materials and Structures*, 25 (2016).
- [7] A. Rivadeneyra, J. Manuel Soto-Rueda, R. O'Keeffe, J. Banqueri, N. Jackson, A. Mathewson, J.A. Lopez-Villanueva, Tunable MEMS piezoelectric energy harvesting device, *Microsystem Technologies-Micro-and Nanosystems-Information Storage and Processing Systems*, 22 (2016) 823-830.
- [8] Q. Shi, T. Wang, C. Lee, MEMS Based Broadband Piezoelectric Ultrasonic Energy Harvester (PUEH) for Enabling Self-Powered Implantable Biomedical Devices, *Scientific Reports*, 6 (2016).
- [9] R. Takei, N. Makimoto, H. Okada, T. Itoh, T. Kobayashi, Design of piezoelectric MEMS cantilever for low-frequency vibration energy harvester, *Japanese Journal of Applied Physics*, 55 (2016).

[10] K. Tao, J. Wu, L. Tang, X. Xia, S.W. Lye, J. Miao, X. Hu, A novel two-degree-of-freedom MEMS electromagnetic vibration energy harvester, *Journal of Micromechanics and Microengineering*, 26 (2016).

[11] H.V. Demir, C.M. Puttlitz, R. Melik, BioMEMS sensor and apparatuses and methods therefor, *Official Gazette of the United States Patent and Trademark Office Patents*, (2016).

[12] R.R. Jivani, G.J. Lakhtaria, D.D. Patadiya, L.D. Patel, N.P. Jivani, B.P. Jhala, Biomedical microelectromechanical systems (BioMEMS): Revolution in drug delivery and analytical techniques, *Saudi Pharmaceutical Journal*, 24 (2016) 1-20.

[13] J.M. Sanders, L. Butt, A. Clark, J. Williams, M. Padgen, E. Leung, P. Keely, J.S. Condeelis, J. Aguirre-Ghiso, J. Castracane, A BioMEMS Device for the Study of Mechanical Properties of Cells, in: B.L. Gray, H. Becker (Eds.) *Microfluidics, Biomems, and Medical Microsystems Xiii*, 2015.

[14] Global BioMEMS and Microsystem Market in Healthcare 2015-2019 - Reportlinker Review, in, *prnewswire*, 2015.

[15] J. Tamayo, P.M. Kosaka, J.J. Ruz, A. San Paulo, M. Calleja, Biosensors based on nanomechanical systems, *Chemical Society Reviews*, 42 (2013) 1287-1311.

[16] G. Binnig, C.F. Quate, C. Gerber, ATOMIC FORCE MICROSCOPE, *Physical Review Letters*, 56 (1986) 930-933.

[17] S. Xu, Electromechanical biosensors for pathogen detection, *Microchimica Acta*, 178 (2012) 245-260.

[18] M. Calleja, P.M. Kosaka, A. San Paulo, J. Tamayo, Challenges for nanomechanical sensors in biological detection, *Nanoscale*, 4 (2012) 4925-4938.

[19] R.R. Anderson, W. Hu, J.W. Noh, W.C. Dahlquist, S.J. Ness, T.M. Gustafson, D.C. Richards, S. Kim, B.A. Mazzeo, A.T. Woolley, G.P. Nordin, Transient deflection response in microcantilever array integrated with polydimethylsiloxane (PDMS) microfluidics, *Lab on a Chip*, 11 (2011) 2088-2096.

[20] A.S. Nezhad, M. Ghanbari, C.G. Agudelo, M. Packirisamy, R. Bhat, A new Polydimethylsiloxane (PDMS) microcantilever with integrated optical

waveguide for biosensing application, in: J.C. Kieffer (Ed.) Photonics North 2012, 2012.

[21] A.S. Nezhad, M. Ghanbari, C.G. Agudelo, M. Packirisamy, R.B. Bhat, A. Geitmann, PDMS Microcantilever-Based Flow Sensor Integration for Lab-on-a-Chip, *Ieee Sensors Journal*, 13 (2013) 601-609.

[22] G.P. Nordin, R.R. Anderson, W. Hu, S.J. Ness, D.C. Richards, J. Oxborrow, T. Gustafson, B. Tsai, B. Mazzeo, A. Woolley, *Ieee, Microcantilever Array Sensors With Integrated PDMS Microfluidics*, 2011 *Ieee Sensors*, (2011) 1333-1336.

[23] F. Liu, G. Alici, B. Zhang, S. Beirne, W. Li, Fabrication and characterization of a magnetic micro-actuator based on deformable Fe-doped PDMS artificial cilium using 3D printing, *Smart Materials and Structures*, 24 (2015).

[24] E. Makino, T. Mineta, T. Mitsunaga, T. Kawashima, T. Shibata, Sphincter actuator fabricated with PDMS/SMA bimorph cantilevers, *Microelectronic Engineering*, 88 (2011) 2662-2665.

[25] T. Maleki, G. Chitnis, B. Ziaie, A batch-fabricated laser-micromachined PDMS actuator with stamped carbon grease electrodes, *Journal of Micromechanics and Microengineering*, 21 (2011).

[26] N. Bhattacharjee, A. Urrios, S. Kanga, A. Folch, The upcoming 3D-printing revolution in microfluidics, *Lab on a Chip*, 16 (2016) 1720-1742.

[27] I. Mirzaee, M. Song, M. Charmchi, H. Sun, A microfluidics-based on-chip impinger for airborne particle collection, *Lab on a chip*, 16 (2016) 2254-2264.

[28] H.J. Pandya, K. Park, J.P. Desai, Design and fabrication of a flexible MEMS-based electro-mechanical sensor array for breast cancer diagnosis, *Journal of Micromechanics and Microengineering*, 25 (2015) 13.

[29] A. Gaitas, R. Malhotra, K. Pienta, A method to measure cellular adhesion utilizing a polymer micro-cantilever, *Applied Physics Letters*, 103 (2013) 4.

[30] J.Y.H. Kim, M. Nandra, Y.C. Tai, *Ieee, CANTILEVER ACTUATED BY PIEZOELECTRIC PARYLENE-C*, in: 25th IEEE International Conference on Micro Electro Mechanical Systems (MEMS), *Ieee*, Paris, FRANCE, 2012.

- [31] Y.F. Shang, X.Y. Ye, J.Y. Feng, H.Y. Zhou, Y. Wang, Fabrication and Characterization of a Polymer/Metal Bimorph Microcantilever for Ultrasensitive Thermal Sensing, *Ieee Sensors Journal*, 14 (2014) 1304-1312.
- [32] J. Kim, J.Y. Kim, S. Choe, Electro-active papers: Its possibility as actuators, in: Y. BarCohen (Ed.) *Smart Structures and Materials 2000: Electroactive Polymer Actuators and Devices*, 2000, pp. 203-209.
- [33] J. Kim, Y.B. Seo, Electro-active paper actuators, *Smart Materials & Structures*, 11 (2002) 355-360.
- [34] K.B. Lee, Urine-activated paper batteries for biosystems, *Journal of Micromechanics and Microengineering*, 15 (2005) S210-S214.
- [35] A.W. Martinez, S.T. Phillips, M.J. Butte, G.M. Whitesides, Patterned paper as a platform for inexpensive, low-volume, portable bioassays, *Angewandte Chemie-International Edition*, 46 (2007) 1318-1320.
- [36] X.Y. Liu, M. Mwangi, X.J. Li, M. O'Brien, G.M. Whitesides, Paper-based piezoresistive MEMS sensors, *Lab on a Chip*, 11 (2011) 2189-2196.
- [37] X.J. Chen, Y.G. Pan, H.Q. Liu, X.J. Bai, N. Wang, B.L. Zhang, Label-free detection of liver cancer cells by aptamer-based microcantilever biosensor, *Biosensors & Bioelectronics*, 79 (2016) 353-358.
- [38] T.L. Ren, H. Tian, D. Xie, Y. Yang, Flexible Graphite-on-Paper Piezoresistive Sensors, *Sensors*, 12 (2012) 6685-6694.
- [39] X. Li, P. Zwanenburg, X.Y. Liu, Magnetic timing valves for fluid control in paper-based microfluidics, *Lab on a Chip*, 13 (2013) 2609-2614.
- [40] Z.W. Ding, P.H. Wei, G. Chitnis, B. Ziaie, Ferrofluid-Impregnated Paper Actuators, *Journal of Microelectromechanical Systems*, 20 (2011) 59-64.
- [41] A.S. Chen, H.L. Zhu, Y.Y. Li, L.B. Hu, S. Bergbreiter, IEEE, A paper-based electrostatic zipper actuator for printable robots, in: *IEEE International Conference on Robotics and Automation (ICRA)*, Hong Kong, PEOPLES R CHINA, 2014, pp. 5038-5043.
- [42] A. Fraiwan, H. Lee, S. Choi, A paper-based cantilever array sensor: Monitoring volatile organic compounds with naked eye, *Talanta*, 158 (2016) 57-62.

[43] D.M. Cate, J.A. Adkins, J. Mettakoonpitak, C.S. Henry, Recent Developments in Paper-Based Microfluidic Devices, *Analytical Chemistry*, 87 (2015) 19-41.

[44] Y. Xu, M. Liu, N. Kong, J. Liu, Lab-on-paper micro- and nano-analytical devices: Fabrication, modification, detection and emerging applications, *Microchimica Acta*, 183 (2016) 1521-1542.

[45] R. Elbaum, Y. Abraham, Insights into the microstructures of hygroscopic movement in plant seed dispersal, *Plant Science*, 223 (2014) 124-133.

[46] A. Celino, S. Freour, F. Jacquemin, P. Casari, The hygroscopic behavior of plant fibers: a review, *Frontiers in Chemistry*, 2 (2014).

[47] R. Elbaum, S. Gorb, P. Fratzl, Structures in the cell wall that enable hygroscopic movement of wheat awns, *Journal of Structural Biology*, 164 (2008) 101-107.

[48] E. Reyssat, L. Mahadevan, Hygromorphs: from pine cones to biomimetic bilayers, *Journal of the Royal Society Interface*, 6 (2009) 951-957.

[49] Y. Abraham, R. Elbaum, Hygroscopic movements in Geraniaceae: the structural variations that are responsible for coiling or bending, *New Phytologist*, 199 (2013) 584-594.

[50] A. Rafsanjani, V. Brule, T.L. Western, D. Pasini, Hydro-Responsive Curling of the Resurrection Plant *Selaginella lepidophylla*, *Scientific Reports*, 5 (2015).

[51] H. Cheng, J. Liu, Y. Zhao, C. Hu, Z. Zhang, N. Chen, L. Jiang, L. Qu, Graphene Fibers with Predetermined Deformation as Moisture-Triggered Actuators and Robots, *Angewandte Chemie International Edition*, 52 (2013) 10482-10486.

[52] T. Leppänen, J. Sorvari, A. Erkkilä, J. Hämäläinen, Mathematical modelling of moisture induced out-of-plane deformation of a paper sheet, *Modelling and Simulation in Materials Science and Engineering*, 13 (2005) 841.

[53] B. Madsen, P. Hoffmeyer, H. Lilholt, Hemp yarn reinforced composites - III. Moisture content and dimensional changes, *Composites Part a-Applied Science and Manufacturing*, 43 (2012) 2151-2160.

[54] Y. Yao, X. Chen, H. Guo, Z. Wu, X. Li, Humidity sensing behaviors of graphene oxide-silicon bi-layer flexible structure, *Sensors and Actuators B: Chemical*, 161 (2012) 1053-1058.

[55] A. Le Duigou, M. Castro, Moisture-induced self-shaping flax-reinforced polypropylene biocomposite actuator, *Industrial Crops and Products*, 71 (2015) 1-6.

[56] M.-L. Dano, J.-P. Bourque, Deformation behaviour of paper and board subjected to moisture diffusion, *International Journal of Solids and Structures*, 46 (2009) 1305-1316.

[57] G. Gendron, M.L. Dano, A. Cloutier, A numerical study of the hygro-mechanical deformation of two cardboard layups, *Composites Science and Technology*, 64 (2004) 619-627.

[58] S. Douezan, M. Wyart, F. Brochard-Wyart, D. Cuvelier, Curling instability induced by swelling, *Soft Matter*, 7 (2011) 1506-1511.

[59] E. Reyssat, L. Mahadevan, How wet paper curls, *Epl*, 93 (2011).

[60] M. Lee, S. Kim, H.-Y. Kim, L. Mahadevan, Bending and buckling of wet paper, *Physics of Fluids*, 28 (2016) 042101.

[61] B.N. Johnson, R. Mutharasan, Biosensing using dynamic-mode cantilever sensors: A review, *Biosensors & Bioelectronics*, 32 (2012) 1-18.

[62] J. Jensen, M. Farina, G. Zuccheri, W. Grange, M. Hegner, Quantitative, Label-Free Detection of the Aggregation of alpha-Synuclein Using Microcantilever Arrays Operated in a Liquid Environment, *Journal of Sensors*, (2012).

[63] J.E. Sader, Frequency response of cantilever beams immersed in viscous fluids with applications to the atomic force microscope, *Journal of Applied Physics*, 84 (1998) 64-76.

[64] J.W.M. Chon, P. Mulvaney, J.E. Sader, Experimental validation of theoretical models for the frequency response of atomic force microscope cantilever beams immersed in fluids, *Journal of Applied Physics*, 87 (2000) 3978-3988.

[65] C. Vancura, I. Dufour, S.M. Heinrich, F. Josse, A. Hierlemann, Analysis of resonating microcantilevers operating in a viscous liquid environment, *Sensors and Actuators a-Physical*, 141 (2008) 43-51.

[66] H.S. Liao, K.Y. Huang, C.S. Chang, Ieee, Cantilever-based Mass Sensor using High Order Resonances for Liquid Environment, in: IEEE/ASME International Conference on Advanced Intelligent Mechatronics, Budapest, HUNGARY, 2011, pp. 652-655.

[67] R. Cox, J.J. Zhang, F. Josse, S.M. Heinrich, I. Dufour, L.A. Beardslee, O. Brand, IEEE, Damping and Mass Sensitivity of Laterally Vibrating Resonant Microcantilevers in Viscous Liquid Media, 2011 Joint Conference of the Ieee International Frequency Control Symposium/European Frequency and Time Forum Proceedings, (2011) 412-417.

[68] T. Cai, F. Josse, I. Dufour, S. Heinrich, N. Nigro, O. Brand, Ieee, Resonant Characteristics of Rectangular Microcantilevers Vibrating Torsionally in Viscous Liquid Media, 2012 Ieee International Frequency Control Symposium (Fcs), (2012).

[69] X. Xu, A. Raman, Comparative dynamics of magnetically, acoustically, and Brownian motion driven microcantilevers in liquids, Journal of Applied Physics, 102 (2007).

[70] N. Mullin, J. Hobbs, Torsional resonance atomic force microscopy in water, Applied Physics Letters, 92 (2008).

[71] L.A. Beardslee, A.M. Addous, S. Heinrich, F. Josse, I. Dufour, O. Brand, Thermal Excitation and Piezoresistive Detection of Cantilever In-Plane Resonance Modes for Sensing Applications, Journal of Microelectromechanical Systems, 19 (2010) 1015-1017.

[72] T.P. Burg, M. Godin, S.M. Knudsen, W. Shen, G. Carlson, J.S. Foster, K. Babcock, S.R. Manalis, Weighing of biomolecules, single cells and single nanoparticles in fluid, Nature, 446 (2007) 1066-1069.

[73] S. Wang, J. Wang, Y. Zhu, J. Yang, F. Yang, A new device for liver cancer biomarker detection with high accuracy, Sensing and Bio-Sensing Research, 4 (2015) 40-45.

[74] J.J. Wang, Y.F. Zhu, X. Wang, S.P. Wang, J.L. Yang, F.H. Yang, A High-Throughput Cantilever Array Sensor for Multiple Liver Cancer Biomarkers Detection, Ieee Sensors Journal, 16 (2016) 4675-4682.

[75] S. Xu, R. Mutharasan, A novel method for monitoring mass-change response of piezoelectric-excited millimeter-sized cantilever (PEMC) sensors, *Sensors and Actuators B-Chemical*, 143 (2009) 144-151.

[76] K. Rijal, R. Mutharasan, PEMC-based method of measuring DNA hybridization at femtomolar concentration directly in human serum and in the presence of copious noncomplementary strands, *Analytical Chemistry*, 79 (2007) 7392-7400.

[77] K. Rijal, R. Mutharasan, A method for DNA-based detection of *E. coli* O157:H7 in a proteinous background using piezoelectric-excited cantilever sensors, *Analyst*, 138 (2013) 2943-2950.

[78] H. Sharma, R. Mutharasan, Rapid and sensitive immunodetection of *Listeria monocytogenes* in milk using a novel piezoelectric cantilever sensor, *Biosensors & Bioelectronics*, 45 (2013) 158-162.

[79] A. Jeetender, I. Stiharu, M. Packirisamy, G. Balagopal, X. Li, MOEMS based cardiac enzymes detector for acute myocardial infarction, in: *International Conference on Applications of Photonics Technology*, Ottawa, CANADA, 2004, pp. 91-98.

[80] T.I. Yin, Y. Zhao, C.F. Lin, H.H. Tsai, Y.Z. Juang, S.M. Yang, G.A. Urban, The application of capillary force to a cantilever as a sensor for molecular recognition, *Applied Physics Letters*, 98 (2011).

[81] V. Chan, J.H. Jeong, P. Bajaj, M. Collens, T. Saif, H. Kong, R. Bashir, Multi-material bio-fabrication of hydrogel cantilevers and actuators with stereolithography, *Lab on a Chip*, 12 (2012) 88-98.

[82] D. Buenger, F. Topuz, J. Groll, Hydrogels in sensing applications, *Progress in Polymer Science*, 37 (2012) 1678-1719.

[83] A. Agrawal, T. Yun, S.L. Pesek, W.G. Chapman, R. Verduzco, Shape-responsive liquid crystal elastomer bilayers, *Soft matter*, 10 (2014) 1411-1415.

[84] X.M. Mu, N. Sowan, J.A. Tumbic, C.N. Bowman, P.T. Mather, H.J. Qi, Photo-induced bending in a light-activated polymer laminated composite, *Soft Matter*, 11 (2015) 2673-2682.

[85] H.H. Cheng, J. Liu, Y. Zhao, C.G. Hu, Z.P. Zhang, N. Chen, L. Jiang, L.T. Qu, Graphene Fibers with Predetermined Deformation as Moisture-

Triggered Actuators and Robots, *Angewandte Chemie-International Edition*, 52 (2013) 10482-10486.

[86] C. Ganser, G. Fritz-Popovski, R. Morak, P. Sharifi, B. Marmiroli, B. Sartori, H. Amenitsch, T. Griesser, C. Teichert, O. Paris, Cantilever bending based on humidity-actuated mesoporous silica/silicon bilayers, *Beilstein Journal of Nanotechnology*, 7 (2016).

[87] E.W. Washburn, The dynamics of capillary flow, *Physical review*, 17 (1921) 273.

[88] R. Lucas, Ueber das Zeitgesetz des kapillaren Aufstiegs von Flüssigkeiten, *Kolloid-Zeitschrift*, 23 (1918) 15-22.

[89] A.K. Yetisen, M.S. Akram, C.R. Lowe, Paper-based microfluidic point-of-care diagnostic devices, *Lab on a Chip*, 13 (2013) 2210-2251.

[90] X. Li, D.R. Ballerini, W. Shen, A perspective on paper-based microfluidics: Current status and future trends, *Biomicrofluidics*, 6 (2012).

[91] S.F. Cheung, S.K.L. Cheng, D.T. Kamei, Paper-Based Systems for Point-of-Care Biosensing, *Jala*, 20 (2015) 316-333.

[92] J. Adkins, K. Boehle, C. Henry, Electrochemical paper-based microfluidic devices, *Electrophoresis*, 36 (2015) 1811-1824.

[93] L. Ge, J. Yu, S. Ge, M. Yan, Lab-on-paper-based devices using chemiluminescence and electrogenerated chemiluminescence detection, *Anal Bioanal Chem*, 406 (2014) 5613-5630.

[94] Y. He, Y. Wu, J.-Z. Fu, W.-B. Wu, Fabrication of paper-based microfluidic analysis devices: a review, *Rsc Advances*, 5 (2015) 78109-78127.

[95] Y. Jiang, C. Ma, X. Hu, Q. He, Fabrication Techniques of Microfluidic Paper-Based Chips and Their Applications, *Progress in Chemistry*, 26 (2014) 167-177.

[96] E.L. Fu, S. Ramsey, P. Kauffman, B. Lutz, P. Yager, Transport in two-dimensional paper networks, *Microfluidics and Nanofluidics*, 10 (2011) 29-35.

[97] E. Elizalde, R. Urteaga, C.L.A. Berli, Rational design of capillary-driven flows for paper-based microfluidics, *Lab on a Chip*, 15 (2015) 2173-2180.

[98] Z.W. Zhong, R.G. Wu, Z.P. Wang, H.L. Tan, An investigation of paper based microfluidic devices for size based separation and extraction applications, *Journal of Chromatography B*, 1000 (2015) 41-48.

[99] Y. Sun, A. Kharaghani, E. Tsotsas, Micro-model experiments and pore network simulations of liquid imbibition in porous media, *Chemical Engineering Science*, 150 (2016) 41-53.

[100] A. Gunde, T. Babadagli, S.S. Roy, S.K. Mitra, Pore-scale interfacial dynamics and oil-water relative permeabilities of capillary driven counter-current flow in fractured porous media, *Journal of Petroleum Science and Engineering*, 103 (2013) 106-114.

[101] H. Hoang, D. Hoxha, N. Belayachi, D.P. Do, Modelling of two-phase flow in capillary porous medium by a microscopic discrete approach, *European Journal of Environmental and Civil Engineering*, 17 (2013) 444-452.

[102] H. Ovdad, B. Berkowitz, Pore-scale imbibition experiments in dry and prewetted porous media, *Advances in Water Resources*, 30 (2007) 2373-2386.

[103] B. Nestler, A. Aksi, M. Selzer, Combined Lattice Boltzmann and phase-field simulations for incompressible fluid flow in porous media, *Mathematics and Computers in Simulation*, 80 (2010) 1458-1468.

[104] L.A. Richards, Capillary conduction of liquids through porous mediums, *Journal of Applied Physics*, 1 (1931) 318-333.

[105] R. Masoodi, K.M. Pillai, *Wicking in porous materials: traditional and modern modeling approaches*, CRC Press, 2012.

[106] B.V. Zhmud, F. Tiberg, K. Hallstenson, Dynamics of capillary rise, *Journal of Colloid and Interface Science*, 228 (2000) 263-269.

[107] A. Hamraoui, T. Nylander, Analytical approach for the Lucas-Washburn equation, *Journal of colloid and interface science*, 250 (2002) 415-421.

[108] N. Fries, M. Dreyer, An analytic solution of capillary rise restrained by gravity, *Journal of Colloid and Interface Science*, 320 (2008) 259-263.

[109] R. Masoodi, E. Languri, A. Ostadhossein, Dynamics of liquid rise in a vertical capillary tube, *Journal of Colloid and Interface Science*, 389 (2013) 268-272.

- [110] S.F. Nia, K. Jessen, Theoretical Analysis of Capillary Rise in Porous Media, *Transport in Porous Media*, 110 (2015) 141-155.
- [111] B.J. Mullins, R.D. Braddock, Capillary rise in porous, fibrous media during liquid immersion, *International Journal of Heat and Mass Transfer*, 55 (2012) 6222-6230.
- [112] M. Reyssat, L.Y. Sangne, E.A. van Nierop, H.A. Stone, Imbibition in layered systems of packed beads, *Epl*, 86 (2009).
- [113] J.C. Cai, B.M. Yu, A Discussion of the Effect of Tortuosity on the Capillary Imbibition in Porous Media, *Transport in Porous Media*, 89 (2011) 251-263.
- [114] J.C. Cai, E. Perfect, C.L. Cheng, X.Y. Hu, Generalized Modeling of Spontaneous Imbibition Based on Hagen-Poiseuille Flow in Tortuous Capillaries with Variably Shaped Apertures, *Langmuir*, 30 (2014) 5142-5151.
- [115] R. Masoodi, H. Tan, K.M. Pillai, Numerical simulation of liquid absorption in paper-like swelling porous media, *Aiche Journal*, 58 (2012) 2536-2544.
- [116] Y.J. Chen, S. Watanabe, K. Yoshikawa, Roughening Dynamics of Radial Imbibition in a Porous Medium, *Journal of Physical Chemistry C*, 119 (2015) 12508-12513.
- [117] G.D. Liu, M.Y. Zhang, C. Ridgway, P. Gane, Pore wall rugosity: The role of extended wetting contact line length during spontaneous liquid imbibition in porous media, *Colloids and Surfaces a-Physicochemical and Engineering Aspects*, 443 (2014) 286-295.
- [118] B. Markicevic, H. Li, A.R. Zand, H.K. Navaz, Influence of the boundary conditions on capillary flow dynamics and liquid distribution in a porous medium, *Aiche Journal*, 58 (2012) 2911-2919.
- [119] G.Y. Li, X.Q. Chen, Y.Y. Huang, Contact Angle Determined by Spontaneous Imbibition in Porous Media: Experiment and Theory, *Journal of Dispersion Science and Technology*, 36 (2015) 772-777.
- [120] S. Ravi, R. Dharmarajan, S. Moghaddam, Measurement of Capillary Radius and Contact Angle within Porous Media, *Langmuir*, 31 (2015) 12954-12959.

- [121] A. Medina, C. Perez-Rosales, A. Pineda, F.J. Higuera, Imbibition in pieces of paper with different shapes, *Revista Mexicana De Fisica*, 47 (2001) 537-541.
- [122] M. Reyssat, L. Courbin, E. Reyssat, H.A. Stone, Imbibition in geometries with axial variations, *Journal of Fluid Mechanics*, 615 (2008) 335-344.
- [123] S. Mendez, E.M. Fenton, G.R. Gallegos, D.N. Petsev, S.S. Sibbett, H.A. Stone, Y. Zhang, G.P. Lopez, Imbibition in Porous Membranes of Complex Shape: Quasi-stationary Flow in Thin Rectangular Segments, *Langmuir*, 26 (2010) 1380-1385.
- [124] J.F. Xiao, H.A. Stone, D. Attinger, Source-like Solution for Radial Imbibition into a Homogeneous Semi-infinite Porous Medium, *Langmuir*, 28 (2012) 4208-4212.
- [125] A. Askar, Y.C. Jin, Macroporous drainage of unsaturated swelling soil, *Water Resources Research*, 36 (2000) 1189-1197.
- [126] M. Camporese, S. Ferraris, M. Putti, P. Salandin, P. Teatini, Hydrological modeling in swelling/shrinking peat soils, *Water Resources Research*, 42 (2006).
- [127] F. Kalinka, B. Ahrens, A modification of the mixed form of Richards equation and its application in vertically inhomogeneous soils, *Advances in Science and Research*, 6 (2011) 123-127.
- [128] P. Kumar, Layer averaged Richard's equation with lateral flow, *Advances in Water Resources*, 27 (2004) 522-532.
- [129] X. Chen, Y. Dai, An Approximate Analytical Solution of Richards' Equation, *International Journal of Nonlinear Sciences and Numerical Simulation*, 16 (2015) 239-247.
- [130] M. Hayek, An analytical model for steady vertical flux through unsaturated soils with special hydraulic properties, *Journal of Hydrology*, 527 (2015) 1153-1160.
- [131] M. Hayek, An exact explicit solution for one-dimensional, transient, nonlinear Richards' equation for modeling infiltration with special hydraulic functions, *Journal of Hydrology*, 535 (2016) 662-670.

[132] X. Chen, Y. Dai, Differential transform method for solving Richards' equation, *Applied Mathematics and Mechanics-English Edition*, 37 (2016) 169-180.

[133] Z.Y. Zhang, W.K. Wang, T.C.J. Yeh, L. Chen, Z.F. Wang, L. Duan, K.D. An, C.C. Gong, Finite analytic method based on mixed-form Richards' equation for simulating water flow in vadose zone, *Journal of Hydrology*, 537 (2016) 146-156.

[134] I.C.N. Reina, G.A.A. Proano, R.A.C. Flores, C.F.I. Cabrera, Modeling and numerical simulation of the Richards equation for infiltration problems, *Enfoque Ute*, 7 (2016) 46-58.

[135] T.P. Witelski, Intermediate asymptotics for Richards' equation in a finite layer, *Journal of Engineering Mathematics*, 45 (2003) 379-399.

[136] J.C. Crittenden, R.R. Trussell, D.W. Hand, K.J. Howe, G. Tchobanoglous, Appendix C: Physical Properties of Water, in: *MWH's Water Treatment: Principles and Design, Third Edition*, John Wiley & Sons, Inc., 2012, pp. 1861-1862.

[137] D.A. Barry, L. Wissmeier, J.Y. Parlange, G.C. Sander, D.A. Lockington, Comment on "An analytic solution of capillary rise restrained by gravity" by N. Fries and M. Dreyer, *Journal of Colloid and Interface Science*, 338 (2009) 293-295.

[138] C. Hall, Comment on "Source-like Solution for Radial Imbibition into a Homogeneous Semi-infinite Porous Medium", *Langmuir*, 28 (2012) 8587-8587.

[139] C. Hall, Comment on "Imbibition in layered systems of packed beads" by Reyssat M. et al, *Epl*, 98 (2012).

[140] K. Adibkia, J. Shokri, M. Barzegar-Jalali, M. Solduzian, Y. Javadzadeh, Effect of solvent type on retardation properties of diltiazem HCl form liquisolid tablets, *Colloids and Surfaces B-Biointerfaces*, 113 (2014) 10-14.

[141] S.L. Alexander, L.T. Korley, Tunable hygromorphism: structural implications of low molecular weight gels and electrospun nanofibers in bilayer composites, *Soft Matter*, (2016).

- [142] A.B. Figueiredo, S. Magina, D.V. Evtuguin, E.F. Cardoso, J.M. Ferra, P. Cruz, Factors Affecting the Dimensional Stability of Decorative Papers under Moistening, *Bioresources*, 11 (2016) 2020-2029.
- [143] Z. Li, K. Li, C. Camm, Z. Chen, Dimensional Stability of Paper Made from Mixtures of BCTMP and Kraft Fibres, *Journal of Pulp and Paper Science*, 35 (2009) 123-129.
- [144] J. Borch, B.M. Lyne, R.E. Mark, C.C.J. Harbeger, *Handbook of physical testing of paper*, Crc Press, 2001.
- [145] S. Schmid, S. Kühne, C. Hierold, Influence of air humidity on polymeric microresonators, *Journal of micromechanics and microengineering*, 19 (2009) 065018.
- [146] C. Py, P. Reverdy, L. Doppler, J. Bico, B. Roman, C.N. Baroud, Capillary origami: spontaneous wrapping of a droplet with an elastic sheet, *Physical Review Letters*, 98 (2007) 156103.
- [147] S. Bouchemella, A. Seridi, I. Alimi-Ichola, Numerical simulation of water flow in unsaturated soils: comparative study of different forms of Richards's equation, *European Journal of Environmental and Civil Engineering*, 19 (2015) 1-26.
- [148] R.E. Mark, C.C.J. Harbeger, J. Borch, B.M. Lyne, *Handbook of physical testing of paper*, Crc Press, 2001.
- [149] X. Liu, M. Mwangi, X. Li, M. O'Brien, G.M. Whitesides, Paper-based piezoresistive MEMS sensors, *Lab on a Chip*, 11 (2011) 2189-2196.
- [150] P. Du, X. Lin, X. Zhang, A multilayer bending model for conducting polymer actuators, *Sensors and Actuators a-Physical*, 163 (2010) 240-246.
- [151] M.A. Changizi, *Geometry and Material Nonlinearity Effects on Static and Dynamics Performance of MEMS*, in, Concordia University, Montreal Canada, 2011.
- [152] D.P. Holmes, M. Roche, T. Sinha, H.A. Stone, Bending and twisting of soft materials by non-homogenous swelling, *Soft Matter*, 7 (2011) 5188-5193.
- [153] S. Timoshenko, Analysis of bi-metal thermostats, *J. Opt. Soc. Am*, 11 (1925) 233-255.
- [154] B. Katryniok, S. Paul, F. Dumeignil, *The Future of Glycerol: By Mario Pagliaro and Michele Rossi*, in, Wiley Online Library, 2011.

[155] B.N. Johnson, R. Mutharasan, A Cantilever Biosensor-Based Assay for Toxin-Producing Cyanobacteria *Microcystis aeruginosa* using 16S rRNA, *Environmental Science & Technology*, 47 (2013) 12333-12341.

[156] M.L. Nagurka, T.R. Kurfess, Gain and phase margins of SISO systems from modified root locus plots, *IEEE Control Systems*, 12 (1992) 123-127.

[157] J. Liu, *Liquid Explosives*, Springer Berlin Heidelberg, 2015.

## Appendix A

### Richard's equation

This model is developed under the following assumptions. (i) The fluid is incompressible, and the flow is laminar. (ii) The effects of fiber swelling on the imbibition response are neglected. (iii) the imbibition is assumed as isothermal. Under these assumptions, Richards [104] suggested that the motion of the liquid within the porous media can be described using the two dimensional Navier-stokes equations in the cartesian form as:

$$\begin{aligned}\rho \left[ \frac{\partial u}{\partial t} + \frac{\partial u}{\partial x} u + \frac{\partial u}{\partial y} v \right] &= -\frac{\partial p}{\partial x} + \mu \left[ \frac{\partial^2 u}{\partial x^2} + \frac{\partial^2 u}{\partial y^2} \right] + F_x \\ \rho \left[ \frac{\partial v}{\partial t} + \frac{\partial v}{\partial x} u + \frac{\partial v}{\partial y} v \right] &= -\frac{\partial p}{\partial y} + \mu \left[ \frac{\partial^2 v}{\partial x^2} + \frac{\partial^2 v}{\partial y^2} \right] + F_y\end{aligned}\tag{A.1}$$

where  $\mu$  and  $\rho$  are the viscosity and the density of the liquid, respectively. Dividing Eq. (A.1) by  $\rho$  and neglecting inertia terms, as the flow is laminar, Eq (A.1) is reduced to:

$$\begin{aligned}\frac{\partial u_x}{\partial t} &= F_x - \frac{1}{\rho} \frac{\partial p}{\partial x} + \frac{\mu}{\rho} \left[ \frac{\partial^2 u_x}{\partial x^2} + \frac{\partial^2 u_x}{\partial y^2} \right] \\ \frac{\partial u_y}{\partial t} &= F_y - \frac{1}{\rho} \frac{\partial p}{\partial y} + \frac{\mu}{\rho} \left[ \frac{\partial^2 u_y}{\partial x^2} + \frac{\partial^2 u_y}{\partial y^2} \right]\end{aligned}\tag{A.2}$$

Moreover, Eq. (A.2) can be expressed in the abbreviated form as:

$$\frac{du}{dt} = F - \frac{1}{\rho} \nabla p + \frac{\mu}{\rho} \nabla \cdot \nabla u\tag{A.3}$$

In Eq. (A.2) the fluid flow can be described by means of three forces per unit of mass.  $F_x$  and  $F_y$  represent external forces in the direction  $x$  and  $y$ , respectively. In the case of imbibition into paper-based networks gravity is the only external force influencing the motion of the fluid. The force  $F$  can be expressed as the negative gradient of the potential  $\Theta = gy$  as follows

$$F = -\nabla\varphi = -g \quad (\text{A.4})$$

where  $g$  represents the gravity. The term  $\nabla p/\rho$  represents the force due to the pressure gradient and can be expressed as the gradient of the potential  $\psi = \int dp/\rho$ . Hence, Eq. (A.3) can be rewritten as

$$\frac{du}{dt} = -\nabla\Phi + \frac{\mu}{\rho} \nabla \cdot \nabla u \quad (\text{A.5})$$

where  $\Phi$  is the head pressure differential and is defined as

$$\Phi = \Theta + \psi \quad (\text{A.6})$$

The motion of the fluid described by Eq. (A.5) can be represented by Darcy's law for porous media using the average procedure. In this case, the averaged volumetric flow,  $q$ , can be expressed as:

$$q = -\frac{k\rho}{\mu} \nabla\Phi \quad (\text{A.7})$$

where  $k$  represents the permeability of the averaged porous material. Capillary models are usually developed assuming that both the differential of pressure and the permeability are constant [87, 88, 106-108]. In this case, the solution to the one-dimensional problem is reduced to the LW theory. An empirical relationship of the permeability as a function of time was developed in [115] to account for the swelling influences in one-dimensional lateral flow. However, a general framework for describing the two-dimensional flow in paper-based networks has not been presented upto day. According to [104] the permeability in an unsaturated media is highly dependent on the volumetric content of liquid ( $\varphi$ ). The volumetric content is defined as the ratio between the volume of liquid and the total volume of the media. Thus, by defining the fluid conductivity as

$$K(\varphi) = \frac{k(\varphi)\rho}{\mu} \quad (\text{A.8})$$

Eq. (A.7) can be rewritten as

$$q = -K(\varphi)\nabla\phi \quad (\text{A.9})$$

Setting the plane XY as reference in which the gravitational force acts in the vertical (-y) direction, the pressure head differential is defined as

$$\phi = \psi(\varphi) + z \quad (\text{A.10})$$

where  $\psi(\theta)$  represents the capillary pressure head as a function of the volumetric content. Thus, by applying the continuity equation the two-dimensional Richard's equation its mixed form is obtained as

$$\frac{\partial \varphi}{\partial t} = \nabla(K(\varphi)\nabla(\psi(\varphi) + z)) \quad (\text{A.11})$$

By defining an equivalent diffusivity function of the media as

$$D(\varphi) = K(\varphi) \frac{\partial \psi(\varphi)}{\partial \varphi} \quad (\text{A.12})$$

Eq. (3) can be transformed into its volumetric content for

$$\frac{\partial \varphi}{\partial t} = \frac{\partial}{\partial x} \left( D(\varphi) \frac{\partial \varphi}{\partial x} \right) + \frac{\partial}{\partial y} \left( D(\varphi) \frac{\partial \varphi}{\partial y} \right) + \frac{\partial K(\varphi)}{\partial z} \quad (\text{A.13})$$

## Appendix B

### Large deflection solution using COMSOL

All the computed stress and deformation state in COMSOL Multiphysics® are referred to the material coordinates, also known as total Lagrangian configuration. When one object is deformed by either internal or external forces each particle preserves its material coordinates; however, its spatial coordinates change with respect to time and applied forces.

$$\mathbf{x} = \mathbf{X} + \mathbf{u}(\mathbf{X}, t) \quad (\text{B.1})$$

The current spatial position only depends on the displacement vector  $\mathbf{u}$  as the material coordinates are constant. The global Cartesian components in the  $x$  and  $y$  direction of  $\mathbf{u}$  are defined as  $u$  and  $v$ , respectively. These two components are the dependent variables in the Solid Mechanics interface of COMSOL Multiphysics. Hence, the gradient of the displacement is defined with respect to material coordinates as:

$$\nabla \mathbf{u} = \begin{bmatrix} \frac{\partial u}{\partial X} & \frac{\partial u}{\partial Y} \\ \frac{\partial v}{\partial X} & \frac{\partial v}{\partial Y} \end{bmatrix}$$

For the case of small deflections the total strain tensor is written in terms of the displacement gradient using Eq. (B.4). The representation in

Cartesian coordinates using the displacements leads to the expressions applied in chapter 3 for the case of small deflections.

$$\boldsymbol{\varepsilon} = \frac{1}{2}(\nabla\mathbf{u} + \nabla\mathbf{u}^T) \quad (\text{B.3})$$

For the case of large deflection one has to study how the infinitesimal element  $d\mathbf{X}$  is mapped to the corresponding deformed element  $d\mathbf{x}$ . In this light, the deformation gradient  $\mathbf{F}$  is defined as follows:

$$d\mathbf{x} = \mathbf{F}d\mathbf{X} \quad (\text{B.3})$$

From the deformation gradient the right Cauchy-Green tensor can be defined as

$$\mathbf{C} = \mathbf{F}^T\mathbf{F} = (\nabla\mathbf{u})^T + \nabla\mathbf{u} + (\nabla\mathbf{u})^T\nabla\mathbf{u} + \mathbf{I} \quad (\text{B.3})$$

Hence, the Green-Lagrange strain tensor is defined as

$$\boldsymbol{\varepsilon} = \frac{1}{2}(\mathbf{C} - \mathbf{I}) \quad (\text{B.3})$$

For a linear elastic material the stress tensor can be expressed as:

$$\mathbf{s} = \mathbf{D}:(\boldsymbol{\varepsilon} - \boldsymbol{\varepsilon}_h) \quad (\text{B.3})$$

where  $\mathbf{D}$  represents the 4<sup>th</sup> order elasticity tensor and “:” is the double-dot tensor product. The solution of the constitutive equations in the Solid Mechanics in COMSOL Multiphysics is conducted by means of the principle of virtual work. This principle establishes that the sum of virtual work done

by the internal strains is equal to work done by the external loads. COMSOL Multiphysics evaluate the normal and shear strain variables based on the displacement derivatives. Using the tensor strain, stress, and displacement variables, the principle of virtual work for a quasistatic problem is expressed as:

$$\delta W = \int_V (-\varepsilon_{test} : s)$$